博士論文

Generation of Dirac cones in graphene on superlattices

(超格子上グラフェンにおける ディラックコーン生成)

平成２５年１２月博士（理学）申請
東京大学大学院理学系研究科
物理学専攻　田島　昌征

Abstract

In the present thesis, we study generation of Dirac-electron structures in the energy spectrum of hexagonal lattice systems, particularly graphene, under periodic and quasiperiodic superlattice potentials. Graphene is a hexagonal lattice system with carbon atoms and is expected to play an important role in the development of micro-devices in the next decades. Its spectrum in the low-energy range has conical structures, namely the Dirac cones. Other systems of similar energy spectra also attract much attention recently. The Dirac-cone structure has both merits and demerits for applications. The Dirac cones around the Fermi energy cause not only the high electron mobility but also the difficulty of controlling the energy gap. An effort to overcome the difficulty is being done by adding artificial structures to graphene and other Dirac electron systems.

As a part of the effort, applying superlattice potentials to graphene has received widespread attention from theoretical and experimental viewpoints. Park *et al.* have reported for the Dirac Hamiltonian that new massless Dirac cones periodically appear on the linear dispersion under a periodic superlattice potential, particularly depending on the period of the superlattice. Although there are no rigorous proofs that the new spectral structures are truly gapless for tight-binding models, their theories have successfully explained the experimental results.

In the present thesis, we first show that the new structure, which we refer to as the Dirac-electron structure, may have an invisibly small energy for small amplitude of superlattice potential but develops a visible energy gap rapidly and ceases to be a Dirac-electron structure as the potential amplitude increases. In other words, the number of the Dirac-electron structures in the whole spectrum decreases as we apply a stronger potential. We define the energy cutoff ΔE as the minimum energy of the disappeared Dirac-electron structures. The cutoff will be a basic concept to understand double-periodic

cases which we define later. The change of the potential amplitude also shifts the positions of the Dirac-electron structures. This behavior has not been reported for the real Dirac cones in previous works.

When we apply double-periodic potentials, although they are still periodic, the appearance of the Dirac-electron structures strongly changes. Our theoretical study shows that the generation in the double-periodic cases is governed by the Diophantine equation. Assuming that the Dirac-electron structures can appear only below each energy cutoff ΔE for the respective component of the double-periodic potential, we predict that they can appear *sporadically*, which our numerical analysis confirms. By increasing one of the amplitudes of the components, we empirically find that the lower one of the energy cutoffs controls the appearance of the Dirac-electron structures even if the other one does not change.

We next extend the arguments to general Dirac-electron systems under the superlattice potentials and classify them in terms of the energy cutoff ΔE. Our analytical study shows that the generation of the Dirac cones has three different cases. In the first case $\Delta E \geq \pi$, the new cones appear consecutively as in the case of the single-periodic potential. In the second case $\pi/2 \leq \Delta E < \pi$, the generation occurs in two ways, namely sporadic and consecutive, depending on the energy range. In the third case $\Delta E < \pi/2$, the generation of the new Dirac cones are all sporadic. Graphene under a superlattice potential corresponds to the third case.

Finally we study the generation of the Dirac cones induced by a quasiperiodic potential. Quasiperiodic potentials are generally used to study the quasicrystals. A quasiperiodic function is given by the summation of two sine functions with an irrational number as the ratio of the periods. In other words, it is not periodic. We can treat the quasiperiodic function as a limiting case of the double-periodic functions with large periods through a continued-fraction expansion. We thus understand the generation of the Dirac cones in the quasiperiodic superlattice potential as the limiting case of that of the double-periodic one.

The quasiperiodic superlattice case also exhibits three cases of the Dirac cones characterized by the normalized density ρ_{Dirac}. The normalized density ρ_{Dirac} is all unity in the first case $\Delta E \geq \pi$, unity or less than unity depending on the energy range in the second case $\pi/2 \leq \Delta E < \pi$, and all less than unity in the third case $\Delta E < \pi/2$. We study the multifractal spectra of the intervals of the Dirac points. The quasiperiodic systems have been generally believed to have a fractal structure in the energy spectrum. However,

our multifractal spectra show that the intervals are *not* fractal although the system is quasiperiodic.

Contents

Chapter 1

Introduction

1.1 Graphene and Dirac cones

We have used the pencil for a long period of time. One of the reasons why we have used it is that black lead, or graphite, has a layered structure whose binding force is weak enough to be peeled off by hands [1,2]. This fact clearly shows that graphite is very close to our lives.

The common material, graphite, has gathered much attention from the theoretical points of view. In 1947 the pioneering work by Wallace [3] reported the electronic states and an unusual semimetallic behavior of graphite. Other researchers also reported the band structure and the electronic properties in 1950s [4,5]. We now know that graphite consists of two-dimensional layers of carbon atoms [1,2,6,7]. Each layer is a honeycomb lattice in which each carbon atom has three bonds. In other words, carbon atoms share three valence electrons on the honeycomb structure and the last electron can hop on a layer of carbon atoms.

Researchers had believed that isolating a one-atom thick flake from graphite was a very difficult challenge. Furthermore, producing a purely two-dimensional material in a free-standing state had been thought as impossible [8]. Almost 60 years after the pioneering work on graphite [3], a paper in 2004 reported surprising discoveries by using scotch tape [9]. Novoselov and coworkers reported that they obtained just one layer of graphite, namely graphene, and observed electronic properties which are essentially of a two-dimensional semimetal [9]. In addition, two groups reported the measurement of the integer quantum Hall effect in graphene in 2005 [10,11]. After the reports, the

study of graphene gathered great interest from theoretical and experimental points of view [12–14]. Today the studies of graphene grow day by day.

An interesting feature of graphene is its low-energy structure. The tight-binding approximation of the Schrödinger equation tells us that the band dispersion of graphene is linear around the Fermi energy [1,6]. Therefore the low-energy dispersion has a form similar to the massless Dirac equation. This mapping was discussed by Semenoff in 1984 [15]. The valence and conduction bands touch at one point, namely the K and K' points at the Fermi energy. Therefore the energy spectrum of graphene is gapless. The linear dispersion touching at one point is known as the Dirac cone [1, 2, 6].

Recent advances have shown the possibility of creating artificial hexagonal or hexagonal-like systems, for example, nano-pattering of electron gas [16, 17], molecular graphene systems [18], hexagonal optical lattices [19–22], and photonic honeycomb crystals [23, 24]. They are sometimes called *artificial graphene* [17,22,25]. Studying the Dirac cones becomes much more important today.

1.2 Graphene under superlattice potentials

1.2.1 Theories and experiments for superlattices

Graphene is not only studied from fundamental viewpoints, but also is expected to be a basic material for manufacturing micro-structures [26–37]; the energy spectrum and the group velocity can be manipulated with an external superlattice potential. Well known approaches to fabricate graphene superlattices include placing graphene on substrates [27–29, 38–40] and creating graphene nanomesh [41–49].

Graphene nanomesh is recently gathering much attention because of possible applications to electronics [45–49]. It is a nano-structure created by periodically removing atoms from pristine graphene by block copolymer lithography. Field-effect transistors based on graphene nanomesh showed currents nearly 100 times larger than that of graphene nanoribbon of room temperature [45]. A group-theoretical analysis of graphene nanomesh [41] considered superhoneycomb systems consisting of two types of superatoms on the honeycomb lattice and found that the systems can be classified into four types: A_0, A_C, B_0, and B_C. First, they defined the types B and A, according to whether or not neighboring superatoms share atoms in between. Second,

they classified A (B) into A_C (B_C) with atoms at the corner of the superhoneycomb lattice and A_0 (B_0) without the atoms at the corner. They revealed that materials in the three classes A_C, B_0, and B_C should be semimetallic, while the last one A_0 should be a semiconductor. Recent studies indeed reported that the band structure of graphene nanomesh can be controlled by its geometry as well as the symmetry of the sublattices [42–44, 47, 48] .

It is widely believed that constructing a moiré pattern is a hopeful way to achieve graphene superlattice. A moiré pattern is created by setting graphene on a substrate. For example, one recently uses hexagonal boron-nitride [26–31] and iridium surface [38,39] to create *two-dimensional* periodic superlattices. The reason why the method is gathering much attention from many theoretical and experimental studies is that one can easily control the period of the superlattice by tuning the angle between graphene and the substrate.

Furthermore, recent experimental studies reported the creation of *one-dimensional* periodic superlattices by using a high-index surface of copper oxide [40] and mosaic graphene [50, 51] as substrates. The high index surface has terraces separated by monoatomic steps. Thus, graphene on the high-index surface is subjected to a one-dimensional periodic superlattice potential. The mosaic graphene, on the other hand, consists of graphene and atom-doped graphene. In order to make it, one firstly grows discrete graphene grains on a substrate and grafts the grains by nitrogen-doped graphene. Coalescence of the graphene grains thus produces a continuous mosaic graphene monolayer. Bai *et al.* [51] reported that nano-ripples close to the boundary between intrinsic graphene and the nitrogen-doped graphene generates one-dimensional periodic superlattices.

An efficient way to understand the graphene under periodic superlattices was reported by Park *et al.* [52, 53]. Their theoretical studies for the Dirac Hamiltonian showed that graphene under a periodic potential develops new Dirac cones in the energy spectrum around the original Dirac cone (K and K' points) [52,53]. The new Dirac cones are predicted to appear in the dispersion at a constant interval which is determined by the reciprocal vectors of the superlattice. Recent experimental studies indeed reported that the new Dirac cones appear at the predicted energies by using the hexagonal boron-nitride and the copper oxide [26, 27, 31, 40]. The generation of the new Dirac cones is also expected to play a significant role in understanding the electric features of graphene superlattices.

1.2.2 Maintaining Dirac cones

The application of the superlattice potential has stimulated to consider maintaining the Dirac cones against a perturbation in graphene and artificial structures [25]. Neto *et al.* [1] reported that the gapless Dirac cones in graphene under a small uniaxial strain are stable. However, when the deformation exceeds a threshold, the Dirac cones turn into gapful structures [55]. Depending on the direction of an applied tension, the threshold deformation is of the order of 20 %. For a uniaxial strain, the hopping elements of the honeycomb lattice become anisotropic and the two Dirac points move toward each other until they meet at the saddle point [55], where they merge into a point contact and become gapful for larger deformation. Other theoretical studies also reported similar behavior of the Dirac cones [56–58]. Hasegawa *et al.* [56] studied honeycomb lattice systems with nonuniform hopping elements but with keeping the chiral symmetry. They analytically found a gapless condition and showed that the Dirac points again merge at a critical value of the hopping elements. A symmetry argument [54] showed that the if tight-binding Hamiltonian H conserves the chiral symmetry, the Dirac cones remain gapless against a finite perturbation and that the number of the cones is kept to be even under the perturbation.

Asano and Hotta [59] reported the stability of the Dirac cones from a different point of view. They studied the stability of "essential" and "accidental" band contacts against parameter changes (e.g. transfer integrals, on-site energies, and the spatial coordinates). When a band contact occurs at a symmetric point in the $\vec{k}$ space, they called it an essential contact. We can know where the essential contacts take place in advance of solving the secular equation, while accidental contacts can sometimes happen at general points in the $\vec{k}$ space. The studies [54–58] considered the essential contacts, while Asano and Hotta [59] paid attention to the accidental contacts and reported that the band contacts, including the Dirac cones at general points, can merge and be annihilated by tuning the lattice parameters.

1.2.3 Remaining problems

The theoretical and experimental studies have reported that the superlattice potential induce the Dirac cones [26, 27, 31, 52, 53]. However, it is not clearly reported that whether the Dirac-electron structures in the honeycomb lattice systems are truly gapless ones. Strictly speaking, the analytical results in

the previous study [53] are only obtained for the pure Dirac Hamiltonian, which is an effective Hamiltonian, under a superlattice potential. There is a possibility that these Dirac electrons have a small energy gap outside the Dirac Hamiltonian approximation. Indeed, Ponomarenko *et al.* [27] reported that the Dirac electrons in graphene on the hexagonal boron-nitride possibly have small energy gaps.

Previous studies [52,53] have not reported that the shapes and the amplitudes of the superlattice potential affect the new Dirac-electron structures. Lin *et al.* [40] recently pointed out that one needs to study effects of the shape and amplitude of the periodic superlattice potentials in order to understand much detail of the new Dirac cones.

The theoretical studies [52,53] based on the pure Dirac Hamiltonian under periodic superlattice potentials did not set any restrictions to the maximum energy of the new Dirac cones. There must be a limit to the theory, however, because the energy spectrum of graphene under superlattice potential is not well approximated linearly in a wider energy range. In other words, applying the Dirac Hamiltonian to graphene under superlattice potentials may have a limiting energy. Indeed, we later introduce an energy cutoff to take account of the maximum energy of the Dirac-electron structures caused by the superlattice potentials. Although the above experimental studies reported only the new cones very close to the Fermi energy, we expect that further progress in experimental techniques enables us to detect new Dirac cones in higher ranges of the energy spectrum and reveal the energy cutoff.

Previous studies [55, 56] for chiral symmetric systems reported the shift and the annihilation of the Dirac points through merging of the two points. Graphene under a superlattice potential in the form of the identity matrix I in the space of the sublattices clearly breaks the chiral symmetry but it conserves the equivalence of the sublattices. Watanabe *et al.* [60] analytically reported that the honeycomb lattice system with the second-nearest-neighbor hopping of the form of I has Dirac cones. For stronger hopping elements, they revealed that the two gapless Dirac cones always appear at the K and K' points and never merge with each other. The nature of the Dirac electrons with a broken chiral symmetry but with the sublattice symmetry has not been fully understood so far.

1.3 Quasiperiodic superlattice

The behavior of graphene under a *non*-periodic potential also gathers much attention recently. Indeed, an experimental work reported *quasi*periodic ripples in graphene grown by chemical vapor deposition [61]. Theoretical studies of monolayer and bilayer graphenes under a quasiperiodic superlattice suggested that the energy band, the transmission coefficient, and the conductance had self-similar, or fractal structures [37,62,63]. The external potentials were often arranged as the Fibonacci lattice which is a typical quasiperiodic function [64–66]. The results coincided with previous studies for quantum systems with quasiperiodic arrangements.

However, the previous studies of the quasiperiodic systems were based on quantum systems with quadratic dispersions [64–69]. We here consider the possibility that the linear dispersion of graphene makes essential differences in the appearance of the quasiperiodicity and fractal structures in quantum mechanics. In addition the Fibonacci arrangement is intrinsically fractal because its recipe for growing lattice blocks is obviously a self-similar rule [64–66]. In order to avoid any fractal elements, we here study graphene under quasiperiodic superlattice potentials without fractal arrangements.

Before going to the details of our study, we briefly review studies of quasiperiodic systems in quantum mechanics. The one which triggered much attention to the quasiperiodicity is the discovery of a quasicrystal in 1984 [70]. Shechtman and his colleagues reported a non-periodic structure in a crystal which researchers have not considered to exist as a stable state of matter. After the discovery, the non-periodic crystalline structure is called *quasicrystal* as a word for the quasiperiodic crystal [71]. At the same time theoretical studies started to expose the nature of quasiperiodic structures in quantum mechanics, many of which claimed that quasiperiodic systems had fractal structures in both the energy spectrum and the eigenstates [65–69, 72]. The energy spectra of quasiperiodic systems were reported to have fractal structures similar to the Cantor set [67, 72]. Multifractal analyses reported that the eigenstates possessed non-integer dimensions [65–67,69]. It is now widely believed that quantum systems with quasiperiodic arrangements exhibit fractal structures in the energy spectra. Some theoretical studies reinforced the belief by considering the inverse problems [73–75].

1.4 Purpose and organization of this thesis

In this thesis, we study the generation of the Dirac-electron structures induced by superlattice potentials. We first summarize our results.

1. The Dirac-electron structures either are gapless or have very small gaps for small amplitudes of superlattice potentials, but develop visible gaps for amplitudes greater than critical or crossover values. We cannot completely judge from our numerical results whether the energy gaps of the Dirac-electron structures in the tight-binding model under a superlattice potential are truly zero or not. According to the theoretical study [56], it is quite likely that there are invisibly small gaps in the structures.

2. The generation of the Dirac-electron structures is affected not only by the period but also by the amplitude for the potential. As we increase the amplitude, the maximum number of the Dirac-electron structures decreases. We define the energy cutoff in order to characterize the decrease of the number of the Dirac-electron structures. The annihilation of the structures without merging indicate a high likelihood that they have small energy gaps.

3. The shape of the superlattice potential also affects the generation of the Dirac-electron structures. When we add a double-periodic potential, which we will define in a later chapter, we find a different way of generation of the Dirac-electron structures, namely *sporadic*. The sporadic appearance is described by the Diophantine equation. In the case of a greater amplitude, our numerical results show that the lower energy cutoff controls the maximum energy of the sporadic generation.

4. When we regard the cutoff as a model parameter, we can classify the generation of the Dirac-electron structures for the double-periodic potentials into three cases. They can be sporadic, sporadic and consecutive, or consecutive.

5. The three cases also appear in the generation induced by quasiperiodic potentials, which are limiting cases of the double-periodic potentials. Our numerical analysis indicates that the generation of the Dirac-electron structures is hardly fractal although the potential is quasiperiodic.

We organize the thesis as follows. In Chapter 2, we review the theories of graphene, quasiperiodic functions, and the tight-binding model of the hexagonal lattice with a periodic superlattice potential [1, 6, 53]. We briefly show the generation of Dirac cones on the K and K' points at the Fermi energy as the first step. We next show the definition of quasiperiodic functions which we use in this study. A quasiperiodic function is characterized by an irrational number. Therefore we can approximate a quasiperiodic function by a double-periodic function with a rational number as the ratio of the periods. The approximation is based on a relation between an irrational number and a rational number which we explain in Appendix A. We also review the tight-binding model of graphene under periodic superlattice potentials. We only introduce the nearest-neighbor hopping in this thesis and set the on-site potential of pristine graphene to zero. We apply a superlattice potential which is periodic along the lattice vector $\vec{a}_1$ in our study. The tight-binding Hamiltonian with the wave-number representation is the basis for the numerical analysis.

In Chapter 3, we first review the generation of the new Dirac cones under a *single-periodic* potential by using the Dirac Hamiltonian [52,53]. The Dirac cones are indexed by a consecutive series of integers: $n = 0, \pm 1, \pm 2, \ldots$.

We next confirm the generation of the new Dirac-electron structures by numerical analyses of graphene under single-periodic potentials. Our numerical analyses show that up to an energy cutoff, the Dirac-electron structures are possibly gapless or have small energy gaps which are practically invisible in our numerical environment. The index of the Dirac-electron structures continues up to a number, beyond which there appear visible energy gaps. As we increase the potential amplitude, the Dirac-electron structures disappear one by one, developing visible energy gaps suddenly. In other words, the maximum number decreases as the amplitude of the potential increases. We here define the energy cutoff $\Delta E(v)$ as the minimum energy of the disappeared Dirac-electron structures. The new Dirac-electron structures are not isotropic as the ones in graphene. The anisotropy becomes stronger as the index becomes larger. The positions of the Dirac-electron structures move perpendicularly to the reciprocal vector of the superlattice potential through the K and K' points (see Appendix B). Therefore, the two Dirac-electron structures cannot meet each other. According to the theoretical study [56], this suggests that the Dirac-electron structures are not true Dirac cones. We also show the numerical results for different periods in order to use as the starting point for understanding double-periodic cases.

In Chapter 4, we use the energy cutoff as a model parameter for the Dirac Hamiltonian under a double-periodic superlattice potential. In our model, only the new Dirac cones below the energy cutoff appear [76, 77]. We show that the generation rule of the new Dirac cones for *double-periodic* potentials turns out to be the Diophantine equation. When the generation of the new cones is limited by the energy cutoff, the rule indicates that the new cones appear sporadically, which differs from the prediction of the previous study for periodic potentials [52, 53].

The numerical results for double-periodic potentials with small amplitudes show that the generation is indeed sporadic in good agreement with the theoretical prediction from the generation rule. The new Dirac-electron structures are also anisotropic but behave quite differently from those in the single-periodic cases. For potentials of larger amplitudes, on the other hand, the numerical analysis indicates that the lower one of the two energy cutoffs obtained in the corresponding two single-periodic cases, governs the appearance in addition to the generation rule. Thus the number of the Dirac-electron structures becomes less than that of the prediction from the generation rule itself.

We next extend our arguments to general Dirac electron systems. We analytically show that the generation of the Dirac cones has three cases depending on the energy cutoff. In the first case, $\Delta E \geq \pi$, the new Dirac cones appear consecutively while we consider the double-periodic cases. In the second case, $\pi/2 \leq \Delta E < \pi$, the Dirac cones appear either sporadically or consecutively, depending on the energy region. Finally, in the third case, $\Delta E < \pi/2$, the generation is always sporadic.

In Chapter 5, we consider the generation of the new Dirac cones in general Dirac electron systems under a quasiperiodic superlattice potential. Based on the results for the double-periodic potentials, we predict that the new cones appear densely in the energy spectrum under quasiperiodic potentials. The density of the new cones depend on the energy, again because of the energy cutoff of the linear dispersion. In addition, we show multifractal spectra of the intervals of the new Dirac points in the Dirac Hamiltonian under the quasiperiodic potential. Our study suggests a *non*-fractal appearance of the new cones in the energy spectrum although the previous studies of quasiperiodic systems have reported fractal spectrum [64–67]. We apply the multifractal analysis whose formalism is introduced in Appendix D.

Chapter 2

Backgrounds

2.1 Theory of graphene

We first review a theoretical representation of graphene in the tight-binding approximation.

2.1.1 Tight-binding representation of graphene

Graphene is a monoatomic layer of carbon atoms on a hexagonal lattice (Fig. 2.1) [1,6]. The unit cells can be represented by the lattice vectors $\vec{a}_1$ and $\vec{a}_2$:

$$\vec{a}_1 = \frac{a}{2}\begin{pmatrix} 1 \\ \sqrt{3} \end{pmatrix} \tag{2.1}$$

and

$$\vec{a}_2 = \frac{a}{2}\begin{pmatrix} -1 \\ \sqrt{3} \end{pmatrix}, \tag{2.2}$$

where $a \simeq 0.246$ [nm] is the lattice constant. The positions of the unit cells can be represented by $\vec{R} = n_1\vec{a}_1 + n_2\vec{a}_2$, where n_1 and n_2 are integers. A unit cell of graphene includes two equivalent carbon atoms. We denote them as A and B sublattices, which are represented by the filled and open circles, respectively, in Fig. 2.1.

A useful way to represent the energy spectrum is using the wave vector $\vec{k}$ because the lattice structure of graphene has periodicity. The reciprocal vectors are written as

$$\vec{b}_1 = \frac{2\pi}{a\sqrt{3}}\begin{pmatrix} \sqrt{3} \\ 1 \end{pmatrix} \tag{2.3}$$

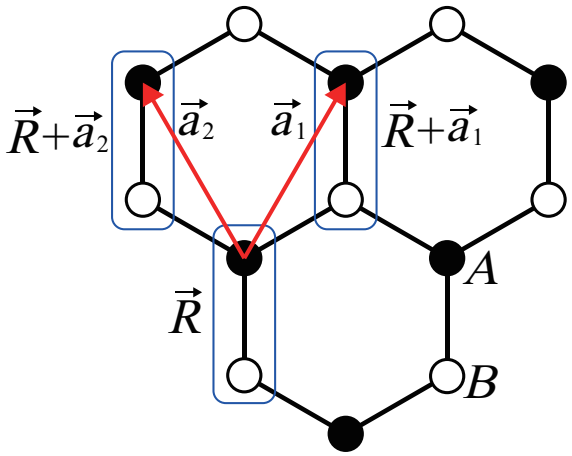

Figure 2.1: Honeycomb lattice of graphene. The filled and open circles represent the A and B sublattices, respectively. The red arrows represent the unit vectors $\vec{a}_1$ and $\vec{a}_2$. Unit cells are emphasized by blue lines.

and

$$\vec{b}_2 = \frac{2\pi}{a\sqrt{3}} \begin{pmatrix} -\sqrt{3} \\ 1 \end{pmatrix}. \tag{2.4}$$

They observe the relation $\vec{a}_i \cdot \vec{b}_j = 2\pi\delta_{i,j}$ $(i, j = 1, 2)$. The first Brillouin zone spanned by the vectors $\vec{b}_1$ and $\vec{b}_2$ is often chosen to be a hexagon (see Fig. 2.2).

We assume that electrons transfer only to the nearest-neighbor sites. We thus use the tight-binding model to represent the electron states of graphene with the periodic boundary conditions. The tight-binding Hamiltonian H_1 can be represented by bra and ket vectors as

$$H_1 = t_1 \sum_{\vec{R}} \left(|\vec{R}; B\rangle\langle\vec{R}; A| + |\vec{R} + \vec{a}_1; B\rangle\langle\vec{R}; A| + |\vec{R} + \vec{a}_2; B\rangle\langle\vec{R}; A| + (\text{h.c.}) \right), \tag{2.5}$$

where t_1 is the hopping element, $|\vec{R}; l\rangle$ $(l = A, B)$ represents the electron wave function on a sublattice l of a unit cell $\vec{R}$, and (h.c.) represents the Hermitian conjugate. Let the whole system have N_1 and N_2 unit cells along the directions $\vec{a}_1$ and $\vec{a}_2$, respectively. The wave vector $\vec{k}$ is therefore represented

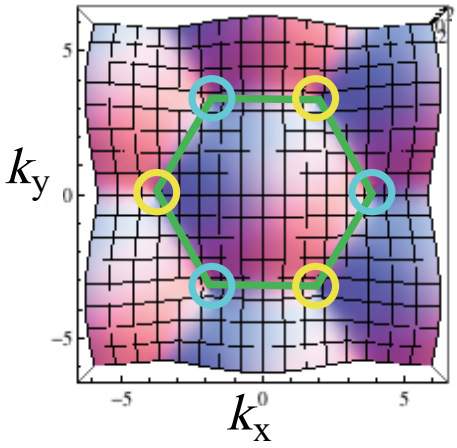

Figure 2.2: The first Brillouin zone in the momentum space. The green hexagon indicates the first Brillouin zone. The yellow circles and the blue circles represent the K and K' points, respectively.

by

$$\vec{k} = \frac{m_1}{N_1}\vec{b}_1 + \frac{m_2}{N_2}\vec{b}_2, \tag{2.6}$$

where $m_1 = 0, 1, \ldots, (N_1 - 1)$ and $m_2 = 0, 1, \ldots, (N_2 - 1)$. The electron states of the wave vector $\vec{k}$ can be represented by

$$|\vec{k}; l\rangle = \frac{1}{\sqrt{N_1 N_2}} \sum_{\vec{R}} e^{i\vec{k}\cdot\vec{R}} |\vec{R}; l\rangle. \tag{2.7}$$

We here denote the summation $\sum_{n_1=1}^{N_1} \sum_{n_2=N_2}^{N_2}$ by $\sum_{\vec{R}}$. We rewrite the tight-binding Hamiltonian in the wave-vector representation with the inverse Fourier transformation:

$$\begin{aligned} |\vec{R}; l\rangle &= \frac{1}{\sqrt{N_1 N_2}} \sum_{\vec{k}} e^{-i\vec{k}\cdot\vec{R}} |\vec{k}; l\rangle, \\ \langle \vec{R}; l | \vec{R}'; l' \rangle &= \delta_{\vec{R},\vec{R}'} \delta_{l,l'}. \end{aligned} \tag{2.8}$$

We thereby obtain the Hamiltonian in the wave-vector representation

$$\begin{aligned} H_1 = t_1 \sum_{\vec{k}} \Big[&\left(1 + e^{i\vec{k}\cdot\vec{a}_1} + e^{i\vec{k}\cdot\vec{a}_2}\right) |\vec{k}; A\rangle\langle\vec{k}; B| \\ &+ \left(1 + e^{-i\vec{k}\cdot\vec{a}_1} + e^{-i\vec{k}\cdot\vec{a}_2}\right) |\vec{k}; B\rangle\langle\vec{k}; A| \Big]. \end{aligned} \tag{2.9}$$

This is block diagonalized into $\vec{k}$ subspaces. The eigenvalue equation in each subspace

$$H_1|\psi_{\vec{k}}\rangle = E(\vec{k})|\psi_{\vec{k}}\rangle \tag{2.10}$$

is given by a 2×2 matrix $h_1(\vec{k})$ and the coefficients $C^A_{\vec{k}}$ and $C^B_{\vec{k}}$ in the form

$$h_1(\vec{k}) \begin{pmatrix} C^A_{\vec{k}} \\ C^B_{\vec{k}} \end{pmatrix} = E(\vec{k}) \begin{pmatrix} C^A_{\vec{k}} \\ C^B_{\vec{k}} \end{pmatrix}, \tag{2.11}$$

where

$$h_1(\vec{k}) = t_1 \begin{pmatrix} 0 & 1 + e^{i\vec{k}\cdot\vec{a}_1} + e^{i\vec{k}\cdot\vec{a}_2} \\ 1 + e^{-i\vec{k}\cdot\vec{a}_1} + e^{-i\vec{k}\cdot\vec{a}_2} & 0 \end{pmatrix}. \tag{2.12}$$

We can solve Eq. (2.12) analytically and obtain the eigenvalues

$$E_{\pm}(\vec{k}) = \pm t_1 \sqrt{3 + 2\cos(ak_x) + 4\cos(\frac{1}{2}ak_x)\cos(\frac{\sqrt{3}}{2}ak_y)}; \tag{2.13}$$

see Fig. 2.3 (a). The eigenvalues greater than zero are in the conduction

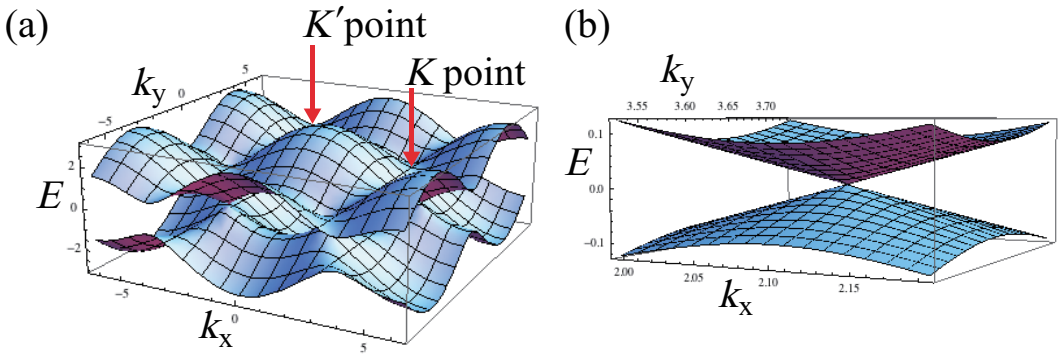

Figure 2.3: **(a)** The energy spectrum of graphene given by the tight-binding model on a honeycomb lattice. The red arrows represent the K and K' points. **(b)** The linear dispersion close to the Fermi energy. The Dirac points exists at the K and K' points. In both figures we set the hopping element t_1 and the lattice constant a to unity.

band and the ones less than zero are in the valence band. The two bands

touch each other at the Fermi energy 0 at the two points K and K' given by

$$\vec{K} = \frac{2\pi}{3a}\begin{pmatrix}1\\ \sqrt{3}\end{pmatrix}, \quad \vec{K}' = \frac{2\pi}{3a}\begin{pmatrix}-1\\ \sqrt{3}\end{pmatrix}; \tag{2.14}$$

see Fig. 2.2. Because the matrix h_1 in (2.12) should be zero at the K and K' points, we have

$$\begin{aligned} 1 + e^{\pm i\vec{K}\cdot\vec{a}_1} + e^{\pm i\vec{K}\cdot\vec{a}_2} &= 0 \\ 1 + e^{\pm i\vec{K}'\cdot\vec{a}_1} + e^{\pm i\vec{K}'\cdot\vec{a}_2} &= 0. \end{aligned} \tag{2.15}$$

Around these two points the energy spectrum can be approximated linearly as shown in Fig. 2.3 (b), which is known as the Dirac cone. We focus on it in the next subsection.

2.1.2 Linear dispersion

In ordinary crystals, the energy spectrum close to the Fermi energy is represented by parabolic curves [78]. However, the spectrum of graphene close to the Fermi energy is approximated well by a linear dispersion [1, 6]. We represent a wave vector $\vec{k}$ close to the K point as $\vec{k} = \vec{K} + \vec{\kappa}$. The following argument is almost the same for the K' point.

The non-diagonal elements in Eq. (2.12) are approximated by the expansions

$$\begin{aligned} &1 + e^{i\vec{k}\cdot\vec{a}_1} + e^{i\vec{k}\cdot\vec{a}_2} = 1 + e^{i(\vec{K}+\vec{\kappa})\cdot\vec{a}_1} + e^{i(\vec{K}+\vec{\kappa})\cdot\vec{a}_2} \\ &= 1 + e^{i\frac{4}{3}\pi}e^{i\vec{\kappa}\cdot\vec{a}_1} + e^{i\frac{2}{3}}e^{i\vec{\kappa}\cdot\vec{a}_2} \\ &\simeq 1 + e^{i\frac{4}{3}\pi}(1 + i\vec{\kappa}\cdot\vec{a}_1) + e^{i\frac{2}{3}\pi}(1 + i\vec{\kappa}\cdot\vec{a}_2) \\ &= -i\frac{\sqrt{3}}{2}a\kappa_y + \frac{\sqrt{3}}{2}a\kappa_x = \frac{\sqrt{3}}{2}a(\kappa_x - i\kappa_y) \end{aligned} \tag{2.16}$$

and

$$1 + e^{-i\vec{k}\cdot\vec{a}_1} + e^{-i\vec{k}\cdot\vec{a}_2} \simeq \frac{\sqrt{3}}{2}a(\kappa_x + i\kappa_y). \tag{2.17}$$

The matrix h_1 is therefore represented by the Pauli matrices σ_x and σ_y:

$$h_1(\vec{K} + \vec{\kappa}) \simeq \frac{\sqrt{3}}{2}at_1\begin{pmatrix}0 & \kappa_x - i\kappa_y\\ \kappa_x + i\kappa_y & 0\end{pmatrix} = v_0(\kappa_x\sigma_x + \kappa_y\sigma_y), \tag{2.18}$$

where $v_0 = \frac{\sqrt{3}}{2}at_1$ is the group velocity. The matrix close to the K' point is also represented by the Pauli matrices as

$$h_1(\vec{K}' + \vec{\kappa}) \simeq \frac{\sqrt{3}}{2}at_1 \begin{pmatrix} 0 & -\kappa_x - i\kappa_y \\ -\kappa_x + i\kappa_y & 0 \end{pmatrix} = v_0(-\kappa_x\sigma_x + \kappa_y\sigma_y). \quad (2.19)$$

The effective Hamiltonian around the K point is given by replacing $\kappa_x \to -i\hbar\,(\partial/\partial x)$ and $\kappa_y \to -i\hbar\,(\partial/\partial y)$:

$$h_1 = \hbar v_0 \left(-i\sigma_x \frac{\partial}{\partial x} - i\sigma_y \frac{\partial}{\partial y}\right), \quad (2.20)$$

which is known as the Dirac Hamiltonian [1, 6]. The eigenstate and the eigenenergy are given by

$$\Psi_{s,\vec{\kappa}}(\vec{r}) = \frac{1}{\sqrt{2}} \begin{pmatrix} 1 \\ se^{i\theta_{\vec{\kappa}}} \end{pmatrix} e^{i\vec{\kappa}\cdot\vec{r}} \quad (2.21)$$

and

$$E_s(\vec{\kappa}) = s\hbar v_0 \left|\vec{\kappa}\right|, \quad (2.22)$$

respectively, where $\theta_{\vec{\kappa}}$ is the polar angle of the wave vector $\vec{\kappa}$ and $s = \pm 1$ is the pseudospin. Note that the vector $\vec{\kappa}$ is measured from the K point. The pseudospin $s = +1$ corresponds to the excitation in the conduction band and $s = -1$ corresponds to the excitation in the valence band. The eigenenergy shows that the energy spectrum is linear with respect to the wave vector $\vec{\kappa}$ (see Fig. 2.3 (b)). The linear dispersion is a characteristic structure in the low-energy region of graphene.

2.2 Quasiperiodicity

In this thesis, we often use quasiperiodic and double-periodic functions for the superlattice potential. We here introduce these concepts as a basis of our study.

Quasiperiodic functions have been used to study quasiperiodic systems which is a theoretical model of quasicrystals [64,65,67,68]. Researchers have tried to apply the quasiperiodicity for wide variety of fields. For example, recent studies reported photonic quasicrystals [79] and polymeric quasicrystals [80]. Today the concept of quasiperiodicity appears in various areas of physics.

2.2.1 Quasiperiodic functions

We first define the quasiperiodicity based on the definition given by Baake [69] and Maciá [66].

Let a real function $f(x)$ contain incommensurate waves:

$$f(x) = \sum_i \left(a_i \cos(\alpha_i x) + b_i \sin(\alpha_i x)\right), \tag{2.23}$$

where a_i and b_i are the real constants and each frequency α_i is an irrational number. When the number of the summation is countably infinite, we refer to $f(x)$ as an almost periodic function. When the number of the summation is finite, we refer to it as a quasiperiodic function. The simplest example is

$$f(x) = \sin(2\pi x) + \sin\left(\frac{2\pi}{\alpha} x\right), \tag{2.24}$$

where α is an irrational number. The Fourier transformation of a quasiperiodic function shows the incommensurate frequencies.

The most important feature of the quasiperiodic function is that it never has the periodicity in spite of the summation of periodic functions. Let us show the lack of the periodicity in the above example (2.24). First, the two sine functions obviously have the periodicity. The periods are unity and α, respectively. Since the sine function is periodic, it must satisfy

$$\sin(2\pi(x+n)) = \sin(2\pi x), \tag{2.25}$$

where $n = \pm 1, \pm 2, \pm 3, \ldots$. The other sine function has the following form:

$$\sin\left(\frac{2\pi}{\alpha}(x+n)\right) = \sin\left(\frac{2\pi}{\alpha}x + \frac{2\pi}{\alpha}n\right). \tag{2.26}$$

If the second sine function showed the same periodicity, the phase $2\pi\alpha n$ would have to satisfy

$$\frac{2\pi}{\alpha}n = 2\pi m, \tag{2.27}$$

where $m = \pm 1, \pm 2, \pm 3, \ldots$. We could rewrite the above relation as

$$\alpha = \frac{n}{m}. \tag{2.28}$$

It clearly conflicts with the definition of the irrational number α. Thus the quasiperiodic function $f(x)$ never has the periodicity.

2.2.2 Approximation of a quasiperiodic function

Considering a function without periodicity can be difficult in theoretical and numerical studies. We here show an efficient approximation of quasiperiodic functions by periodic functions with long enough periods.

A quasiperiodic function can be characterized by an irrational number α. Mathematical studies tell us that an irrational number α is approximated well by a rational number $\alpha_\nu = A_\nu/B_\nu$, where the numerator A_ν and the denominator B_ν are integers (see Appendix A) [81]. Any irrational number can be represented by an infinite simple continued fraction [81]

$$\begin{aligned}\alpha_\infty &= b_0 + \cfrac{1}{b_1 + \cfrac{1}{b_2 + \cdots \cfrac{1}{b_{\nu-1} + \cfrac{1}{b_\nu + \cdots}}}} \\ &= [b_0; b_1, b_2, \ldots, b_\nu, \ldots],\end{aligned} \tag{2.29}$$

where $\{b_\nu\}$ are positive integers. A rational number $\alpha_\nu = [b_0, b_1, \ldots, b_\nu] = A_\nu/B_\nu$ converges to the irrational number $\alpha = \alpha_\infty$ in the limit $\nu \to \infty$.

A function which is characterized by a rational number α_ν is a periodic function with the ratio of period α_ν:

$$f_\nu(x) = \sin\left(\frac{2\pi}{A_\nu}x\right) + \sin\left(\frac{2\pi}{B_\nu}x\right). \tag{2.30}$$

The periods A_ν and B_ν are *coprime* integers which approximate an irrational number. The period of the summed function $f_\nu(x)$ is thereby given by $A_\nu \times B_\nu$. We call the function $f_\nu(x)$ a *double-periodic* function. The double-periodic function well approximates the quasiperiodic function as a rational number does an irrational number.

For example, a quasiperiodic function with the golden ratio $\alpha = \left(1+\sqrt{5}\right)/2$ is approximated by double-periodic functions with the series of rational numbers,

$$\frac{A_1}{B_1} = \frac{2}{1}, \quad \frac{A_2}{B_2} = \frac{3}{2}, \quad \frac{A_3}{B_3} = \frac{5}{3}, \quad \frac{A_4}{B_4} = \frac{8}{5}, \quad \frac{A_5}{B_5} = \frac{13}{8}, \tag{2.31}$$

and so on.

2.3 Tight-binding Hamiltonian with a superlattice potential

When graphene is put on a superlattice membrane, the on-site potential changes because of the electrostatic potential. We here apply the tight-binding approximation in order to represent graphene under superlattice potentials.

For simplicity, we add an external potential along the $\vec{a}_1$ direction to construct a superlattice structure with period L. A unit cell of graphene under a superlattice potential is defined as $(L\vec{a}_1) \times \vec{a}_2$ (see Fig. 2.4). There

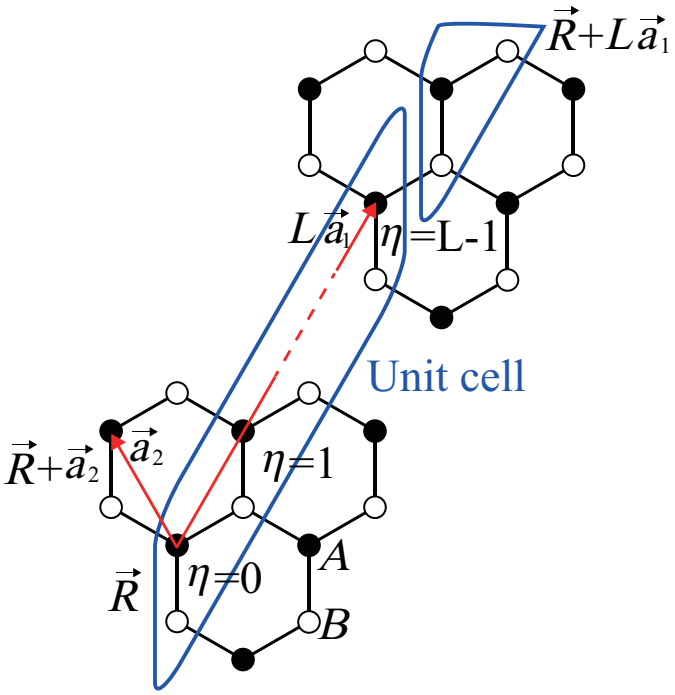

Figure 2.4: A unit cell of graphene superlattice. The area encircled by a blue line represents a unit cell. The red arrows represent the lattice vectors $L\vec{a}_1$ and $\vec{a}_2$. We distinguish the atoms in one unit cell by the symbols $\eta = 0, 1, \ldots, (L-1)$ and $l = A, B$.

are $2 \times L$ carbon atoms in a unit cell; the number of sublattices is also two for graphene under the superlattice potential. The position of a unit cell is

represented by

$$\vec{R} = n_1(L\vec{a}_1) + n_2\vec{a}_2, \tag{2.32}$$

where n_1 and n_2 are integers. We set the periodic boundary conditions in order to treat the system numerically; the integers n_1 and n_2 are thereby restricted to $n_1 = 0, 1, \ldots, (N_1/L) - 1$ and $n_2 = 0, 1, \ldots, N_2 - 1$, respectively. In a unit cell, the wave functions for the tight-binding model is represented as

$$|\psi_{\vec{k}}\rangle = \sum_{\eta} \sum_{l} C_{\vec{k}}^{\eta,l} \, |\vec{k}; \eta, l\rangle, \tag{2.33}$$

where $C_{\vec{k}}^{\eta,l}$ are coefficients and $|\vec{k}; \eta, l\rangle$ is the Fourier transform of $|\vec{R}; \eta, l\rangle$, which is the electronic wave function on a carbon atom in a unit cell $\vec{R}$:

$$|\vec{k}; \eta, l\rangle = \frac{1}{\sqrt{(N_1/L)N_2}} \sum_{\vec{R}} e^{i\vec{k}\cdot\vec{R}} |\vec{R}; \eta, l\rangle \tag{2.34}$$

and

$$|\vec{R}; \eta, l\rangle = \frac{1}{\sqrt{(N_1/L)N_2}} \sum_{\vec{k}} e^{-i\vec{k}\cdot\vec{R}} |\vec{k}; \eta, l\rangle. \tag{2.35}$$

We use the indices $\eta = 0, 1, \ldots, (L-1)$ and $l = \mathrm{A}, \mathrm{B}$ to denote a set of $2L$ carbon atoms in one unit cell; see Fig. 2.4.

The wave vector $\vec{k}$ is given by

$$\vec{k} = \frac{m_1}{N_1/L} \left(\frac{\vec{b}_1}{L} \right) + \frac{m_2}{N_2} \vec{b}_2, \tag{2.36}$$

where $m_1 = 0, 1, \ldots, (N_1/L) - 1$ and $m_2 = 0, 1, \ldots, N_2 - 1$. The supercell Brillouin zone is therefore defined as $\left(\vec{b}_1/L\right) \times \vec{b}_2$; see Fig. 2.5. Because of the superlattice potential with the period L, there are $2 \times L$ states for a wave vector $\vec{k}$. The Brillouin zone is narrowed in the direction of $\vec{b}_1$ vector.

The Hamiltonian of the hopping term for graphene under a superlattice

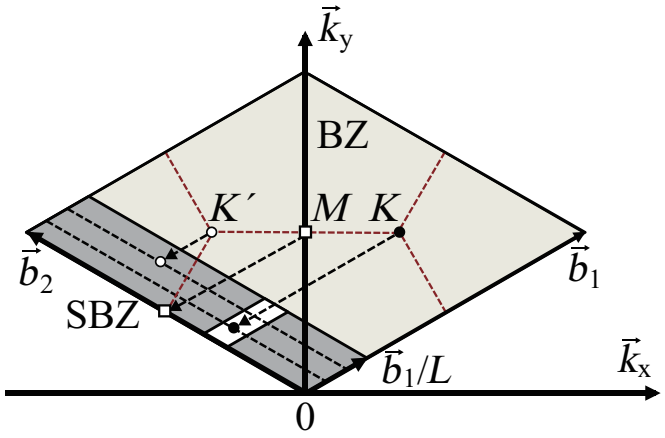

Figure 2.5: A schematic view of the supercell Brillouin zone (SBZ) (the dark gray parallelogram). The light gray area is the first Brillouin zone (BZ) of graphene without an external potential. The red broken lines represent the hexagonal Brillouin zone. The broken arrows represent the reposition of the K (the dark circle), K' (the white circle), and M (the white square) points. The band structure in the white area is illustrated in Fig. 3.1. The dark broken lines represent $(1/3) \times (\vec{b}_1/L)$ and $(2/3) \times (\vec{b}_1/L)$. The relocation of the K and K' points depends on the period of the potential (see Appendix B).

potential is represented as

$$\begin{aligned} H_1 = & \sum_{\vec{R}} \sum_{\eta=0}^{L-2} t_1 \Big(|\vec{R};\eta,B\rangle\langle\vec{R};\eta,A| + |\vec{R};\eta+1,B\rangle\langle\vec{R};\eta,A| \\ & + |\vec{R}+\vec{a}_2;\eta,B\rangle\langle\vec{R};\eta,A| \Big) \\ & + t_1 \Big(|\vec{R};L-1,B\rangle\langle\vec{R};L-1,A| + |\vec{R}+L\vec{a}_1;0,B\rangle\langle\vec{R};L-1,A| \\ & + |\vec{R}+\vec{a}_2;L-1,B\rangle\langle\vec{R};L-1,A| \Big) \\ & + (\text{h.c.}). \end{aligned} \tag{2.37}$$

We rewrite the hopping Hamiltonian by using the following relations:

$$\sum_{\vec{R}} |\vec{R};\eta,B\rangle\langle\vec{R};\eta',A| = \sum_{\vec{k}} |\vec{k};\eta,B\rangle\langle\vec{k};\eta',A|, \tag{2.38}$$

$$\sum_{\vec{R}} |\vec{R}+\vec{a}_2;\eta,B\rangle\langle\vec{R};\eta,A| = \sum_{\vec{k}} e^{-i\vec{k}\cdot\vec{a}_2}|\vec{k};\eta,B\rangle\langle\vec{k};\eta,A|, \tag{2.39}$$

and

$$\sum_{\vec{R}} |\vec{R}+L\vec{a}_1;0,B\rangle\langle\vec{R};L-1,A| = \sum_{\vec{k}} e^{-i\vec{k}\cdot(L\vec{a}_1)}|\vec{k};0,B\rangle\langle\vec{k};L-1,A|. \tag{2.40}$$

We thus obtain the hopping term in the wave-vector representation:

$$\begin{aligned} H_1 = t_1 \sum_{\vec{k}} \sum_{\eta=0}^{L-2} & \left(1+e^{-i\vec{k}\cdot\vec{a}_2}\right)|\vec{k};\eta,B\rangle\langle\vec{k};\eta,A| + |\vec{k};\eta+1,B\rangle\langle\vec{k};\eta,A| \\ & + \Big[\left(1+e^{-i\vec{k}\cdot\vec{a}_2}\right)|\vec{k};L-1,B\rangle\langle\vec{k};L-1,A| \\ & + e^{-i\vec{k}\cdot(L\vec{a}_1)}|\vec{k};0,B\rangle\langle\vec{k};L-1,A|\Big] \\ & + (\text{h.c.}). \end{aligned} \tag{2.41}$$

We write down the potential term in both cases of the single-periodic and the double-periodic potentials. First we add a sine function with the period L along the $\vec{a}_1$ direction for the single-periodic potentials. The potential term is given by

$$\begin{aligned} V &= v\sum_{\vec{R}}\sum_{\eta=0}^{L-1}\sum_{l=A,B} \sin\left[\vec{k}_{\rm s}\cdot\left(\vec{R}+\eta\vec{a}_1\right)\right]|\vec{R};\eta,l\rangle\langle\vec{R};\eta,l| \\ &= v\sum_{\eta=0}^{L-1}\sin\left(\vec{k}_{\rm s}\cdot\eta\vec{a}_1\right)\sum_{\vec{k}}\sum_{l=A,B}|\vec{k};\eta,l\rangle\langle\vec{k};\eta,l|, \end{aligned} \tag{2.42}$$

where v is the strength of the function and $\vec{k}_{\rm s}$ is the wave vector $\vec{k}_{\rm s}=\vec{b}_1/L$. Second we add two sine functions V_1 and V_2 along the $\vec{a}_1$ direction with the periods L_1 and L_2, respectively. We rewrite the potential term in the double-periodic case $V=V_1+V_2$:

$$\begin{aligned} V &= \sum_{j=1}^{2} v_j \sum_{\vec{R}}\sum_{\eta=0}^{L-1}\sum_{l=A,B} \sin\left[\vec{k}_j\cdot\left(\vec{R}+\eta\vec{a}_1\right)\right]|\vec{R};\eta,l\rangle\langle\vec{R};\eta,l| \\ &= \sum_{j=1}^{2} v_j \sum_{\eta=0}^{L-1}\sin\left(\vec{k}_j\cdot\eta\vec{a}_1\right)\sum_{\vec{k}}\sum_{l=A,B}|\vec{k};\eta,l\rangle\langle\vec{k};\eta,l|, \end{aligned} \tag{2.43}$$

where v_j are the strengths of the sine functions and $\vec{k}_j = \vec{b}_1/L_j$ for $j = 1, 2$. We obtain the energy spectrum by solving the eigenvalue equation which includes the hopping term (2.41) and the potential term (2.42) or (2.43).

Chapter 3

Single-periodic potentials

We first review the generation of new Dirac cones, indexed by integers $n = \pm 1, \pm 2, \ldots$, in the Dirac Hamiltonian under a single-periodic superlattice potential, which was reported by Park *et al.* [52, 53]. Our numerical calculation of graphene under a periodic potential is consistent with the previous study to some extent. However, we here report two differences: first, the appearance is discontinued around $|E| \sim t_1$; second, the amplitude and the period of the superlattice potential affect the maximum possible value of the index.

3.1 Generation of new Dirac cones under the single-periodic potentials

We review the theory that shows the generation of new massless Dirac electrons by analyzing the Dirac Hamiltonian under single-periodic potentials [52, 53]. The Dirac Hamiltonian under a superlattice potential $V(x, y)$ is given by

$$h\left[V\right] = \hbar v_0 \left(-i\sigma_x \frac{\partial}{\partial x} - i\sigma_y \frac{\partial}{\partial y} \right) + IV(x, y), \tag{3.1}$$

where v_0 is the group velocity, σ_x and σ_y are the Pauli matrices, and I is the identity matrix. This Hamiltonian has been used to study the energy spectrum near the Fermi energy of graphene under a periodic potential [52, 53, 62].

Let us simplify the problem by assuming an external potential varying along the x direction, which corresponds to the $\vec{a}_1$ direction for the graphene

on the hexagonal lattice:

$$V(x+L) = V(x), \quad \text{or} \quad V(\vec{r} + L\vec{a}_1) = V(\vec{r}). \tag{3.2}$$

We transform the Hamiltonian (3.1) using the integral of the superlattice potential

$$\alpha(x) = \frac{2}{\hbar v_0} \int_0^x V(x')dx' \tag{3.3}$$

and a unitary matrix

$$U_1 = \frac{1}{\sqrt{2}} \begin{pmatrix} e^{-i\alpha(x)/2} & -e^{+i\alpha(x)/2} \\ e^{-i\alpha(x)/2} & e^{+i\alpha(x)/2} \end{pmatrix}. \tag{3.4}$$

We thereby obtain the transformed Hamiltonian:

$$h' = U_1^\dagger h[V] U_1 = \hbar v_0 \begin{pmatrix} -i\frac{\partial}{\partial x} & -e^{+i\alpha(x)}\frac{\partial}{\partial y} \\ e^{-i\alpha(x)}\frac{\partial}{\partial y} & i\frac{\partial}{\partial x} \end{pmatrix}. \tag{3.5}$$

The electronic states of a quantum system with translational symmetry are given by the Bloch wave functions. A wave function $\psi_{\vec{k}}(\vec{r})$ is given by the multiple of the plane wave and a periodic function:

$$\psi_{\vec{k}}(\vec{r}) = e^{i\vec{k}\cdot\vec{r}} f_{\vec{k}}(\vec{r}), \tag{3.6}$$

where $f_{\vec{k}}(\vec{r}) = f_{\vec{k}}(\vec{r} + \vec{L})$ is a periodic function with period $\vec{L}$. The periodic function is represented by the Fourier expansion:

$$f_{\vec{k}}(\vec{r}) = \sum_{j=-\infty}^{+\infty} C_j(\vec{k}) e^{i\vec{G}\cdot\vec{r}}, \tag{3.7}$$

where $\vec{G}$ is a reciprocal vector of the system with an external potential and $C_j(\vec{k})$ is a coefficient. In the particular case of Eq. (3.2), the reciprocal vector is given by $\vec{G} = \vec{b}_1/L$.

We hence introduce a basis set of plane-wave spinors to obtain the eigenstates and eigenenergies of the Hamiltonian h' in (3.5). We here focus on the generation of new Dirac cones close to the wave vector $\vec{k} = \left(\vec{G}n\right)/2 + \vec{\kappa}$. We therefore reduce the matrix h' into a 2×2 matrix by using the following two electron states as bases:

$$\vec{u}_1 = \begin{pmatrix} 1 \\ 0 \end{pmatrix}' e^{i\left(\frac{\vec{G}}{2}n + \vec{\kappa}\right)\cdot\vec{r}} \tag{3.8}$$

and

$$\vec{u}_2 = \begin{pmatrix} 0 \\ 1 \end{pmatrix}' e^{-i\left(\frac{\vec{G}}{2}n-\vec{\kappa}\right)\cdot\vec{r}}, \tag{3.9}$$

where n is an integer and $\vec{\kappa} = (\kappa_x, \kappa_y)$ is the wave vector which is defined as $|\vec{\kappa}| \ll (2\pi)/L$. We note that the spinors

$$\begin{pmatrix} 1 \\ 0 \end{pmatrix}', \quad \begin{pmatrix} 0 \\ 1 \end{pmatrix}' \tag{3.10}$$

are defined for the matrix h'. We use the prime to distinguish the spinor bases of the transformed matrix h' in (3.5) from that of the matrix h in (3.1).

Operating the transformed Hamiltonian h' on the states $\vec{u}_1$, we obtain the following relation:

$$h'\vec{u}_1 = \hbar v_0 \begin{pmatrix} -i\frac{\partial}{\partial x} \\ e^{-i\alpha}\frac{\partial}{\partial y} \end{pmatrix}' e^{i\left(\frac{\vec{G}}{2}n+\vec{\kappa}\right)\cdot\vec{r}} = \hbar v_0 \begin{pmatrix} \frac{G}{2}n + \kappa_x \\ i\kappa_y \sum_l f_l e^{-ilGx} \end{pmatrix}' e^{i\left(\frac{\vec{G}}{2}n+\vec{\kappa}\right)\cdot\vec{r}}, \tag{3.11}$$

where $G = |\vec{G}| = 2\pi/L$ and we introduced the following expansion:

$$e^{i\alpha(x)} = \sum_{l=-\infty}^{+\infty} f_l[V] e^{ilGx} \tag{3.12}$$

with real coefficients f_l. We here focus on a matrix which is obtained by the bases $\vec{u}_1$ and $\vec{u}_2$ in (3.8) and (3.9), respectively. In Eq. (3.11), we only consider the term $l = n$ to obtain the states with the wave vector $\vec{k} = -\left(\vec{G}n\right)/2 + \vec{\kappa}$:

$$f_n e^{-inGx}\left(i\kappa_y\right) e^{i\left(\frac{\vec{G}}{2}n+\vec{\kappa}\right)\cdot\vec{r}} = f_n\left(i\kappa_y\right) e^{-i\left(\frac{\vec{G}}{2}n-\vec{\kappa}\right)\cdot\vec{r}}. \tag{3.13}$$

Thus we obtain an approximation of $h'\vec{u}_1$ for the states around $\left(\vec{G}n\right)/2$:

$$\begin{aligned} &\hbar v_0 \left(\frac{G}{2}n + \kappa_x\right) \begin{pmatrix} 1 \\ 0 \end{pmatrix}' e^{i\left(\frac{G}{2}n+\vec{\kappa}\right)\cdot\vec{r}} + \hbar v_0 f_n\left(i\kappa_y\right) \begin{pmatrix} 0 \\ 1 \end{pmatrix}' e^{-i\left(\frac{\vec{G}}{2}n-\kappa\right)\cdot\vec{r}} \\ &= \hbar v_0 \left(\frac{G}{2}n + \kappa_x\right) \vec{u}_1 + \hbar v_0\left(i f_n \kappa_y\right) \vec{u}_2. \end{aligned} \tag{3.14}$$

We can rewrite the relation $h'\vec{u}_2$ around the wave vector $\left(\vec{G}n\right)/2$ similarly. First we operate the matrix h' on the basis $\vec{u}_2$:

$$h'\vec{u}_2 = \hbar v_0 \begin{pmatrix} \left(\sum_l f_l e^{+ilGx}\right)(-i\kappa_y) \\ \frac{G}{2}n - \kappa_x \end{pmatrix}' e^{-i\left(\frac{\vec{G}}{2}n - \vec{\kappa}\right)\cdot\vec{r}}. \tag{3.15}$$

We obtain an approximation of $h'\vec{u}_2$ by considering again the term with $l = n$:

$$\hbar v_0 \left(-if_n\kappa_y\right)\vec{u}_1 + \hbar v_0 \left(\frac{G}{2}n - \kappa_x\right)\vec{u}_2. \tag{3.16}$$

We thus obtain a 2×2 matrix M as an approximation of the Hamiltonian h' under the condition that the wave vector $\vec{\kappa}$ is very close to $\left(\vec{G}n\right)/2$:

$$\begin{aligned} M &= \hbar v_0 \begin{pmatrix} \frac{G}{2}n + \kappa_x & -i\kappa_y f_n \\ i\kappa_y f_n & \frac{G}{2}n - \kappa_x \end{pmatrix} \\ &= \hbar v_0 \left(\kappa_x\sigma_z + f_n\kappa_y\sigma_y\right) + \hbar v_0 \left(\frac{G}{2}n\right) I. \end{aligned} \tag{3.17}$$

We further transform (3.17) by using the following unitary matrix U_2 to show that the approximated energy spectrum is linear around $\left(\vec{G}n\right)/2$:

$$U_2 = \frac{1}{\sqrt{2}} \begin{pmatrix} 1 & 1 \\ -1 & 1 \end{pmatrix} = \frac{1}{\sqrt{2}} \left(I + i\sigma_y\right). \tag{3.18}$$

The result is

$$M' = U_2^\dagger M U_2 = \hbar v_0 \left(\kappa_x\sigma_x + f_n\kappa_y\sigma_y\right) + \hbar v_0 \frac{G}{2} nI, \tag{3.19}$$

where we used the relations

$$\left(I - i\sigma_y\right)\sigma_z\left(I + i\sigma_y\right) = \left(\sigma_z + \sigma_x\right)\left(I + i\sigma_y\right) = \sigma_z + \sigma_x + \sigma_x - \sigma_z = 2\sigma_x, \tag{3.20}$$

$$\left(I - i\sigma_y\right)\sigma_y\left(I + i\sigma_y\right) = \left(\sigma_y - iI\right)\left(I + i\sigma_y\right) = \sigma_y + iI - iI + \sigma_y = 2\sigma_y, \tag{3.21}$$

and

$$\left(I - i\sigma_y\right) I \left(I + i\sigma_y\right) = I + i\sigma_y - i\sigma_y + I = 2I. \tag{3.22}$$

The matrix (3.19) except for the constant term is similar to the Dirac Hamiltonian (2.20). In fact the matrix M' has the eigenenergy

$$E_s\left(\vec{\kappa}\right) = s\hbar v_0 \sqrt{\kappa_x^2 + \left|f_n\right|^2 \kappa_y^2} + \frac{hv_0}{2} Gn, \tag{3.23}$$

where $s = \pm 1$ represents the two bands. The second term represents the center of the new Dirac cones, namely the new Dirac points. They appear at

$$\vec{G}_0(n) \equiv \frac{n}{L}\vec{b}_1, \quad n = 0, \pm 1, \pm 2, \ldots . \tag{3.24}$$

in the wave-number space at the energy levels $\hbar v_0 G n/2$. The effect of the potential f_m gives the gradient of the energy spectrum in the κ_y direction. This is because we added an external potential with the periodicity along the x direction; the periodicity in the y direction would result in the gradient change in the κ_x direction.

We will numerically confirm the appearance of the new Dirac-electron structures on the basis of the tight-binding model with the single-periodic potentials (3.2). In this particular case, $\vec{G} = |\vec{b}_1|/L$ with $|\vec{b}_1| = 4\pi/(\sqrt{3}a) = 4\pi/\sqrt{3}$, while group velocity v_0 is $(\sqrt{3}/2)at_1 = \sqrt{3}/2$, where we set the lattice constant a, the hopping element t_1 of the tight-binding model, and the Planck constant $\hbar$ all to unity. The energy levels of the Dirac points therefore reduce to

$$\frac{\hbar v_0}{2}\frac{n}{L}\left|\vec{b}_1\right| = \frac{\pi}{L}n. \tag{3.25}$$

Compared to the original Dirac cone ($n = 0$), the new Dirac cones ($n \neq 0$) is skewed as in Eq. (3.23), its gradient in the $\vec{b}_2$ direction being modified by the periodic potential [53]. We will see that the new Dirac-electron structures are tilted far away from the original one at the Fermi energy.

3.2 Numerical analysis

3.2.1 Generation of the Dirac-electron structures in the tight-binding model

Let us numerically check the theoretical prediction (3.25) of the generation of the new Dirac cones. We will reveal that the prediction is realized in the tight-binding model only in a finite energy range around the Fermi energy because the model has a finite band width.

We numerically diagonalized the tight-binding model on the hexagonal lattice with periodic boundary conditions. We use the systems of size from $(r_1, r_2) = (10^2, 10^2)$ to $(10^6, 10^6)$, where r_1 and r_2 denote the numbers of the unit cells in the $\vec{a}_1$ and $\vec{a}_2$ directions, respectively. In this paper, we numerically evaluate whether the band structures are gapless or not within the accuracy of double precision. We applied to the systems the superlattice potential of the form

$$V(\vec{r}) = v \sin\left(\frac{1}{L}\vec{b}_1 \cdot \vec{r}\right), \tag{3.26}$$

where v denotes the amplitude. We used $L = 25$ and $v = 0.25$ throughout the present subsection. We show in Fig. 3.1 the energy spectrum for $r_1 = r_2 = 10^2$ around the K point (see Fig. 2.5). The energy spectrum with the superlattice potential lies in the range $\left|E(\vec{k})\right| < 3t_1 + v = 3.25$. We find many energy bands which are in contact with each other at seeming points, which is consistent with the prediction (3.25). As shown in Fig. 3.1, we label the bands above the Fermi energy by positive integers; note that the spectrum is symmetric with respect to the Fermi energy $E = 0$, which is labeled by $n = 0$.

Let us check the consistency between the theoretical prediction (3.25) and the numerical data in more details. We compare in Table 3.1 the energy of the contact "points" as shown in Fig. 3.1 with the theoretical predictions $(\pi/L) \times n = (0.1256\ldots) \times n$. The numerical data are mostly consistent with the prediction up to $E \simeq t_1$. Note that in pristine graphene the linear dispersions around the K and K' points bend over away from the Fermi energy and meet at M points of the energy $\pm t_1$ (cf. Fig. 2.5). It is therefore reasonable that the theoretical prediction fails for $E > t_1$, or $n > 8$ for $L = 25$. We will indeed find below that the seeming contact "point" for $n = 9$ is spurious and not a gapless Dirac electron.

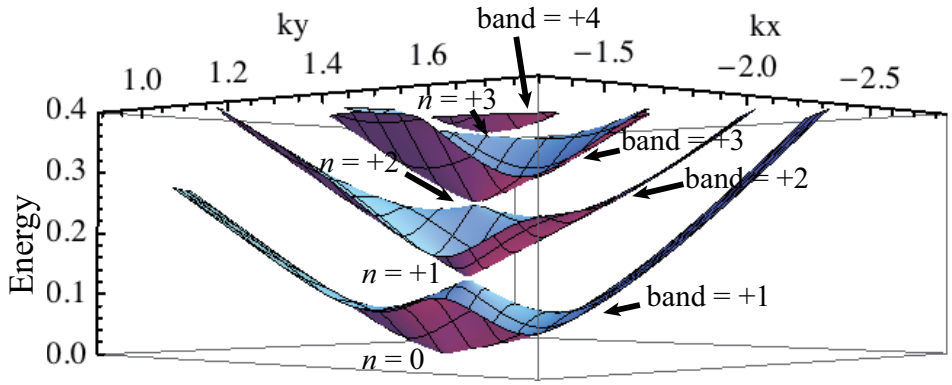

Figure 3.1: The energy spectrum around the K point of the tight-binding model for $L = 25$, $v = 0.25$ and $r_1 = r_2 = 10^2$. Only the positive-energy side is shown here: the spectrum is symmetric with respect to the Fermi energy $E = 0$.

Table 3.1: The energy of the contact "points" for $L = 25$, $v = 0.25$, and $r_1 = r_2 = 10^2$, compared with the energy of the theoretical prediction (3.25). We listed only the data above the Fermi energy $E = 0$.

contact	energy	$(\pi/L) \times n$
$n = 0$	0.00	0.00
$n = +1$	0.13	0.126
$n = +2$	0.25	0.251
$n = +3$	0.37	0.377
$n = +4$	0.49	0.503
$n = +5$	0.61	0.628
$n = +6$	0.72	0.754
$n = +7$	0.83	0.880
$n = +8$	0.93	1.01
$n = +9$	1.03	1.13
$n = +10$	1.13	1.26

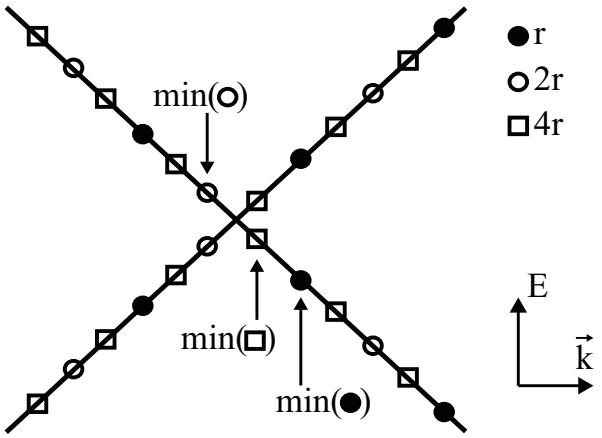

Figure 3.2: A schematic illustration of a possible new Dirac cone and the numerical data points. Solid circles, open circles and open squares indicate the numerical data points for the systems of sizes r, $2r$, and $4r$, respectively. Note that solid circles are on top of half of the open circles and the open circles are on top of the half of the open squares.

In order to show it, we now describe how we evaluate whether the seeming contact "points" correspond to the Dirac-electron structures or not within the numerical accuracy of double precision. Suppose that in the energy range with a Dirac-cone structure, we diagonalize the system of size r and obtain the data points schematically indicated by the solid circle in Fig. 3.2, where we show the spectrum only in one dimension for simplicity. The number of data points in the wave-number space is proportional to the system size, and hence the data points become denser as we increase the system size, as is shown in Fig. 3.2 by the open circles for the system size $2r$ and the solid circles for $4r$.

Let us now focus on the data points indicated as min(•), min(○), and min(□) in Fig. 3.2. They denote the wave numbers where the energy interval between the neighboring eigenvalues for a fixed wave number is the smallest for their respective system size. The minimum energy interval should converge to zero as we increase the system size if the dispersion is indeed linear. As we increase the system size, the minimum energy intervals can show stepwise decreases, as is indeed demonstrated in Fig. 3.3. We can explain it as follows. The wave vector $\vec{k}$ in the first Brillouin zone for the system size

(r_1, r_2) is given by

$$\vec{k} = \frac{l_1}{r_1}\left(\frac{\vec{b}_1}{L}\right) + \frac{l_2}{r_2}\vec{b}_2, \tag{3.27}$$

where $l_1 = 0, 1, \ldots, (r_1 - 1)$ and $l_2 = 0, 1, \ldots, (r_2 - 1)$. For simplicity, let us consider only in the $\vec{b}_1$ direction and assume that a Dirac point in question exists at the wave number $\kappa_1(\vec{b}_1/L)$, where κ_1 is a real constant. In the numerical data for a large system of size r_1, the minimum energy interval is proportional to

$$\kappa_1 - \frac{l_{1,\min}}{r_1}, \tag{3.28}$$

where $l_{1,\min}$ denotes the wave number that gives the minimum energy interval. The minimum energy interval for a larger system of size r_1' should be generally less as in

$$\kappa_1 - \frac{l'_{1,\min}}{r_1'} \leq \kappa_1 - \frac{l_{1,\min}}{r_1}, \tag{3.29}$$

where $l'_{1,\min}$ here denotes the wave number that gives the minimum energy interval for r_1'. However, they can happen to be close to each other when $l_{1,\min}/r_1$ happens to be close to $l'_{1,\min}/r_1'$.

We now show that according to the above judgment rule, the contact "points" $n \leq 8$ are Dirac-electron structures, which we define below in more detail, but $n \geq 9$ are not. Figure 3.4 shows the wave-number dependence of the energy intervals between the neighboring energy eigenvalues around the contact "points" for $n = 8$ and $n = 9$. As we make the data points denser by increasing the system size and at the same time close up the spectrum around the contact point $n = 8$, we still see the linear dispersion. It shows that the energy gap of the contact "point" $n = 8$ is either zero or invisibly small within the accuracy of the present numerical precision. We here refer to the energy spectrum with an invisibly small energy gap a *Dirac-electron structure*. In other words, when we increase the system size further, there are two possibilities that the minimum energy interval of the Dirac-electron structure still decreases or show a finite energy gap. We note that the Dirac-electron structures are quite likely to possess very small energy gaps; we will discuss this point in more detail later. In contrast, the contact "point" $n = 9$ exhibits visible energy gap as explicitly shown in Fig. 3.4 (d).

Figure 3.5 shows a relation between the cone index n and the minimum energy intervals for $L = 25$ and $v = 0.25$. As we increase the system size r,

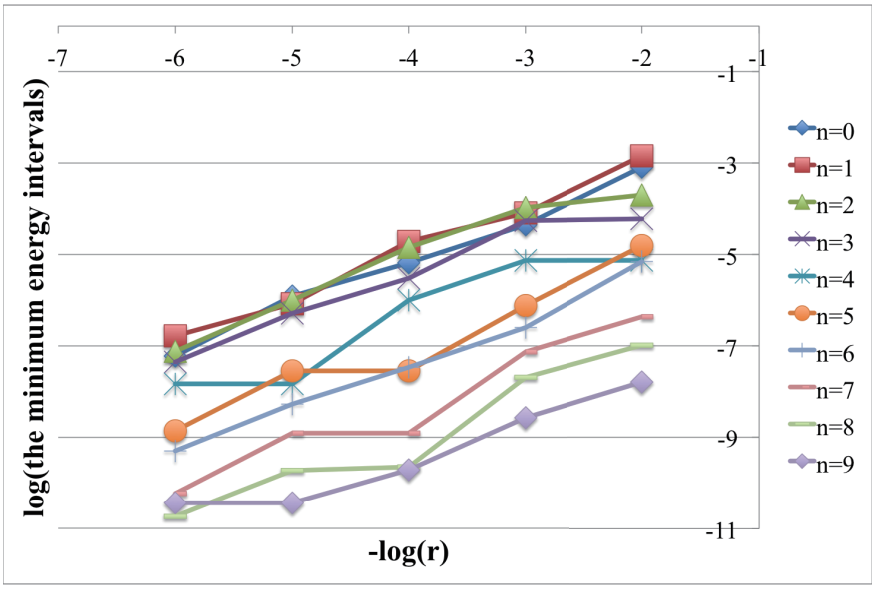

Figure 3.3: A logarithmic plot of the system-size dependence of the minimum energy interval at the contact "points" for $L = 25$ and $v = 0.25$.

the intervals for $n = 9, 10, 11$ converge to small finite values but for $0 \leq n \leq 8$ we cannot completely know from the numerical results whether the contact "points" are exactly gapless or have small finite energy gaps. We thereby refer to the contact "points" $0 \leq n \leq 8$, which are in the energy range $|E| < t_1$, as the Dirac-electron structures, while we refer to the structures for $n \geq 9$ as gapful structures, which are in the energy range $|E| > t_1$. The energy intervals of the Dirac-electron structures are of the order of 10^{-6} at maximum compared to the hopping element t_1, which we put to unity. We can therefore treat the energy structures close to the contact "points" practically as the Dirac cones.

Previous studies by Park and the colleagues [52, 53] revealed the generation of the *gapless* Dirac electrons from the Dirac Hamiltonian, which is an *effective* Hamiltonian for graphene, but they did not rigorously showed that the Dirac cones induced by the superlattice potentials are truly gapless in the tight-binding models. On the other hand, their prediction for the generation of the new Dirac electrons is in good agreement with the experi-

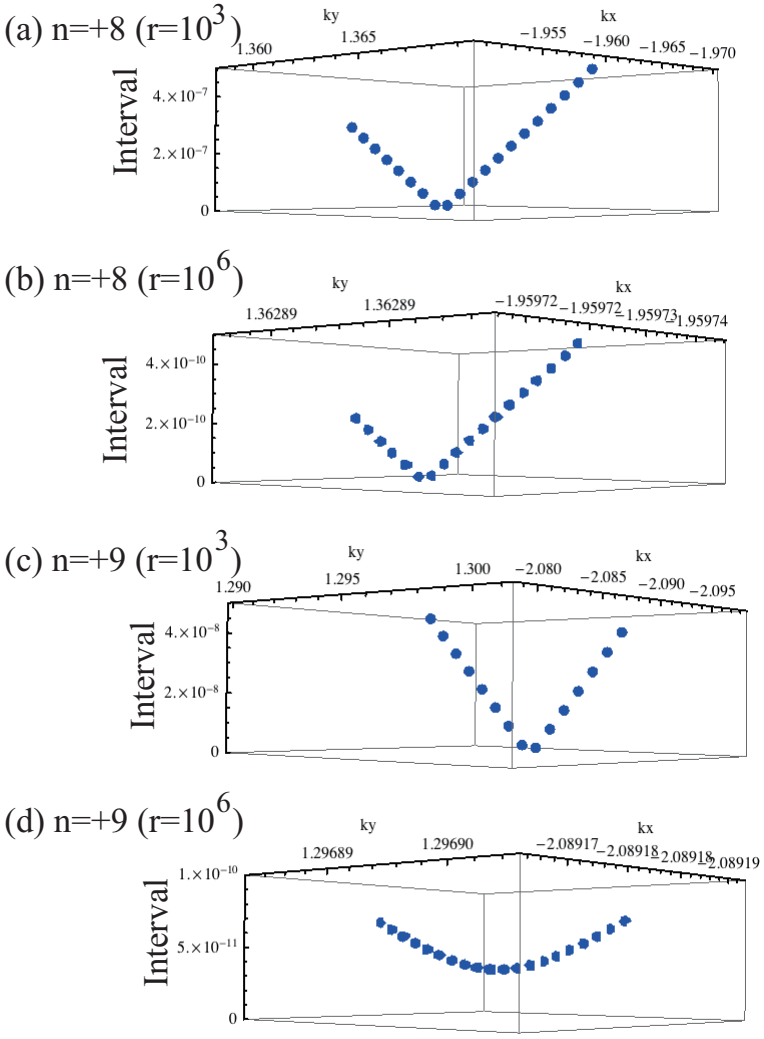

Figure 3.4: The energy intervals of neighboring energy eigenvalues around the contact "points" $n = 8$ ((a) for $r_1 = r_2 = 10^3$ and (b) for 10^6) and $n = 9$ ((c) for $r_1 = r_2 = 10^3$ and (d) for 10^6). Note that the ranges of the wave numbers are all different.

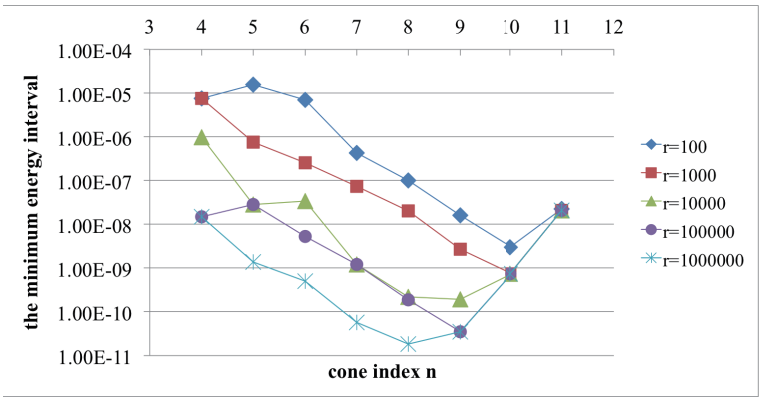

Figure 3.5: A relation between the cone index n and the minimum energy intervals for $r = 10^2$ (blue diamonds), $r = 10^3$ (red squares), $r = 10^4$ (green triangles), $r = 10^5$ (purple circles), and $r = 10^6$ (blue stars).

ential studies of graphene superlattices [26, 31, 38, 40]. From this viewpoint, their effective theory works well in understanding the experimental results although we cannot know whether the new Dirac cones are really gapless or not. We thus expect that our theoretical and numerical results are also effective in realizing behavior of the Dirac-electron structures induced by the superlattice potentials.

3.2.2 Energy cutoff of graphene under the single-periodic potentials

The previous work [52, 53] used the Dirac Hamiltonian and showed the generation of the new Dirac cones independently of the band width and the amplitude of the potential. In Subsection 3.2.1, however, we revealed that in the tight-binding model with an external superlattice potential, the contact "point" between neighboring bands can be Dirac-electron structures only up to an energy cutoff ΔE which is characterized by the band width of the graphene.

When we change the amplitude of the superlattice potential, we can obtain different generation of the Dirac-electron structures. Figures 3.6 shows a relation between the amplitude and the minimum energy intervals of the index $n = 6$ for different system sizes r. As we increase the system size,

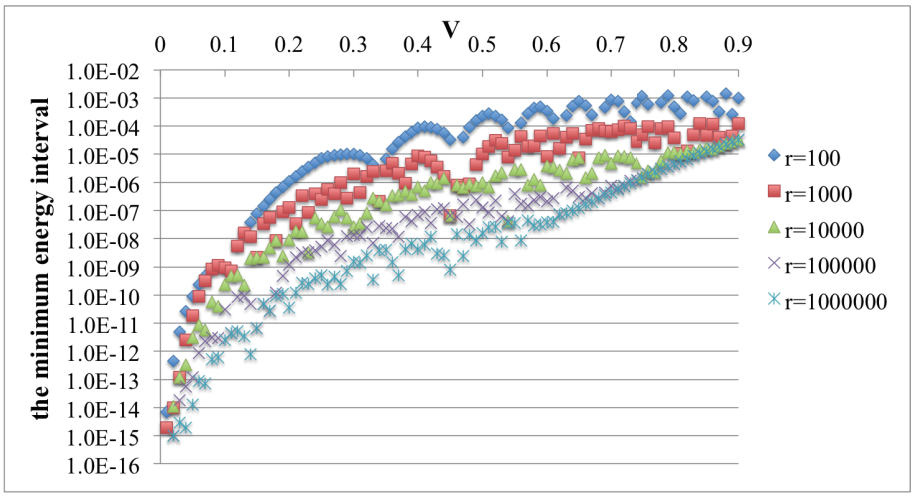

Figure 3.6: A relation between the amplitude and the minimum energy intervals of the index $n = 6$ for $r = 10^2$ (blue diamonds), $r = 10^3$ (red squares), $r = 10^4$ (green triangles), $r = 10^5$ (purple crosses), and $r = 10^6$ (blue stars).

the minimum energy intervals for larger amplitudes converge to finite energy gaps. In a small amplitude region, on the other hand, the intervals continue decreasing as the system size r increases, where we numerically judge that the energy structures are the Dirac-electron structures. The numerical result indicates that the energy cutoff ΔE, which is a borderline between the Dirac-electron structures and the gapful structures, should depend on the amplitude v. In other words, the cone index is consecutive up to a maximum value: $n = 0, \pm 1, \ldots, \pm N(v)$. To be specific, we here define the energy cutoff $\Delta E(v)$ as the minimum energy of the disappeared Dirac-electron structures, namely the lowest spurious contact "point" of the index $N(v) + 1$ in our numerical environment;

$$\Delta E(v) = E(N(v) + 1) \simeq \frac{\pi}{L} (N(v) + 1) , \tag{3.30}$$

where the energy of the Dirac-electron structure $E(N(v)+1)$ is ideally represented by the theoretical analysis (3.25). The maximum index of the Dirac-electron structures is given by the cutoff as

$$N(v) \simeq \left\lfloor \frac{L\Delta E(v)}{\pi} \right\rfloor , \tag{3.31}$$

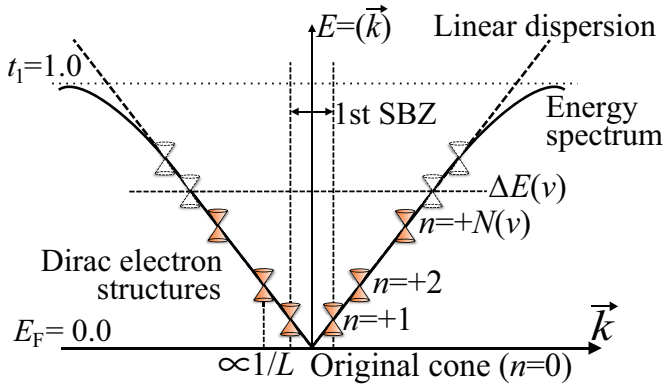

Figure 3.7: A schematic illustration of the appearance of the new Dirac-electron structures around the original Dirac point generated by a periodic potential between the Fermi energy $E_{\rm F}$ (the horizontal solid line) and the hopping element t_1 (the dotted line). The solid lines represent the dispersion of graphene, which deviates from the linear dispersion (the broken diagonal lines). The broken vertical lines indicate the first supercell Brillouin zone (1st SBZ). The new Dirac-electron structures, for the amplitude v, are indexed as $n = 0, \pm 1, \ldots, \pm N(v)$, where $n = 0$ corresponds to the original one. The energy cutoff $\Delta E(v)$ is set as the minimum energy of the disappeared cones, which are illustrated with the broken line. The external potential determines the direction $\vec{k}$ of the generation.

where $\lfloor\, \rfloor$ denotes the floor function. Note that for very weak potentials, we set the energy cutoff to $\Delta E(v) = t_1$ because the Dirac-electron structures never appeared beyond it. We schematically show in Fig. 3.7 the generation of the Dirac-electron structures, illustrating how it is limited by the energy cutoff $\Delta E(v)$ induced by a single-periodic potential. We expect that the energy cutoff $\Delta E(v)$ decreases as the amplitude of the potential increases because the spectrum diverts more from the linear dispersion.

In order to confirm it, we numerically calculate the energy spectra and investigate the generation of the new Dirac-electron structures for the one-dimensional potential of period $L = 25$, changing its amplitude. Figure 3.8 shows relations between the system size r and the minimum energy intervals

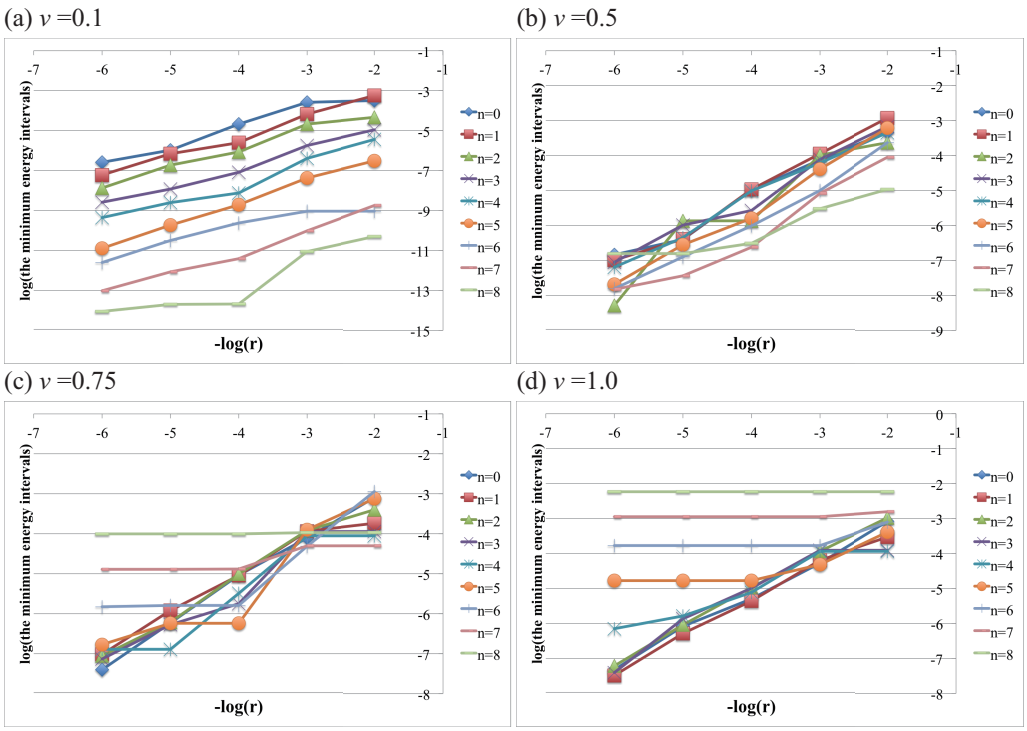

Figure 3.8: Logarithmic plots of the system-size dependence of the minimum energy intervals at the contact "points" for $L = 25$ and (a) $v = 0.1$, (b) $v = 0.5$, (c) $v = 0.75$, and (d) $v = 1.0$. In all plots, we left out the points $n \geq 9$ because their energies are greater than 1.

for (a) $v = 0.1$, (b) $v = 0.5$, (c) $v = 0.75$ (c), and (d) $v = 1.0$; the last case corresponds to $v = t_1$. In all cases, each contact "point" in the range $n \geq 9$ has the energy higher than $t_1 = 1$ and have visibly large energy gaps; we therefore left them out in Fig. 3.8. We notice that some series obviously do not converge to zero as we increase the system size, which implies that the energy cutoff is lowered.

We again judge their trends under the same rule as in Subsection 3.2.1. Figure 3.9 (a) and (b) show the energy intervals around the contact $n = 8$ for $v = 0.5$ with the system sizes $r = 10^3$ and 10^6, respectively. It is clear that the contact "point" $n = 8$ with the amplitude $v = 0.5$ becomes a visibly gapful structure as the potential becomes stronger. We numerically observed that the contact points $n = 0, \ldots, +7$ can be gapless or have invisible small

energy gaps; we thus claim that $N(v = 0.5) = 7$. The same analysis for $v = 0.75$ shows that the point $n = 5$ is a Dirac-electron structure but the one $n = 6$ is not (Fig. 3.9 (c) and (d)). We thus claim that $N(v = 0.75) = 5$. We can similarly have $N(v = 1.0) = 3$. As expected, the maximum index $N(v)$ of the new Dirac-electron structures decreases as the amplitude v of the single-periodic potential gets larger.

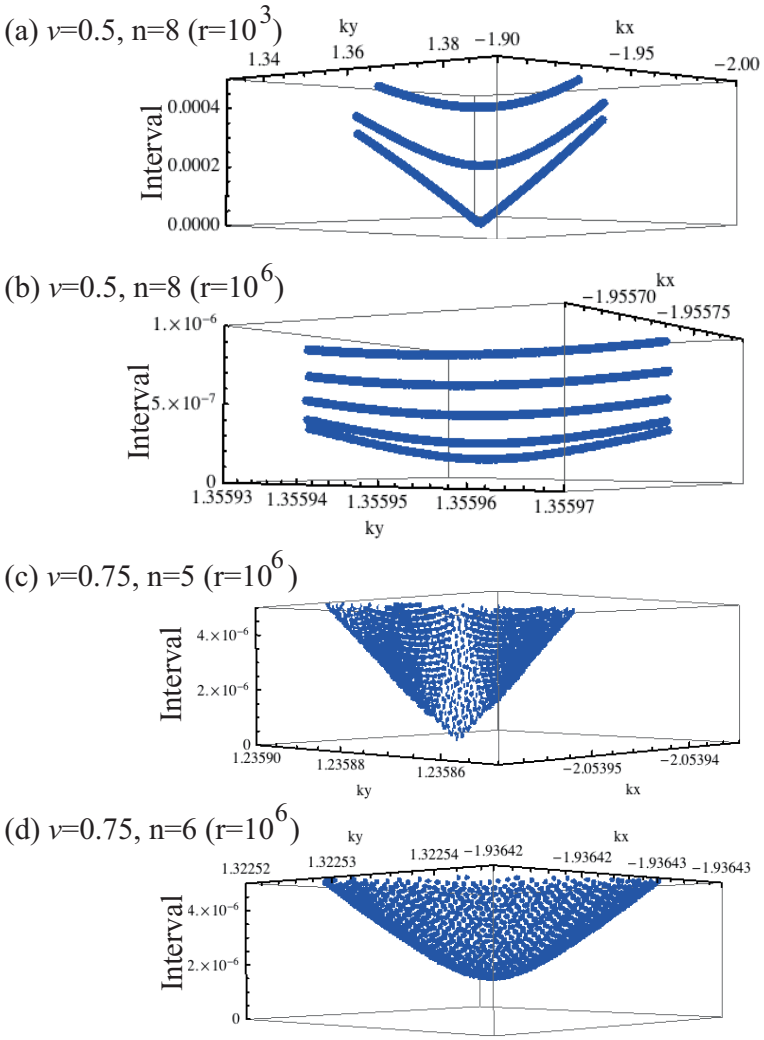

Figure 3.9: The energy intervals of neighboring energy eigenvalues around the contact "point" $n = 8$ ((a) for $r_1 = r_2 = 10^3$ and (b) for 10^6 with $v = 0.5$), $n = 5$ ((c) for $r_1 = r_2 = 10^6$ with $v = 0.75$), and $n = 6$ ((d) for $r_1 = r_2 = 10^6$ with $v = 0.75$). All the numerical results are obtained for the period $L = 25$. Note that the ranges of the wave numbers are all different.

3.2.3 Single-periodic potentials with different periods

We here show the generation of the Dirac-electron structures induced by single-periodic potentials of different periods. First we study the cases of short periods, namely $L = 2$, 3, and 4. When we add a potential of $L < 4$, Eq. (3.25) indicates that the energy of the first new Dirac-electron structure π/L is greater than the hopping element $t_1 = 1$. In these cases, the first Dirac-electron structures should have visibly large energy intervals. We next show other periods $L = 9$, 13, and 8. They have mostly similar properties to what we have discussed in the former subsections, but we still show them because the analysis here will be extended to the double-periodic cases in Chap. 4.

We use the same judgment rule as in Subsection 3.2.1. Figures 3.10, 3.11, and 3.12 represent the energy intervals of neighboring energy eigenvalues for $L = 2$, $L = 3$, and $L = 4$, respectively. For $L = 2$, we used the potential of a cosine function $v\cos((\vec{b}_1/2)\cdot\eta\vec{a}_1)$ because Eq. (2.42) gives always zero for $L = 2$. In Figs. 3.10 and 3.11, the energy intervals for $n = 1$ show visibly large energy gaps, but the intervals for $n = 0$ indicate a Dirac-electron structure. On the other hand, for $L = 4$, the energy intervals for $n = 0$ and $n = 1$ have the Dirac-electron structures but the interval for $n = 2$ show a visibly large gap. We thus find the new Dirac-electron structures only for $L \geq 4$. They also indicate that the energy gaps rapidly grow beyond the hopping element $t_1 = 1$.

Figures 3.13, 3.14, and 3.15 show the minimum energy intervals for $L = 9$, $L = 13$, and $L = 8$, respectively. In the figures, the data show the stepwise decrease similar to the one in Fig. 3.8. The energies of the Dirac electrons listed in Table 3.2 give the energy cutoffs. We will refer to the energies again in Chap. 4.

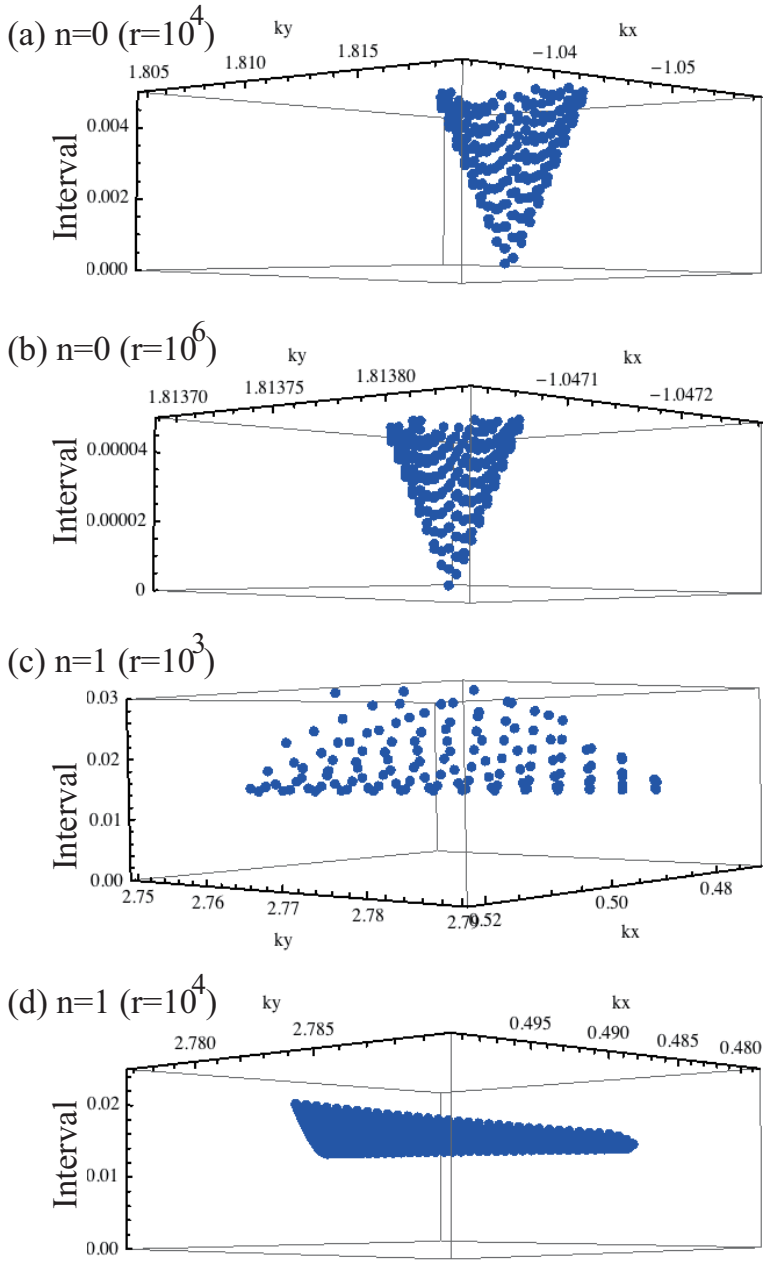

Figure 3.10: The energy intervals of neighboring energy eigenvalues around the contact "point" $n = 0$ ((a) for $r_1 = r_2 = 10^4$ and (b) for 10^6) and $n = 1$ ((c) for $r_1 = r_2 = 10^3$ and (d) for 10^4 with $L = 2$ and $v = 0.01$. Note that the ranges of the wave numbers are all different.

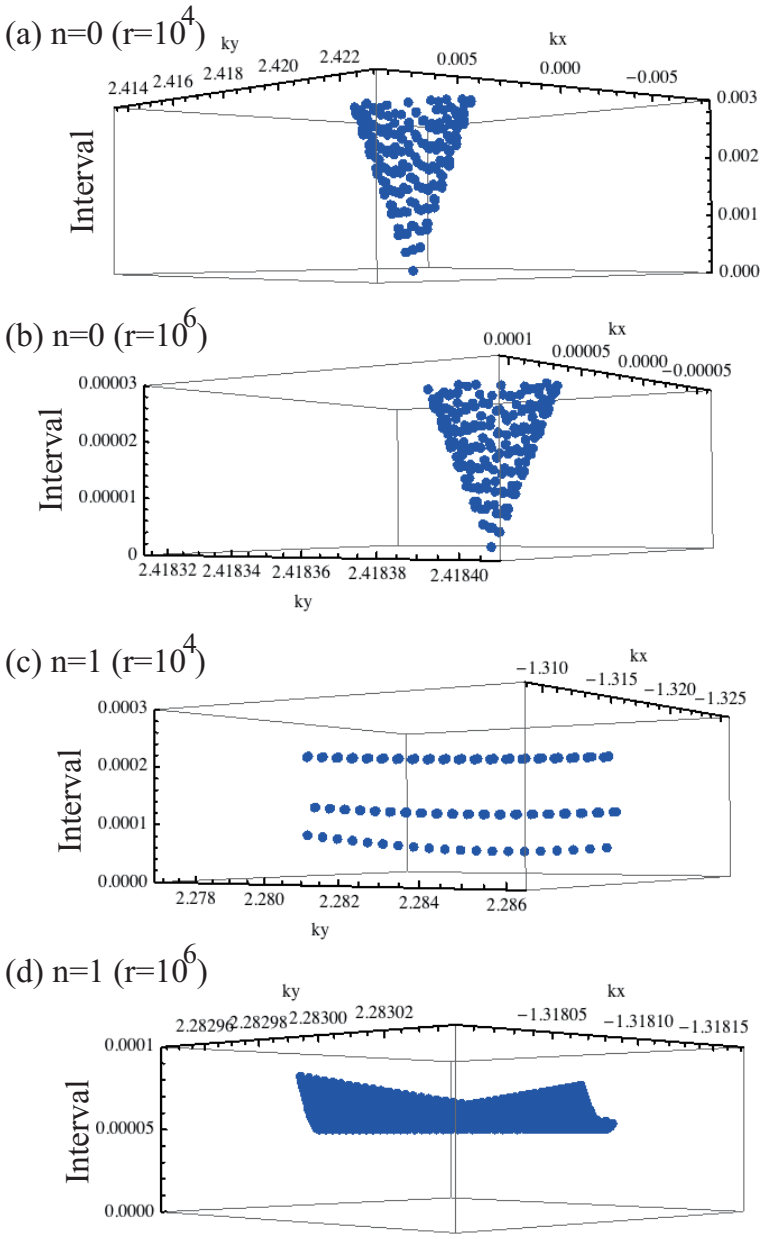

Figure 3.11: The energy intervals of neighboring energy eigenvalues around the contact "point" $n = 0$ ((a) for $r_1 = r_2 = 10^4$ and (b) for 10^6) and $n = 1$ ((c) for $r_1 = r_2 = 10^4$ and (d) for 10^6) with $L = 3$ and $v = 0.01$. Note that the ranges of the wave numbers are all different.

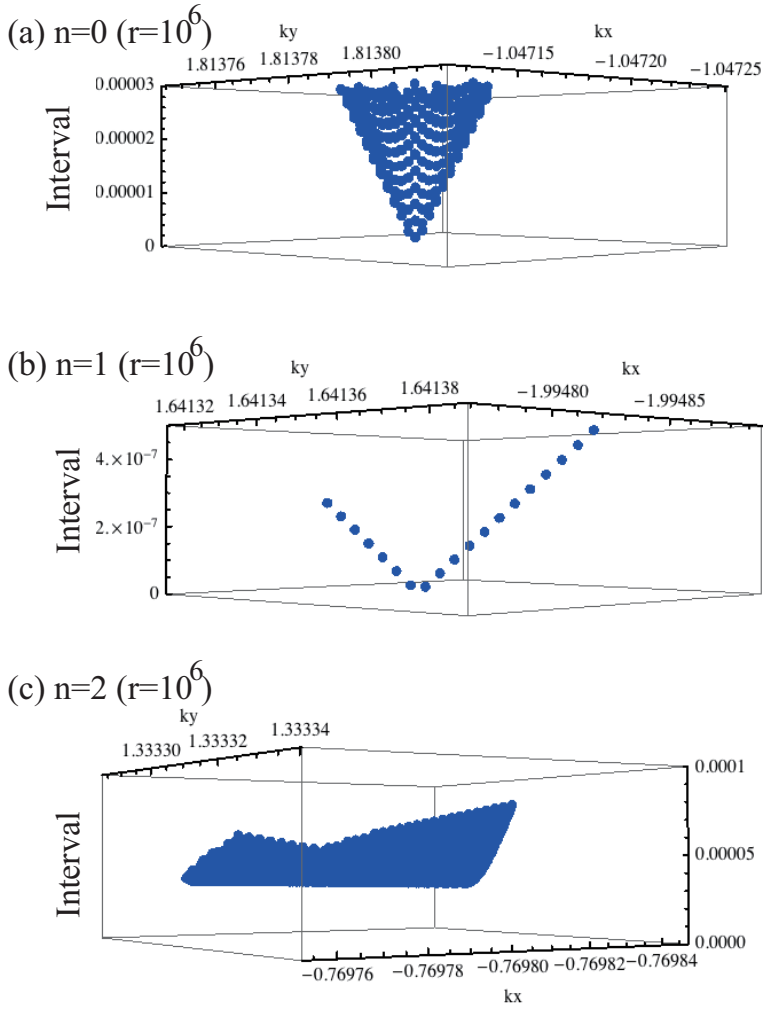

Figure 3.12: The energy intervals of neighboring energy eigenvalues around the contact "points" (a) $n = 0$, (b) $n = 1$, and (c) $n = 2$ for $r_1 = r_2 = 10^6$ with $L = 4$ and $v = 0.01$. Note that the ranges of the wave numbers are all different.

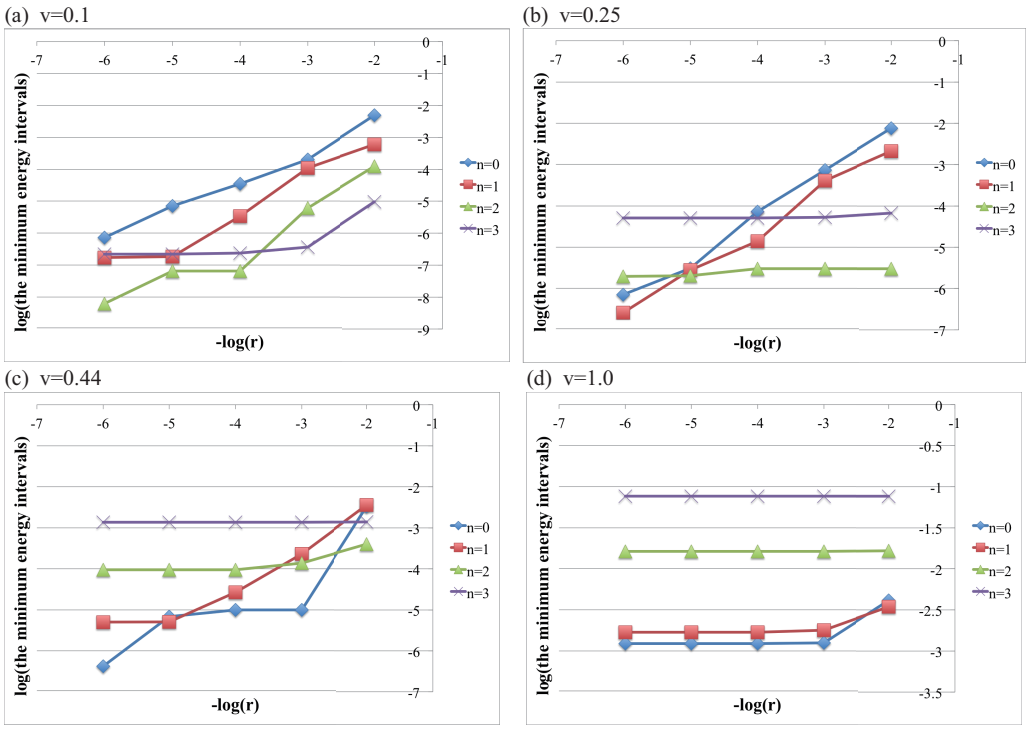

Figure 3.13: Logarithmic plots of the system-size dependence of the minimum energy intervals at the contact "points" for $L = 9$ with (a) $v = 0.1$, (b) $v = 0.25$, (c) $v = 0.44$, and (d) $v = 1.0$.

Table 3.2: The energies of the Dirac-electron structures for the superlattice potential $L = 8$, $L = 9$, and $L = 13$, compared with the theoretical prediction (3.25). We listed only the data above the Fermi energy $E = 0$.

indices	$L = 8$		$L = 9$		$L = 13$	
	energy	$(\pi/L) \times n$	energy	$(\pi/L) \times n$	energy	$(\pi/L) \times n$
$n = 0$	0.00	0.00	0.00	0.00	0.00	0.00
$n = +1$	0.38	0.393	0.34	0.349	0.24	0.242
$n = +2$	0.72	0.785	0.65	0.698	0.47	0.483
$n = +3$	1.00	1.18			0.68	0.725
$n = +4$					0.88	0.967

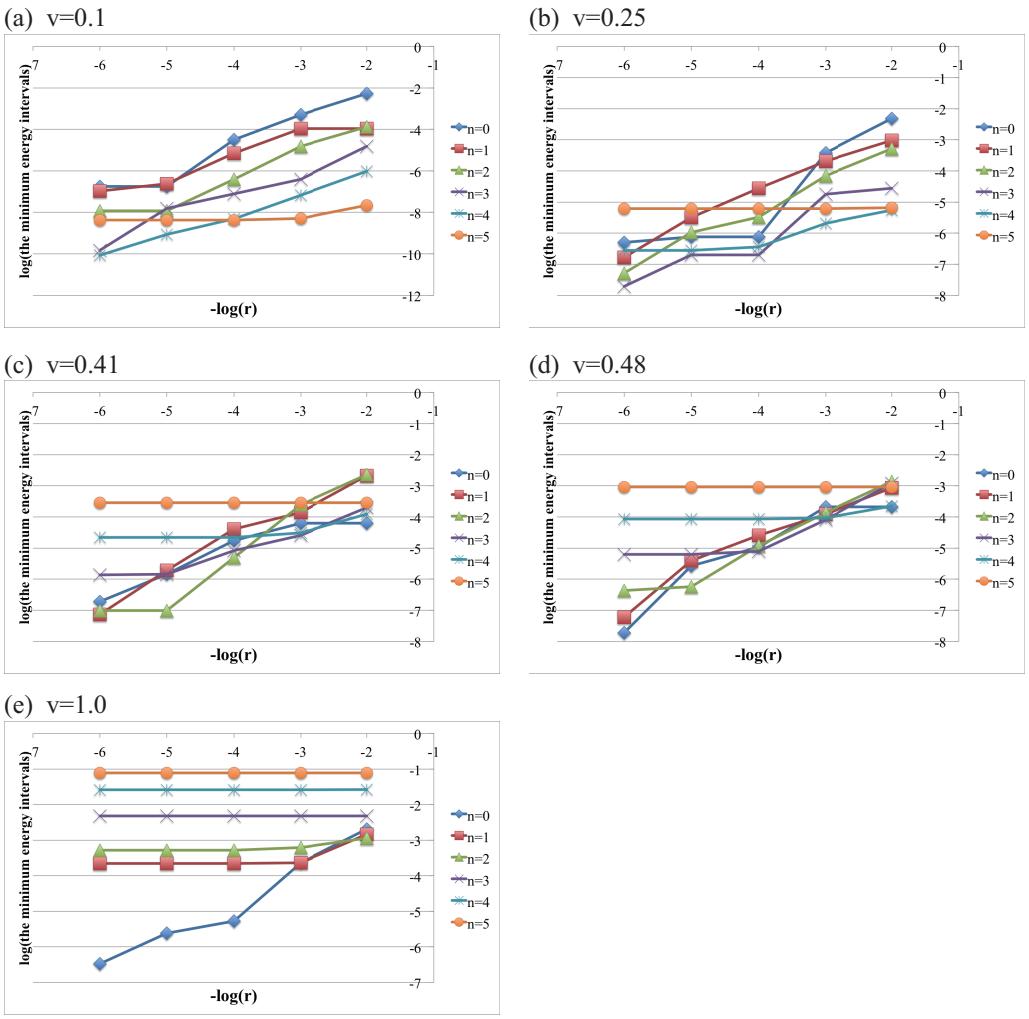

Figure 3.14: Logarithmic plots of the system-size dependence of the minimum energy intervals at the contact "points" for $L = 13$ with (a) $v = 0.1$, (b) $v = 0.25$, (c) $v = 0.41$, (d) $v = 0.48$, and (e) $v = 1.0$.

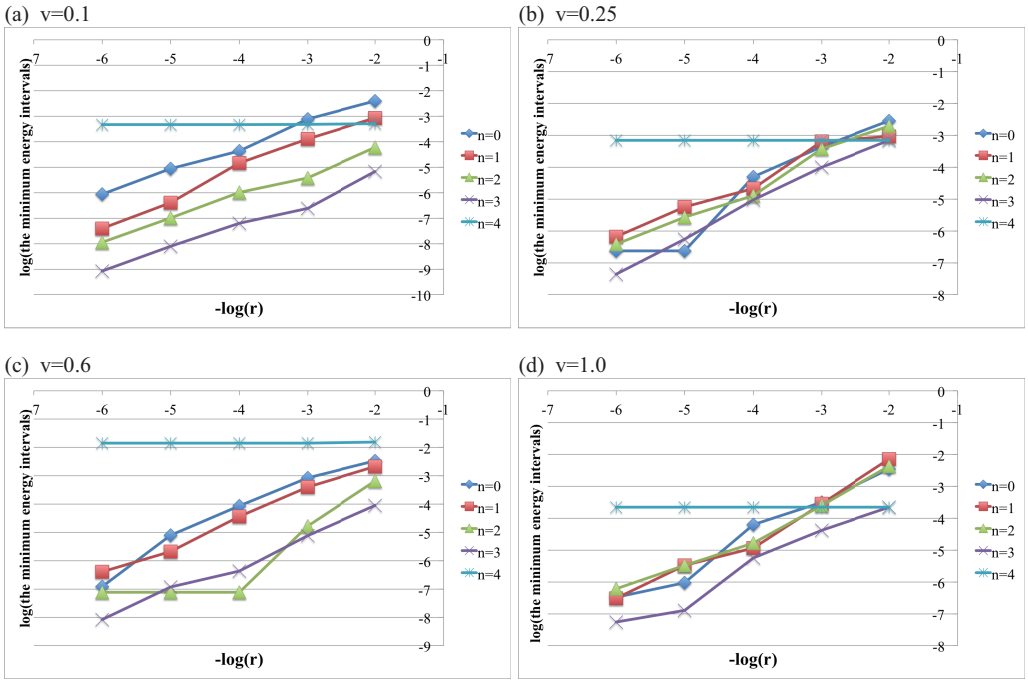

Figure 3.15: Logarithmic plots of the system-size dependence of the minimum energy intervals at the contact "points" for $L = 8$ with (a) $v = 0.1$, (b) $v = 0.25$, (c) $v = 0.6$, and (d) $v = 1.0$.

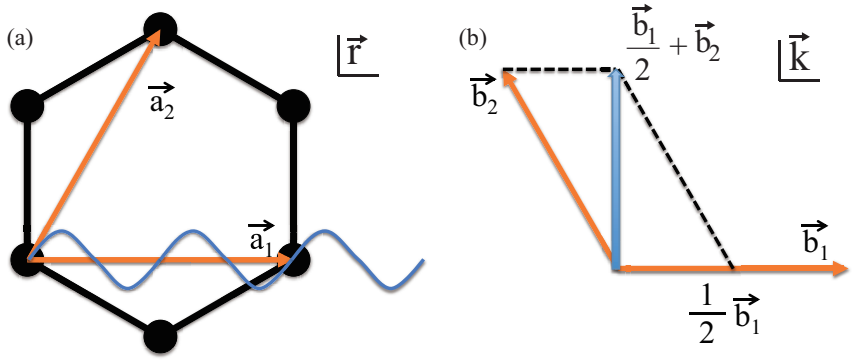

Figure 3.16: A relation between the direction of the one-dimensional superlattice potential and its effect in the reciprocal space. (a) We add the superlattice potential along the $\vec{a}_1$ direction of the hexagonal lattice. (b) The effect appears in the direction $(1/2)\vec{b}_1 + \vec{b}_2$, which is perpendicular to the reciprocal vector $\vec{b}_1$ corresponding to the lattice vector $\vec{a}_1$.

3.2.4 Anisotropy of the Dirac-electron structures

Equation (3.23) predicts that the one-dimensional superlattice potential changes the slope of the new Dirac cones in the direction perpendicular to the reciprocal vector of the external potential. Since we add the one-dimensional superlattice potential along the $\vec{a}_1$ direction on the hexagonal lattice system, the corresponding reciprocal vector is $\vec{b}_1$. The *perpendicular* direction in this case is given by $(1/2)\vec{b}_1 + \vec{b}_2$ (see Fig. 3.16). The effect of the one-dimensional potential $|f_m|^2$ in Eq. (3.23) therefore appears as the ratio of the slopes in the two directions $\vec{b}_1$ and $(1/2)\vec{b}_1 + \vec{b}_2$.

Figure 3.17 shows the ratios of the slopes for the Dirac-electro structures $n = 0, 1, \ldots, 8$ with $L = 25$ and $v = 0.25$, which we estimated by using two data points giving the minimum energy interval and its nearest neighbor for $r = 10^6$. As the index n becomes larger, the ratio of the slopes nearly exponentially decay. In other words, the new Dirac-electron structures far from the Fermi energy are strongly anisotropic. The anisotropy of the new Dirac cones widely changes depending on the amplitudes of the potentials; see Fig. 3.18. We find that the ratio generally approaches $t_1 = 1$ and the new Dirac-electron structures become isotropic as the potential gets stronger.

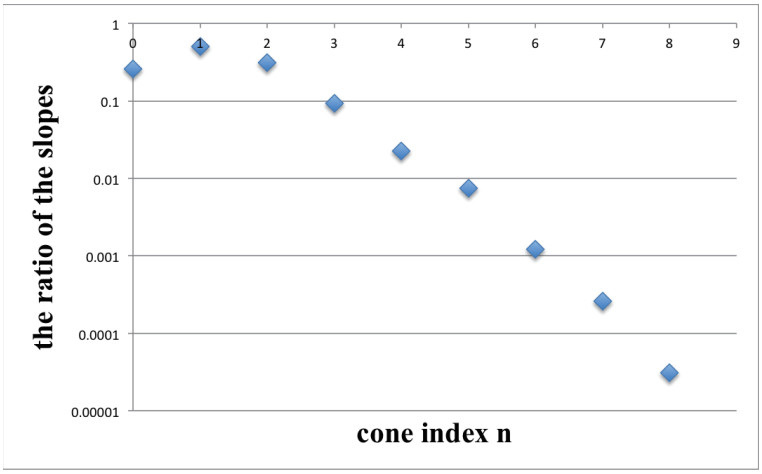

Figure 3.17: A semi-logarithmic plot of the ratio of the slopes in the directions $(1/2)\vec{b}_1+\vec{b}_2$ and $\vec{b}_1$ against the cone index n for $L = 25$, $r = 10^6$, and $v = 0.25$.

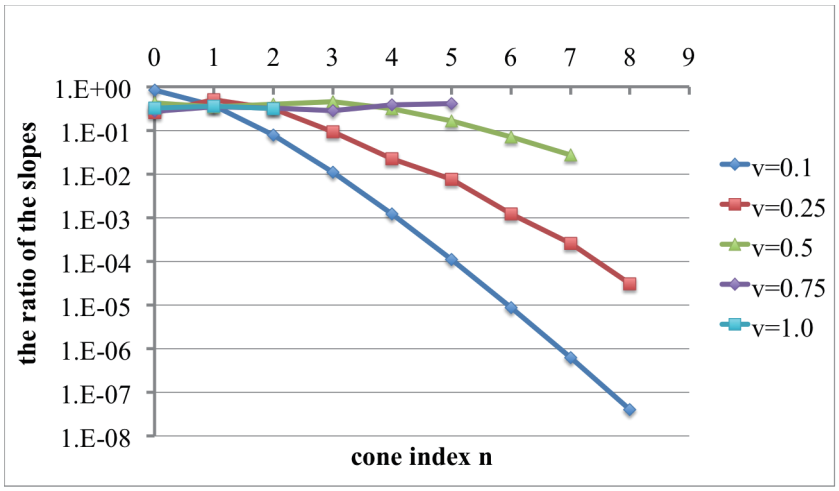

Figure 3.18: A semi-logarithmic plot of the relation between the cone indices n and the ratios of the slopes in the directions $(1/2)\vec{b}_1 + \vec{b}_2$ and $\vec{b}_1$ for $L = 25$ with $v = 0.1$, 0.25, 0.5, 0.75, and 1.0. The data series for $v = 0.25$ is the same as in Fig. 3.17. We omitted the data points whose energy intervals show a visibly large energy gap (e.g., $n = 8$ for $v = 0.5$; see Fig. 3.8).

We also investigate the anisotropy for $L = 9$, 13, 8; see Fig. 3.19 (a), (b), (c), respectively. All relations again show that the anisotropy of the Dirac-electron structure becomes weaker as the potential becomes larger. We, however, have not found a simple relation among the potential period and the anisotropy.

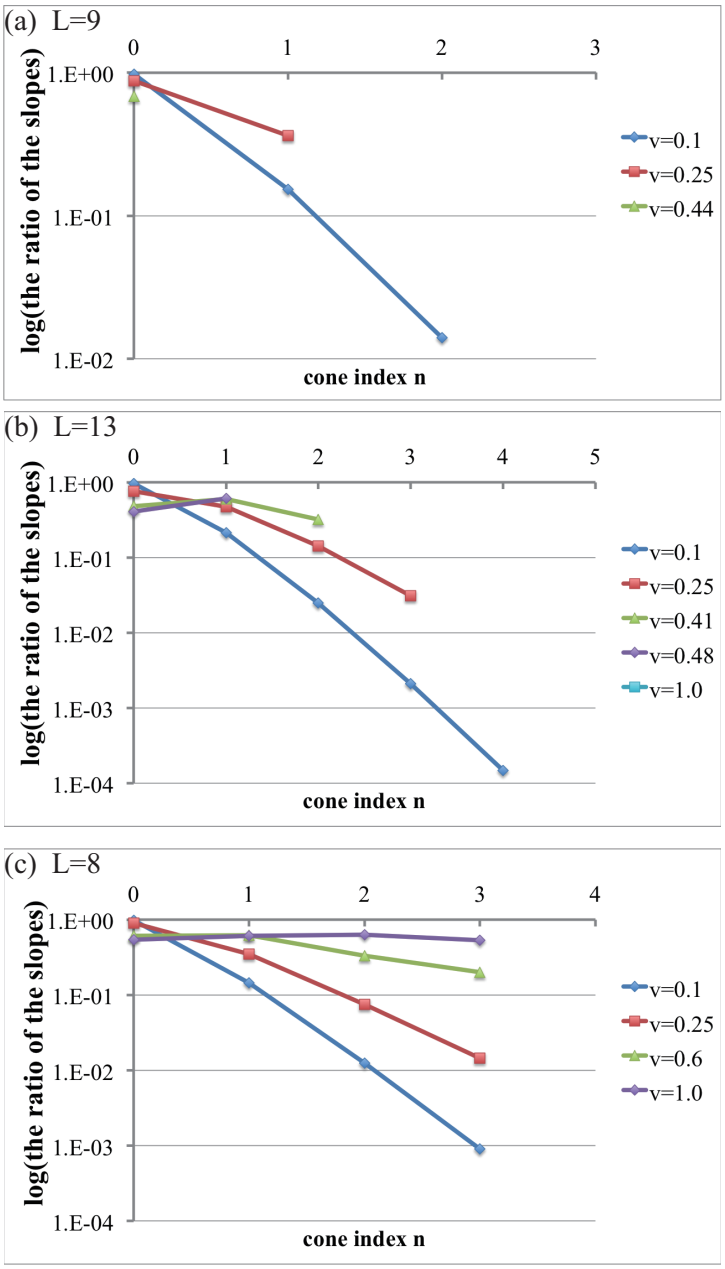

Figure 3.19: Semilogarithmic plots of the relation between the cone indices n and the ratio of the slopes in the directions $(1/2)\vec{b}_1 + \vec{b}_2$ and $\vec{b}_1$ for (a) $L = 9$, (b) $L = 13$, and (c) $L = 8$.

3.2.5 Positions of the Dirac-electron structures

The previous studies [55–58] have reported shifts and annihilation of the Dirac cones induced by external fields but a unified picture has not been clearly given. They reported that tuning the hopping elements can annihilate the two massless Dirac cones through shift and merging but preserve both the chiral symmetry and the equivalence of the sublattices. If we add an external potential through the Pauli matrix σ_z, the equivalence of the sublattices and the chiral symmetry of graphene immediately break. As a result, band gaps open at the K and K' points.

Applying a superlattice potential by using the identity matrix I, on the other hand, breaks the chiral symmetry but preserves the equivalence of the sublattices. In this case, Watanabe *et al.* [60] reported that the two Dirac cones stay gapless at the K and K' points but one of the energies increases and the other decreases as the amplitude increases. Their theoretical analysis showed that the Dirac cones at the K and K' points remain gapless against strong perturbations.

The previous studies [52, 53] predicted that the new Dirac cones appear at $(1/2)\vec{G} \times n$, where $\vec{G}$ is the reciprocal vector of the superlattice and n is an integer. However, when we apply the one-dimensional periodic superlattice potential to the hexagonal lattice system through the identity matrix I, the Dirac-electron structures do not always appear just at the predicted positions $(1/2)\vec{G} \times n$. Theoretical [52, 53] and experimental studies [26–31] indeed have not reported in detail the positions for the hexagonal lattice systems. Furthermore an experimental study for one-dimensional superlattice potential [40] indicated that the electronic structure may depend on the shapes and amplitudes of the potentials. We here report that the positions of the Dirac-electron structures for the hexagonal lattice system under the superlattice potentials move on a line in the k space. Our numerical results indicate a high likelihood that the Dirac-electron structures have invisibly small energy gaps by adding an infinitesimal superlattice potential.

In our thesis, we apply the one-dimensional potentials along the $\vec{a}_1$ direction. Therefore, the original Dirac points K and K' in the supercell Brillouin zone appear at

$$\vec{K} = K_1 \left(\frac{\vec{b}_1}{L} \right) + K_2 \vec{b}_2, \quad \vec{K}' = K_1' \left(\frac{\vec{b}_1}{L} \right) + K_2' \vec{b}_2, \tag{3.32}$$

where the coefficients K_1, K_2, K_1', and K_2' are all real numbers and their

absolute values are less than unity. In our setting, the coefficients can have the following three cases depending on the period L:

$$\{(K_1, K_2), (K_1', K_2')\} = \begin{cases} \left\{ \left(0, \frac{1}{3}\right), \left(0, \frac{2}{3}\right) \right\} \text{ for } L = 3 \times m, \\ \left\{ \left(\frac{1}{3}, \frac{1}{3}\right), \left(\frac{2}{3}, \frac{2}{3}\right) \right\} \text{ for } L = 3 \times m + 2, \\ \left\{ \left(\frac{2}{3}, \frac{1}{3}\right), \left(\frac{1}{3}, \frac{2}{3}\right) \right\} \text{ for } L = 3 \times m + 1, \end{cases} \tag{3.33}$$

where m is a positive integer (see Appendix B). Let us remember that two points $\vec{k}$ and $\vec{k} + \vec{G}$ represent the same position in the reciprocal space, and thus the Dirac points ideally appear only at $(\vec{K}, \vec{K}')$ and $(\vec{K} + (1/2)\vec{G}, \vec{K}' + (1/2)\vec{G})$ for even and odd indices, respectively.

We numerically found that the minimum energy intervals move linearly in the direction perpendicular to $\vec{b}_1$ (see Figs. 3.20, 3.21, and 3.22). It is clear that the data points for even indices pass through the K and K' points while the ones for odd indices pass through the points $\vec{K} + (1/2)\vec{G}$ and $\vec{K}' + (1/2)\vec{G}$. As we change the amplitude of the potential, the data points centered around the K and K' points move in the directions opposite to each other (see Figs. 3.20 and 3.21). Figure 3.23 shows the distances between the positions of the Dirac-electron structures and the K point or $\vec{K} + (1/2)\vec{G}$. For $n = 0$, as we decrease the amplitude, the position of the Dirac-electron structure converges to the K point (see Fig. 3.23 (a)). For $n \geq 1$, however, the distances between the positions and the K point or $\vec{K} + (1/2)\vec{G}$ do not converge to zero (see Fig. 3.23 (b), (c), and (d)). In the tight-binding model with a weak amplitude, the positions of the Dirac-electron structures for $n \neq 0$ appear away from the predicted positions. We can understand why the deviation of the positions have not been reported in the previous studies [52,53] as follows. Figure 3.24 shows a relation between the energies of the Dirac-electron structures and the absolute values of the distances. The distances lineally grow as the energies draw away from the Fermi energy. When we apply a long potential, the first Dirac-electron structure appear very close to the Fermi energy. Thus the distance for the first structure may be invisibly small. In the previous studies [52, 53], they actually applied a weak potential ($0.1t_1$) with a long period (40 times larger than the lattice constant), and focused only on the first new Dirac cone. This may be the

reason why the previous studies have not numerically found the deviation of the positions.

Previous studies [55–58] reported that the two Dirac cones merge at a point before becoming a gapful structure. Our numerical results indicate a high likelihood that the Dirac-electron structures without merging are in fact not gapless cones.

In our setting, the data points on the lines $(1/2)\vec{b}_1 + \vec{b}_2$ passing through the K and K' points, in general, do not meet in the supercell Brillouin zone. We here study the case $L = 3 \times m + 1$ with even indices as an example. In order for the two series of the data points to meet, they should satisfy the following relation:

$$\vec{K} + \alpha \left(\frac{1}{2}\vec{b_1} + \vec{b_2} \right) = \vec{K}' + \beta \left(\frac{1}{2}\vec{b_1} + \vec{b_2} \right), \tag{3.34}$$

where α and β are real numbers. The coefficient β is thus represented by α:

$$\begin{aligned} \beta &= \alpha - \frac{1}{3}\frac{2}{L} \quad \text{for} \quad \frac{\vec{b}_1}{L} \quad \text{direction} \\ \beta &= \alpha - \frac{1}{3} \quad \text{for} \quad \vec{b}_2 \quad \text{direction.} \end{aligned} \tag{3.35}$$

The two relations only hold for $L = 2$. In the case of the period $L \neq 2$, the two Dirac-electron structures cannot meet in the supercell Brillouin zone. In this thesis, our numerical results have shown that, as we increase the amplitude, the energy intervals of the two structures grow to visible values without merging. However, the results for $L = 2$ shows a completely different trend.

For $L = 2$, the two gapless Dirac cones indeed meet at the midpoint of the K and K' points (see Appendix C). Figures 3.25 and 3.26 show the merging of the two Dirac cones for $L = 2$. In both figures, we focus on the area around the origin of the k space. As the amplitude increases to the threshold $v = \sqrt{3}$, the two Dirac cones approach each other (see Fig. 3.25). In these cases, all the energy intervals are zero. We can find the two Dirac cones for $v = 1.73$ (see Fig. 3.26 (a)) but we cannot find them for $v = 1.74$, which is greater then the threshold (see Fig. 3.26 (b)).

The previous works and our results indicate that, when the two Dirac-electron structures merge each other, they have a strong possibility of the

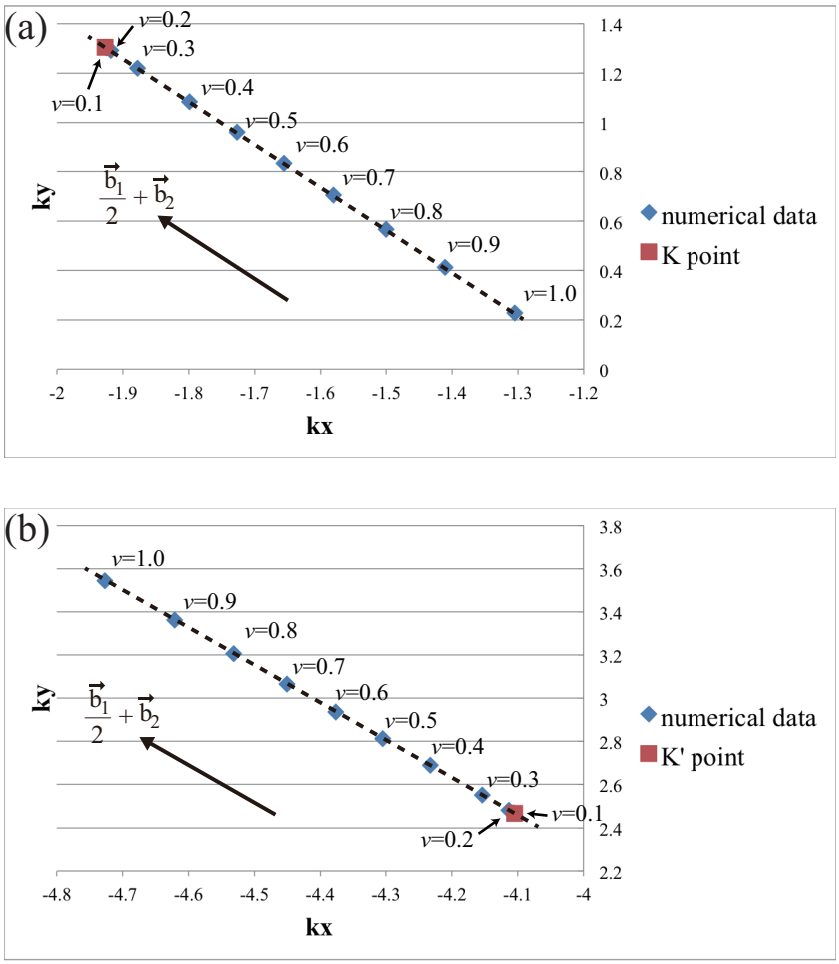

Figure 3.20: Positions of the minimum energy intervals $n = 0$ for $L = 25$. The numerical data around (a) the K and (b) K' points are plotted. The broken line is parallel to the vector $(1/2)\vec{b}_1 + \vec{b}_2$.

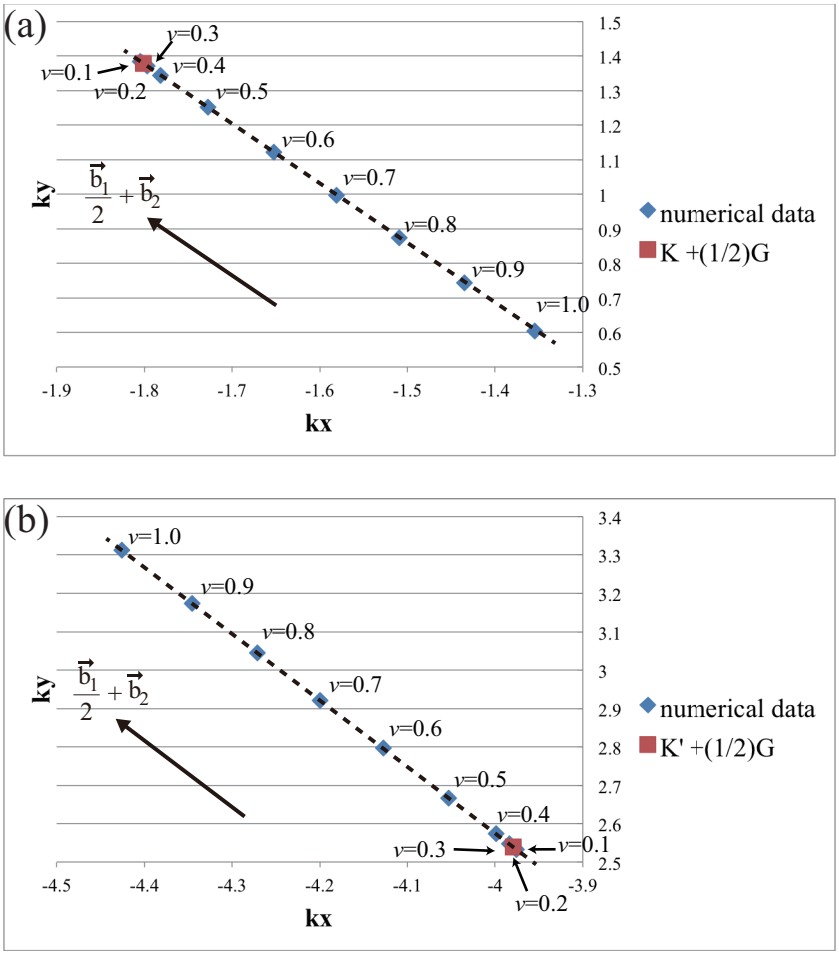

Figure 3.21: Positions of the minimum energy intervals $n = 1$ for $L = 25$. The numerical data around (a) $\vec{K} + (1/2)\vec{G}$ and (b) $\vec{K'} + (1/2)\vec{G}$ points are plotted. The broken line is parallel to the vector $(1/2)\vec{b}_1 + \vec{b}_2$.

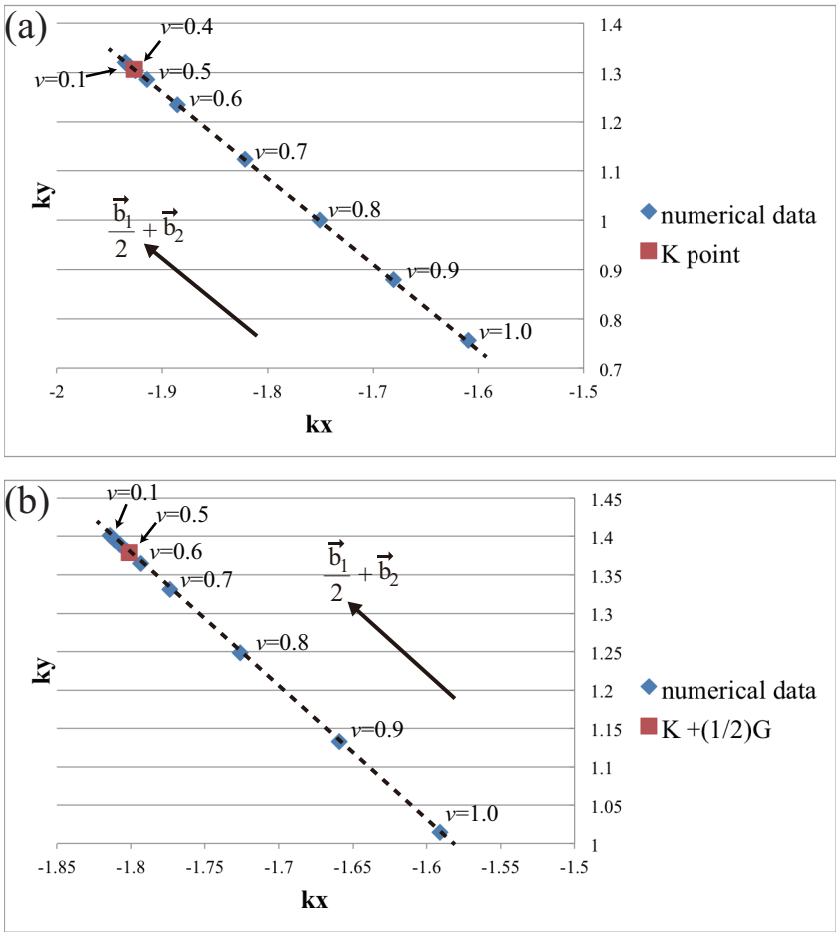

Figure 3.22: Positions of the minimum energy intervals (a) $n = 2$ and (b) $n = 3$ for $L = 25$ around the K point. The broken line is parallel to the vector $(1/2)\vec{b}_1 + \vec{b}_2$.

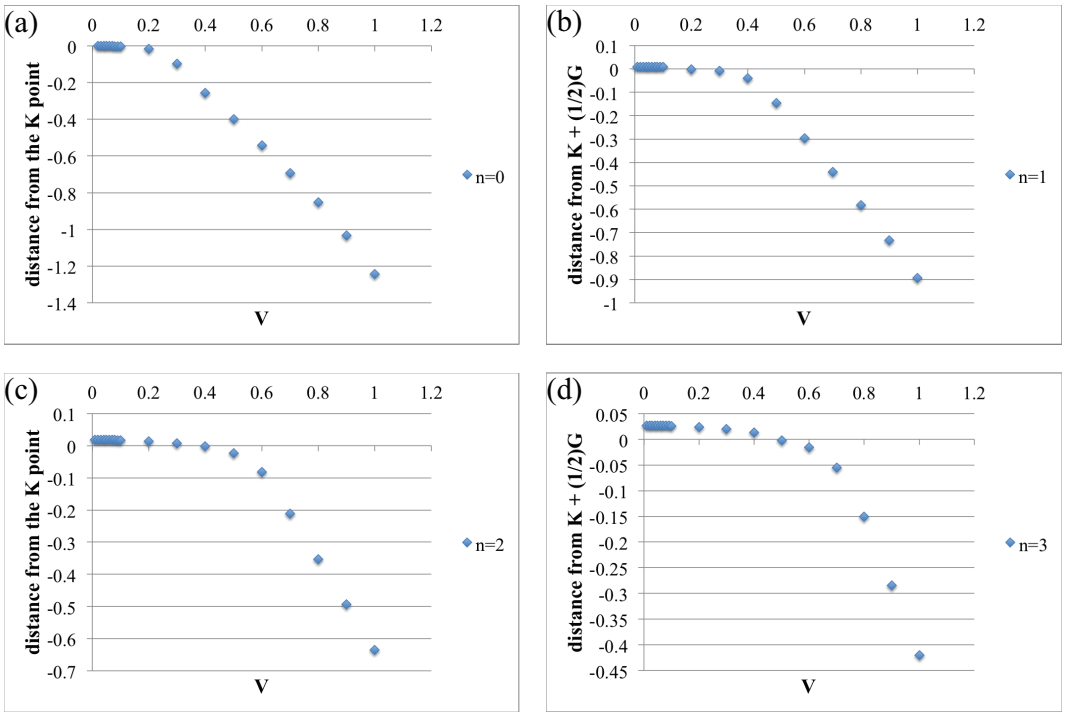

Figure 3.23: Distances between the positions of the Dirac-electron structures and ((a) and (c)) the K point or ((b) and (d)) $\vec{K} + (1/2)\vec{G}$. We set the positive values along the vector $(1/2)\vec{b}_1 + \vec{b}_2$ in Fig. 3.20, 3.21, and 3.22.

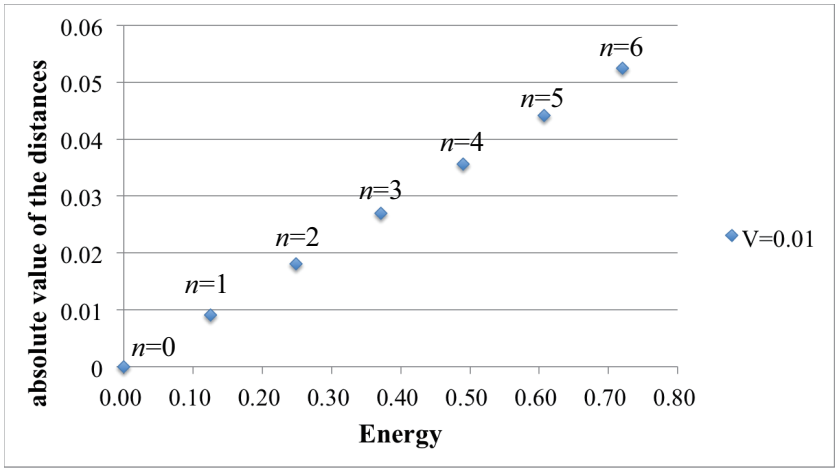

Figure 3.24: A relation between the energies of the Dirac-electron structures and the absolute values of the distances.

existence of zero gaps before the merge. In contrast, the structures without merging are more likely to have invisibly small energy gaps when the potential is very weak.

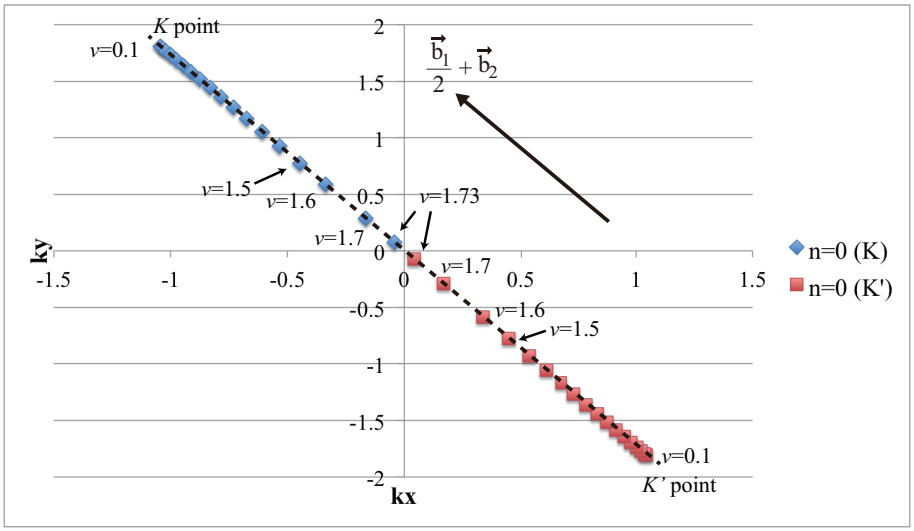

Figure 3.25: The positions of the Dirac points $n = 0$ for $L = 2$. The broken line is parallel to the vector $(1/2)\vec{b}_1 + \vec{b}_2$.

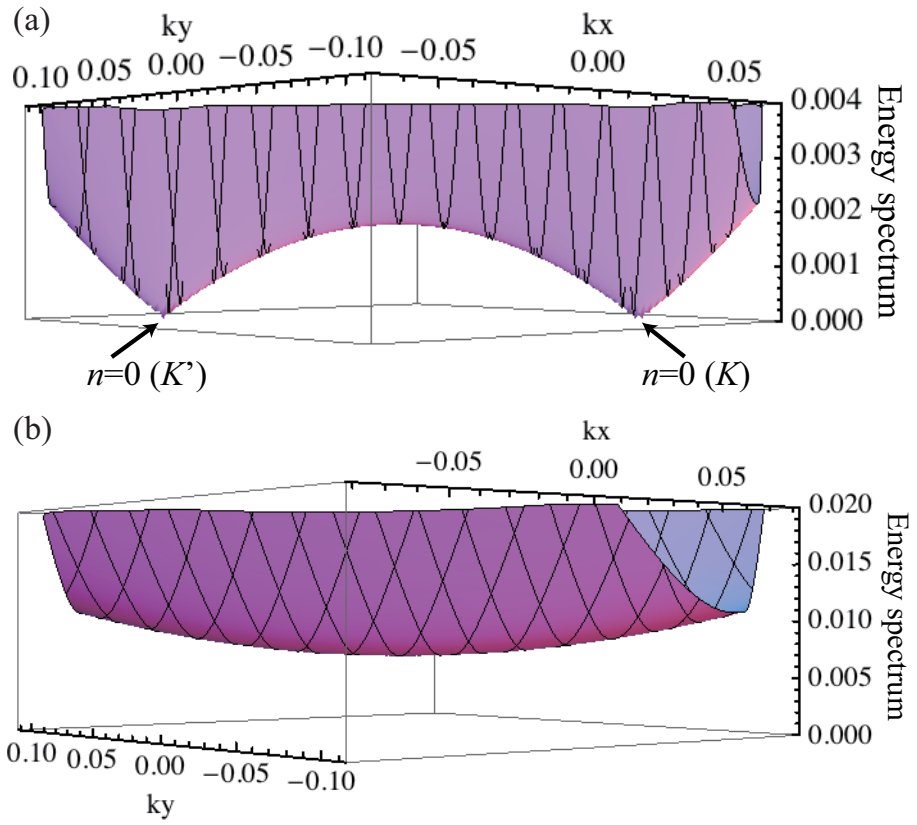

Figure 3.26: The energy spectrum for $L = 2$ with (a) $v = 1.73$ and (b) $v = 1.74$. The arrows indicate the Dirac cones $n = 0$ around the K and K' points.

Chapter 4

Double-periodic potentials

We show a generation rule of the Dirac-electron structures under the double-periodic potentials by analyzing the Dirac Hamiltonian with the energy cutoff ΔE as a model parameter. We first consider that in our model gapless Dirac cones induced by the single-periodic potential consecutively appear only below the energy cutoff. Our theoretical analysis shows that the double-periodic potential generates Dirac cones *sporadically*. We next study the appearance of the Dirac-electron structures in the tight-binding model under the double-periodic potential. As is the case with the single-periodic potentials, our numerical results cannot tell whether the Dirac-electron structures are truly gapless or not. In spite of it, the appearance of the Dirac-electron structures with invisibly small gaps is consistent with the sporadic generation of the Dirac cones derived from our model. It indicates that our model works well for realizing the generation of the Dirac-electron structures in the double-periodic cases.

4.1 Generation of the new Dirac cones under the double-periodic potentials

We consider the double-periodic potentials in order to study the quasiperiodic cases as an ultimate goal. A double-periodic function is defined as follows. For simplicity again, let us consider the functions V_1 and V_2 which are periodic

along the x axis, namely the $\vec{a}_1$ direction:

$$\begin{aligned} V_1(x + L_1) &= V_1(x), \\ V_2(x + L_2) &= V_2(x), \end{aligned} \tag{4.1}$$

where the integers L_1 and L_2 are the periods of the two functions and *coprime* integers. We now apply the sum $V = V_1 + V_2$ as a double-periodic potential.

The potential is obviously a periodic function with the period $L = L_1 \times L_2$. One would therefore expect to understand the generation of new cones in terms of the single-periodic superlattice potential [53] (Chap. 3) and would predict that the Dirac cones appear in the energy spectrum at

$$\hbar v_0 \frac{\pi}{L} n_{\mathrm{d}}, \quad n_{\mathrm{d}} = 0, \pm 1, \pm 2, \ldots, \pm N_{\mathrm{d}} \tag{4.2}$$

consecutively up to the limit $N_{\mathrm{d}} \simeq \lfloor L\Delta E/\pi \rfloor$.

We will show, however, that the appearance of the new Dirac cones is sporadic in some cases of ΔE. The argument is based on the Dirac Hamiltonian in the single-periodic case in Section 3.1. We define α_1 and α_2 as the integral of the superlattice potentials:

$$\alpha_i(x) = \frac{2}{\hbar v_0} \int_0^x V_i(x')dx', \tag{4.3}$$

where $i = 1, 2$. The integral of the whole potential is given by

$$\begin{aligned} \alpha(x) &= \frac{2}{\hbar v_0} \int_0^x V(x')dx' \\ &= \frac{2}{\hbar v_0} \int_0^x \left(V_1(x') + V_2(x')\right) dx' \\ &= \alpha_1(x) + \alpha_2(x). \end{aligned} \tag{4.4}$$

We rewrite the Dirac Hamiltonian with the double-periodic potential (3.1) by using a unitary matrix U_1

$$U_1 = \frac{1}{\sqrt{2}} \begin{pmatrix} e^{-i\alpha/2} & -e^{+i\alpha/2} \\ e^{-i\alpha/2} & e^{+i\alpha/2} \end{pmatrix}, \tag{4.5}$$

which is similar to Eq. (3.8) but we note that α is the sum of the integrals of the two external potentials. We obtain the Hamiltonian h' with a similar

transformation using the unitary matrix U_1:

$$\begin{aligned} h' = U_1^{\dagger} h [V_1 + V_2] U_1 &= \hbar v_0 \begin{pmatrix} -i\frac{\partial}{\partial x} & -e^{+i\alpha(x)}\frac{\partial}{\partial y} \\ e^{-i\alpha(x)}\frac{\partial}{\partial y} & i\frac{\partial}{\partial x} \end{pmatrix} \\ &= \hbar v_0 \begin{pmatrix} -i\frac{\partial}{\partial x} & -e^{+i\alpha_1(x)}e^{+i\alpha_2(x)}\frac{\partial}{\partial y} \\ e^{-i\alpha_1(x)}e^{-i\alpha_2(x)}\frac{\partial}{\partial y} & i\frac{\partial}{\partial x} \end{pmatrix}. \end{aligned} \tag{4.6}$$

We again introduce the basis set of plane-wave spinors in order to calculate the eigenstates and the eigenenergies. The different point from the single-periodic case is to use two reciprocal vectors to represent the wave vectors in the double-periodic case. We can rewrite the reciprocal vector $\vec{G} = \left(2\pi\vec{k}_x\right)/L$ in the double-periodic case as the summation of the reciprocal vectors

$$\vec{G}_1 = \frac{2\pi}{L_1}\vec{k}_x, \quad \vec{G}_2 = \frac{2\pi}{L_2}\vec{k}_x \tag{4.7}$$

of the external potentials because the period is $L = L_1 \times L_2$:

$$n\vec{G} = n_1\vec{G}_1 + n_2\vec{G}_2, \tag{4.8}$$

where n, n_1, and n_2 are integers. We here are interested in the generation of the new Dirac cones close to the wave vector $\vec{k} = \left(\vec{G}_1 n_1\right)/2 + \left(\vec{G}_2 n_2\right)/2 + \vec{\kappa}$. We use the following two states as bases to reduce the matrix h' into a matrix:

$$\vec{u}_1 = \begin{pmatrix} 1 \\ 0 \end{pmatrix}' e^{i\left(\frac{\vec{G}_1}{2}n_1 + \frac{\vec{G}_2}{2}n_2 + \vec{\kappa}\right)\cdot\vec{r}} \tag{4.9}$$

and

$$\vec{u}_2 = \begin{pmatrix} 0 \\ 1 \end{pmatrix}' e^{-i\left(\frac{\vec{G}_1}{2}n_1 + \frac{\vec{G}_2}{2}n_2 - \vec{\kappa}\right)\cdot\vec{r}}, \tag{4.10}$$

where $\vec{\kappa} = (\kappa_x, \kappa_y)$ is the wave vector which is defined as $|\vec{\kappa}| \ll (2\pi)/L$. We also use the prime to indicate that the spinor bases are defined for the matrix h'.

By operating the Hamiltonian h' on the states $\vec{u}_1$, we obtain the following relation:

$$\begin{aligned} h'\vec{B}_1 &= \hbar v_0 \begin{pmatrix} -i\frac{\partial}{\partial x} \\ e^{-i\alpha_1}e^{-\alpha_2}\frac{\partial}{\partial y} \end{pmatrix}' e^{i\left(\frac{\vec{G}_1}{2}n_1 + \frac{\vec{G}_2}{2}n_2 + \vec{\kappa}\right)\cdot\vec{r}} \\ &= \hbar v_0 \begin{pmatrix} (-i)i\left(\frac{G_1}{2}n_1 + \frac{G_2}{2}n_2 + \kappa_x\right) \\ \left(\sum_{l_1} f_{1,l_1} e^{-il_1 G_1 x}\right)\left(\sum_{l_2} f_{2,l_2} e^{-il_2 G_2 x}\right)(i\kappa_y) \end{pmatrix}' e^{i\left(\frac{\vec{G}_1}{2}n_1 + \frac{\vec{G}_2}{2}n_2 + \vec{\kappa}\right)\cdot\vec{r}}, \end{aligned} \tag{4.11}$$

where we introduced the following expansion:

$$e^{i\alpha_1(x)} = \sum_{l_1=-\infty}^{+\infty} f_{1,l_1}[V_1] e^{il_1 G_1 x} \tag{4.12}$$

and

$$e^{i\alpha_2(x)} = \sum_{l_2=-\infty}^{+\infty} f_{2,l_2}[V_2] e^{il_2 G_2 x} \tag{4.13}$$

with $|\vec{G}_i| = 2\pi/L_i$ and real coefficients f_{i,l_i} for $i = 1, 2$. We only consider the term with $l_1 = n_1$ and $l_2 = n_2$ in the sums to obtain the states with the wave vector $\vec{k} = -\left(\vec{G}_1 n_1 + \vec{G}_2 n_2\right)/2 + \vec{\kappa}$ because we are interested in a matrix constructed on the bases $\vec{b}_1$ and $\vec{b}_2$:

$$\begin{aligned} & f_{1,n_1} e^{-in_1 G_1 x} f_{2,n_2} e^{-in_2 G_2 x} (i\kappa_y) \, e^{i\left(\frac{\vec{G}_1}{2} n_1 + \frac{\vec{G}_2}{2} n_2 + \vec{\kappa}\right)\cdot\vec{r}} \\ & = f_{1,n_1} f_{2,n_2} (i\kappa_y) \, e^{-i\left(\frac{\vec{G}_1}{2} n_1 + \frac{\vec{G}_2}{2} n_2 - \vec{\kappa}\right)\cdot\vec{r}}. \end{aligned} \tag{4.14}$$

Therefore we approximate $h'\vec{u}_1$ on the bases $\vec{u}_1$ and $\vec{u}_2$ for the states around $(\vec{G}_1 n_1)/2 + (\vec{G}_2 n_2)/2$:

$$\begin{aligned} & \hbar v_0 \left(\frac{G_1}{2} n_1 + \frac{G_2}{2} n_2 + \kappa_x\right) \begin{pmatrix} 1 \\ 0 \end{pmatrix}' e^{i\left(\frac{G_1}{2} n_1 + \frac{G_2}{2} n_2 + \vec{\kappa}\right)\cdot\vec{r}} \\ & + \hbar v_0 f_{1,n_1} f_{2,n_2} (i\kappa_y) \begin{pmatrix} 0 \\ 1 \end{pmatrix}' e^{-i\left(\frac{\vec{G}_1}{2} n_1 + \frac{\vec{G}_2}{2} n_2 - \kappa\right)\cdot\vec{r}} \\ & = \hbar v_0 \left(\frac{G_1}{2} n_1 + \frac{G_2}{2} n_2 + \kappa_x\right) \vec{u}_1 + \hbar v_0 \left(i f_{1,n_1} f_{2,n_2} \kappa_y\right) \vec{u}_2. \end{aligned} \tag{4.15}$$

We similarly rewrite $h'\vec{u}_2$ around the wave vector $(\vec{G}_1 n_1)/2 + (\vec{G}_2 n_2)/2$. We operate the matrix h' on the basis $\vec{u}_2$:

$$h'\vec{u}_2 = \hbar v_0 \begin{pmatrix} \left(\sum_{l_1} f_{1,l_1} e^{-il_1 G_1 x}\right) \left(\sum_{l_2} f_{2,l_2} e^{-il_2 G_2 x}\right) (-i\kappa_y) \\ \frac{G_1}{2} n_1 + \frac{G_2}{2} n_2 - \kappa_x \end{pmatrix}' e^{-i\left(\frac{\vec{G}_1}{2} n_1 + \frac{\vec{G}_2}{2} n_2 - \vec{\kappa}\right)\cdot\vec{r}}. \tag{4.16}$$

We also obtain an approximation of $h'\vec{u}_2$ with the conditions $l_1 = n_1$ and $l_2 = n_2$:

$$\hbar v_0 \left(-i f_{1,n_1} f_{2,n_2} \kappa_y\right) \vec{u}_1 + \hbar v_0 \left(\frac{G_1}{2} n_1 + \frac{G_2}{2} n_2 - \kappa_x\right) \vec{u}_2. \tag{4.17}$$

We thus obtain a matrix M as an approximation of the Hamiltonian h' under the condition that the wave vector $\vec{k}$ is very close to $(G_1 n_1)/2 + (G_2 n_2)/2$:

$$\begin{aligned} M &= \hbar v_0 \begin{pmatrix} \frac{G_1}{2} n_1 + \frac{G_2}{2} n_2 + \kappa_x & -i\kappa_y f_{1,n_1} f_{2,n_2} \\ i\kappa_y f_{1,n_1} f_{2,n_2} & \frac{G_1}{2} n_1 + \frac{G_2}{2} n_2 - \kappa_x \end{pmatrix} \\ &= \hbar v_0 \left(\kappa_x \sigma_z + f_{1,n_1} f_{2,n_2} \kappa_y \sigma_y \right) + \hbar v_0 \left(\frac{G_1}{2} n_1 + \frac{G_2}{2} n_2 \right) I. \end{aligned} \tag{4.18}$$

We transform (4.18) by using the following unitary matrix U_2 in order to show that the approximated energy spectrum is linear around $\left(\vec{G}_1 n_1\right)/2 + \left(\vec{G}_2 n_2\right)/2$:

$$U_2 = \frac{1}{\sqrt{2}} \begin{pmatrix} 1 & 1 \\ -1 & 1 \end{pmatrix} = \frac{1}{\sqrt{2}} \left(I + i\sigma_y \right). \tag{4.19}$$

We obtain the matrix M' by the unitary transformation:

$$\begin{aligned} M' &= U_2^\dagger M U_2 \\ &= \hbar v_0 \left(\kappa_x \sigma_x + f_{1,n_1} f_{2,n_2} \kappa_y \sigma_y \right) + \hbar v_0 \left(\frac{G_1}{2} n_1 + \frac{G_2}{2} n_2 \right) I, \end{aligned} \tag{4.20}$$

where we used the relations Eqs. (3.20), (3.21), and (3.22). The matrix M is also similar to the Dirac Hamiltonian (2.20). The eigenenergy is

$$E_s\left(\vec{\kappa}\right) = s\hbar v_0 \sqrt{\kappa_x^2 + \left| f_{1,n_1} f_{2,n_2} \right|^2 \kappa_y^2} + \frac{h v_0}{2} \left(G_1 n_1 + G_2 n_2 \right), \tag{4.21}$$

where $s = \pm 1$ represents the two bands. The effect of the potentials f_{1,m_1} and f_{2,m_2} yields the gradient of the energy spectrum in the κ_y direction. This is again because we add the external potential with the periodicity in the x direction.

The second term in (4.21) must be consistent with Eq. (4.2) when we study the same double-periodic system:

$$\hbar v_0 \frac{\pi}{L} n_{\mathrm{d}} = \hbar v_0 \left(\frac{\pi}{L_1} n_1 + \frac{\pi}{L_2} n_2 \right). \tag{4.22}$$

Let us remember that the period of the double-periodic function is given by $L = L_1 \times L_2$. We thus obtain the Diophantine equation:

$$n_{\mathrm{d}} = L_2 n_1 + L_1 n_2. \tag{4.23}$$

The point is the following. If the indices n_1 and n_2 took all integer values as is for the Dirac Hamiltonian (3.1), the Diophantine equation (4.23) could produce any integers for $n_{\rm d}$. In our model, however, the generation of the new Dirac cones is restricted by the energy cutoffs ΔE_i as in $n_i = \pm 1, \pm 2, \ldots, \pm N_i$, where $N_i \simeq \lfloor L_i \Delta E_i / \pi \rfloor$. Though each of the indices n_1 and n_2 is consecutive up to its respective limit N_1 and N_2, the index of the new Dirac cones $n_{\rm d}$ in the Diophantine equation (4.23) is *not* always consecutive because of the finite energy cutoffs ΔE_i.

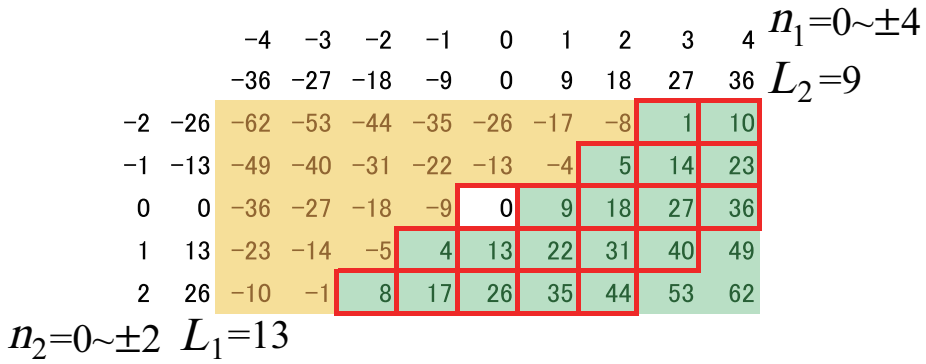

		−4	−3	−2	−1	0	1	2	3	4
		−36	−27	−18	−9	0	9	18	27	36
−2	−26	−62	−53	−44	−35	−26	−17	−8	1	10
−1	−13	−49	−40	−31	−22	−13	−4	5	14	23
0	0	−36	−27	−18	−9	0	9	18	27	36
1	13	−23	−14	−5	4	13	22	31	40	49
2	26	−10	−1	8	17	26	35	44	53	62

Figure 4.1: The table of the combination of the indices $n_1 = 0, \pm1, \pm2, \pm3, \pm4$ and $n_2 = 0, \pm1, \pm2$ obtained by the generation rule $n_{\rm d} = L_2 n_1 + L_1 n_2$ in (4.23) with $L_1 = 13$ and $L_2 = 9$. The green and yellow areas represent positive and negative integers.

4.2 Numerical analyses for double-periodic cases

4.2.1 Sporadic generation of the Dirac-electron structures

Our theoretical analysis in the previous subsection showed that the generation of the Dirac-electron structures induced by a double-periodic potential is understood by the combination of the indices obtained for the pair of single-periodic cases. For the double-periodic potentials, we again will not completely judge whether the contact "points" are truly gapless or not. However, our theoretical study from the Dirac Hamiltonian can satisfactory explain the different generation of the Dirac-electron structures. We here confirm our prediction of the generation rule (4.23) numerically for $L_1 = 13$, $L_2 = 9$, $v_1 = 0.1$, and $v_2 = 0.1$.

The single-periodic cases $(L_1, v_1) = (13, 0.1)$ and $(L_2, v_1) = (8, 0.1)$ numerically exhibit the consecutive indices $n_1 = 0, \pm1, \pm2, \pm3, \pm4$ and $n_2 = 0, \pm1, \pm2$, respectively (see Sec. 3.2.3). Figure 4.1 is the table of the combination of the indices n_1 and n_2. For example, the index $n_{\rm d} = +5$ is made from the set $(n_1, n_2) = (+2, -1)$. Note that the series of the new Dirac-electron structures do not consecutively continue up to a maximum number. We call this type of sequence of indices *sporadic*. We here show that the generation

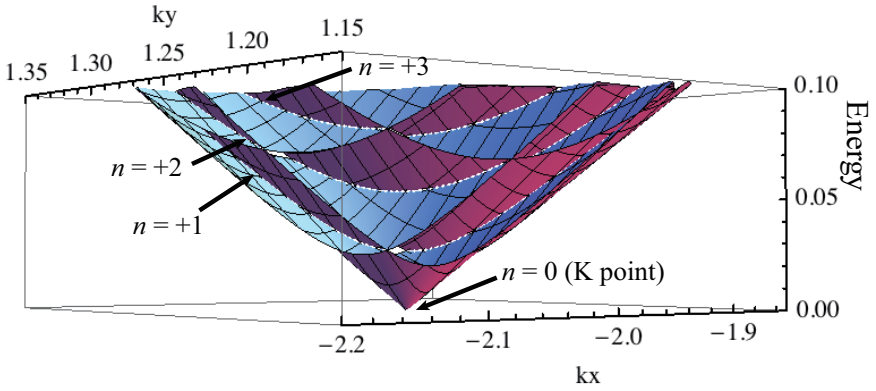

Figure 4.2: The energy spectrum around the K point of the tight-binding model for $L_1 = 13$, $L_2 = 9$, $v_1 = 0.1$, and $v_2 = 0.1$ and the system size $(r_1, r_2) = (10^2, 10^2)$. Only the positive-energy side is shown here. The arrows indicate the contact "points" of the upper and lower bands.

rule (4.23) can explain the sporadic appearance of the new Dirac-electron structures induced by the double-periodic potential.

Let us demonstrate the generation rule (4.23) by numerically diagonalizing the tight-binding model (2.41) under a double-periodic potential (2.43) as the sum of two sine functions V_1 and V_2 with the periods $(L_1, L_2) = (13, 9)$, where the unity means the lattice constant. Therefore, the total period of the double-periodic potential is given by $L = L_1 \times L_2 = 117$. We set the amplitudes of the potentials as $v_1 = 0.1$ and $v_2 = 0.1$. A tight-binding energy spectrum for the system of size $(r_1, r_2) = (10^2, 10^2)$ is illustrated in Fig. 4.2. We here plot the positive energy ranges because the spectrum is symmetric with respect to the Fermi energy $E_{\rm F} = 0$ as in the single-periodic cases. The spectrum over the energy range in Fig. 4.2 also has the band structures and the contact "points". Compared to the single-periodic case in Fig. 3.1, it is hard to find the contact "points" just by watching the spectrum itself. We next study the neighboring energy intervals around the contact "points" in order to realize it.

Figure 4.3 shows the relations between the system size r and the minimum intervals of all contact "points" whose energies are located between the Fermi energy $E_{\rm F} = 0$ and the hopping parameter $t_1 = 1.0$. In the case of the double-periodic potential $L = 117$, we study the system size from

$(r_1, r_2) = (10^2, 10^2)$ to $(10^5, 10^5)$. As the system size r increases, the data series also exhibit the two patterns, the stepwise one and the converging one, which we discussed in Chap. 3. For example, the contact "points" $n_{\rm d} = +1$ and $n_{\rm d} = +2$ in Fig. 4.3 (a) clearly show different patterns.

Figure 4.4 (a), (b), (c), and (d) are the energy intervals around the contact "points" $n_{\rm d} = +1$ and $n_{\rm d} = +2$. The interval around the contact "point" $n_{\rm d} = +1$ keeps showing the linearity even for $r = 10^5$ as illustrated in Fig. 4.4 (b), but the one $n_{\rm d} = +2$ exhibits an energy gap for $r = 10^5$ as in Fig. 4.4 (d). By using the same analysis as in Subsection 3.2.1, the contact "point" $n_{\rm d} = +1$ can be the Dirac-electron structure with an invisible small mass. We thus conclude that the sporadic series of contacts $n_{\rm d} = \{0, 1, 4, 5, 8, 9\}$, $\{10, 13, 14, 17, 18\}$, $\{22, 23, 26, 27\}$, $\{31, 35, 36\}$, and $\{40, 44\}$ can have gapless structures, where curly brackets indicate that each set is plotted in Fig. 4.4 (a), (b), (c), and (d), respectively.

Let us compare our numerical results with the predicted numbers as shown in the table of the combination in Fig. 4.1. All the indices of the new Dirac-electron structures which we obtained by the numerical analyses appear on the table, as we emphasized with the red boxes. This consistency clearly shows that the generation rule (4.23) can explain the *sporadic* appearance of the new Dirac-electron structures.

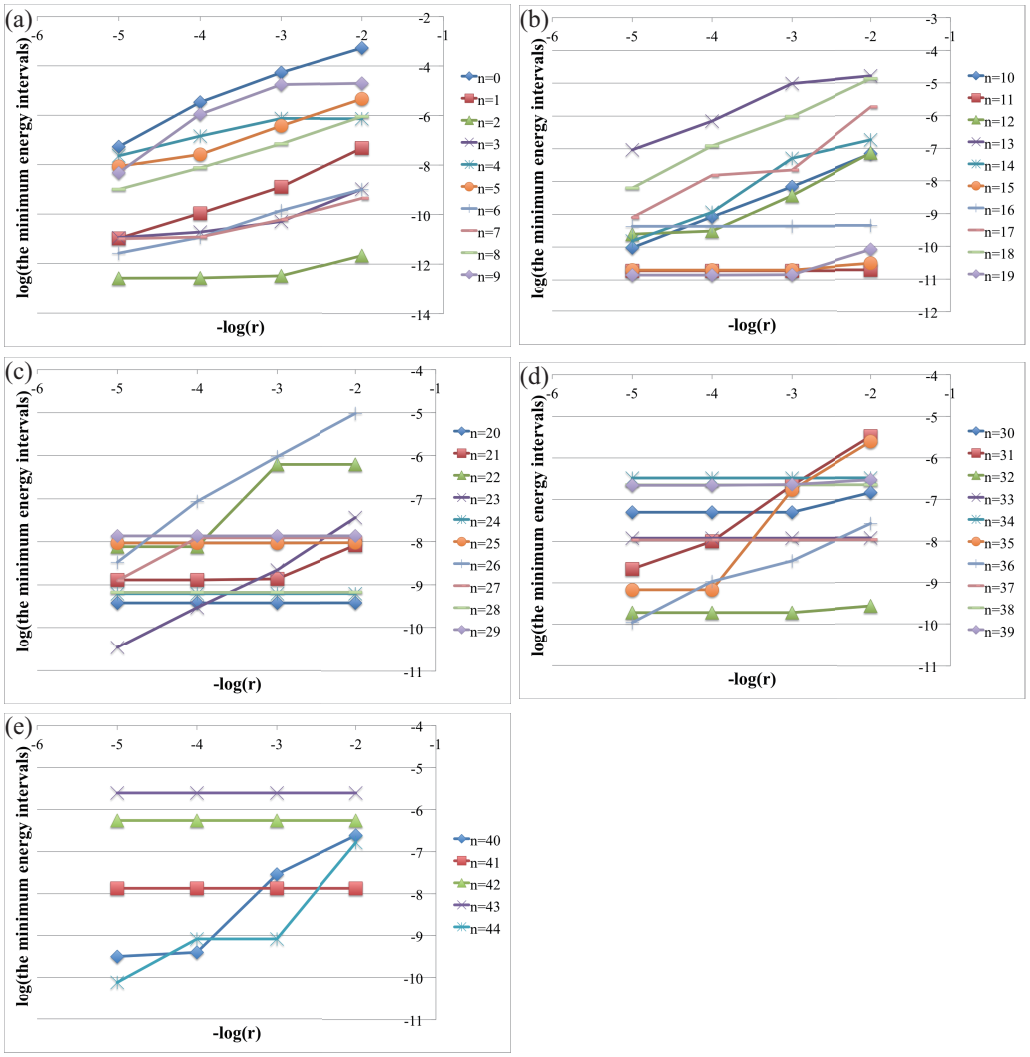

Figure 4.3: Logarithmic plots of the system-size dependence of the minimum energy interval as the contact "points" for $(L_1, L_2, v_1, v_2) = (13, 9, 0.1, 0.1)$. The data series of $0 \leq n_{\mathrm{d}} \leq 9$, $10 \leq n_{\mathrm{d}} \leq 19$, $20 \leq n_{\mathrm{d}} \leq 29$, $30 \leq n_{\mathrm{d}} \leq 39$, and $40 \leq n_{\mathrm{d}} \leq 44$ are plotted in (a) to (e), respectively.

(a) n_d=1 (10^3)

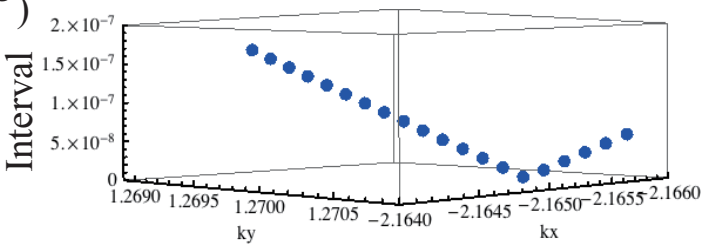

(b) n_d=1 (10^5)

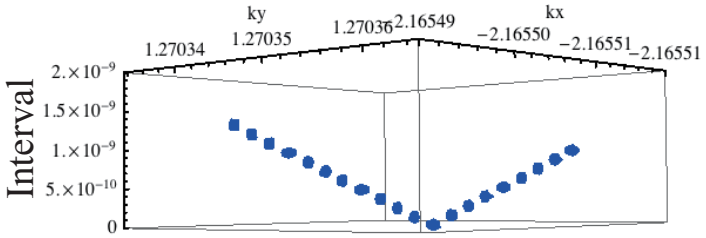

(c) n_d=2 (10^3)

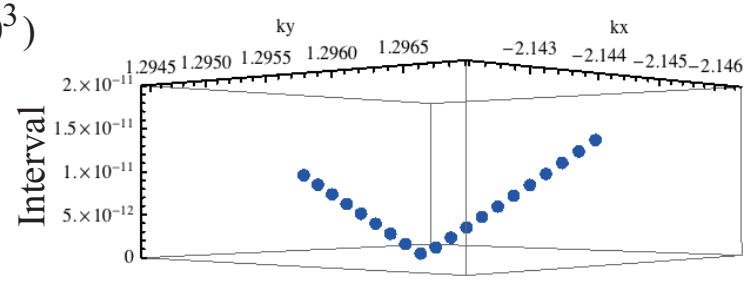

(d) n_d=2 (10^5)

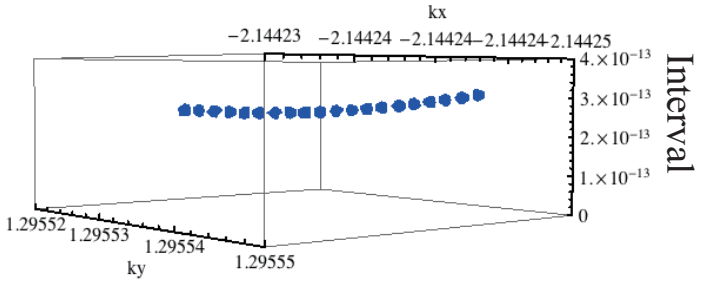

Figure 4.4: The energy intervals of neighboring energy eigenvalues around the contact "points" $n = 1$ ((a) for $r_1 = r_2 = 10^3$ and (b) for 10^5) and $n = 2$ ((a) for $r_1 = r_2 = 10^3$ and (b) for 10^5) for the case of $(L_1, L_2, v_1, v_2) = (13, 9, 0.1, 0.1)$.

Finally, we give a word of caution in the numerical confirmation of the Dirac-electron structures. When the energy interval is a very small finite value, we are not able to find out the gapful structure numerically because we cannot increase the system size forever. In this case, changing the amplitude of the double-periodic potential can resolve the problem as we demonstrate hereafter.

We here show an example from double-periodic systems $L_1 = 13$ and $L_2 = 8$. Figure 4.5 is the combination table for a double-periodic potential $(L_1, L_2, v_1, v_2) = (13, 8, 0.1, 0.1)$ and $(13, 8, 0.1, 0.6)$. The two systems have the same table because the indices n_1 for $L = 13$ and n_2 for $L = 8$ have the same ranges although the potential for $L = 8$ is different. Almost all indices of these cases numerically show the same results; we especially emphasize the possible gapless structures in the red boxes in Fig. 4.5.

We, however, find an exceptional case $n_{\rm d} = 20$ which yields different results for $v_2 = 0.1$ and $v_2 = 0.6$. The generation rule (4.23) would predict that it would not be a new Dirac-electron structures; for the double-periodic potential $(L_1, L_2) = (13, 8)$, the appearance of the cone $n_{\rm d} = +20$ needs $n_1 = -4$ and $n_2 = +4$, which is larger than the maximum index for the single-periodic potential $(L, v) = (8, 0.1)$ (see Figs, 3.15 (a) and 3.19 (c)).

The numerical result for $n_{\rm d} = 20$ does not show a gapful structure for $v_2 = 0.1$ (see Fig. 4.6 (a) and Fig. 4.7 (a)), similarly to the predicted Dirac-electron structure $n_{\rm d} = 21$ for $v_2 = 0.1$ (Fig. 4.6 (a) and Fig. 4.7 (c)). On the other hand, the numerical results for $v_2 = 0.6$ have different trends between the indices $n_{\rm d} = 20$ and 21. The result for $n_{\rm d} = 21$ with $v_2 = 0.6$ indicates a possible gapless structure, (see Fig. 4.6 (b) and Fig. 4.7 (d)), but the result for $n_{\rm d} = 20$ with $v_2 = 0.6$ shows a gapful structure (see Fig. 4.6 (b) and Fig. 4.7 (b)). We found that all other points show the same results while we change the amplitude $v_2 = 0.1$ to 0.6. We therefore conclude that the band contact $n_{\rm d} = +20$ for $v_2 = 0.1$ has a too small energy gap to detect within the current system size.

4.2.2 Anisotropy of the Dirac-electron structures in the double-periodic systems

The difference between the double-periodic and the single-periodic cases also appears in the anisotropy of the new Dirac-electron structures. All the ratios of the slopes in the directions $\vec{b}_1/2+\vec{b}_2$ and $\vec{b}_1$ in the cases of the single-periodic

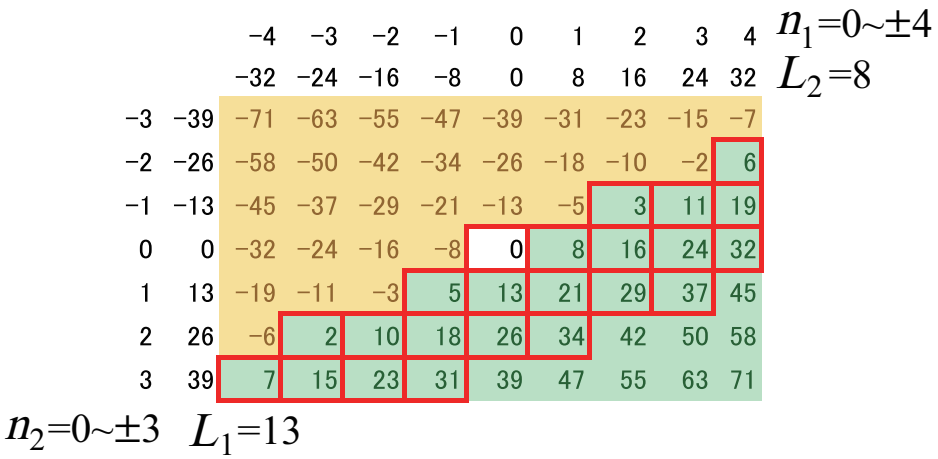

		−4	−3	−2	−1	0	1	2	3	4
		−32	−24	−16	−8	0	8	16	24	32
−3	−39	−71	−63	−55	−47	−39	−31	−23	−15	−7
−2	−26	−58	−50	−42	−34	−26	−18	−10	−2	6
−1	−13	−45	−37	−29	−21	−13	−5	3	11	19
0	0	−32	−24	−16	−8	0	8	16	24	32
1	13	−19	−11	−3	5	13	21	29	37	45
2	26	−6	2	10	18	26	34	42	50	58
3	39	7	15	23	31	39	47	55	63	71

Figure 4.5: The table of the combination of the indices $n_1 = 0, \pm1, \pm2, \pm3, \pm4$ and $n_2 = 0, \pm1, \pm2, \pm3$ with $L_1 = 13$ and $L_2 = 8$ obtained by the generation rule $n_{\rm d} = L_2 n_1 + L_1 n_2$ in (4.23). The green and yellow areas represent positive and negative integers. The numbers in the red boxes correspond to the contact points at which we numerically confirmed the possible Dirac-electron structures.

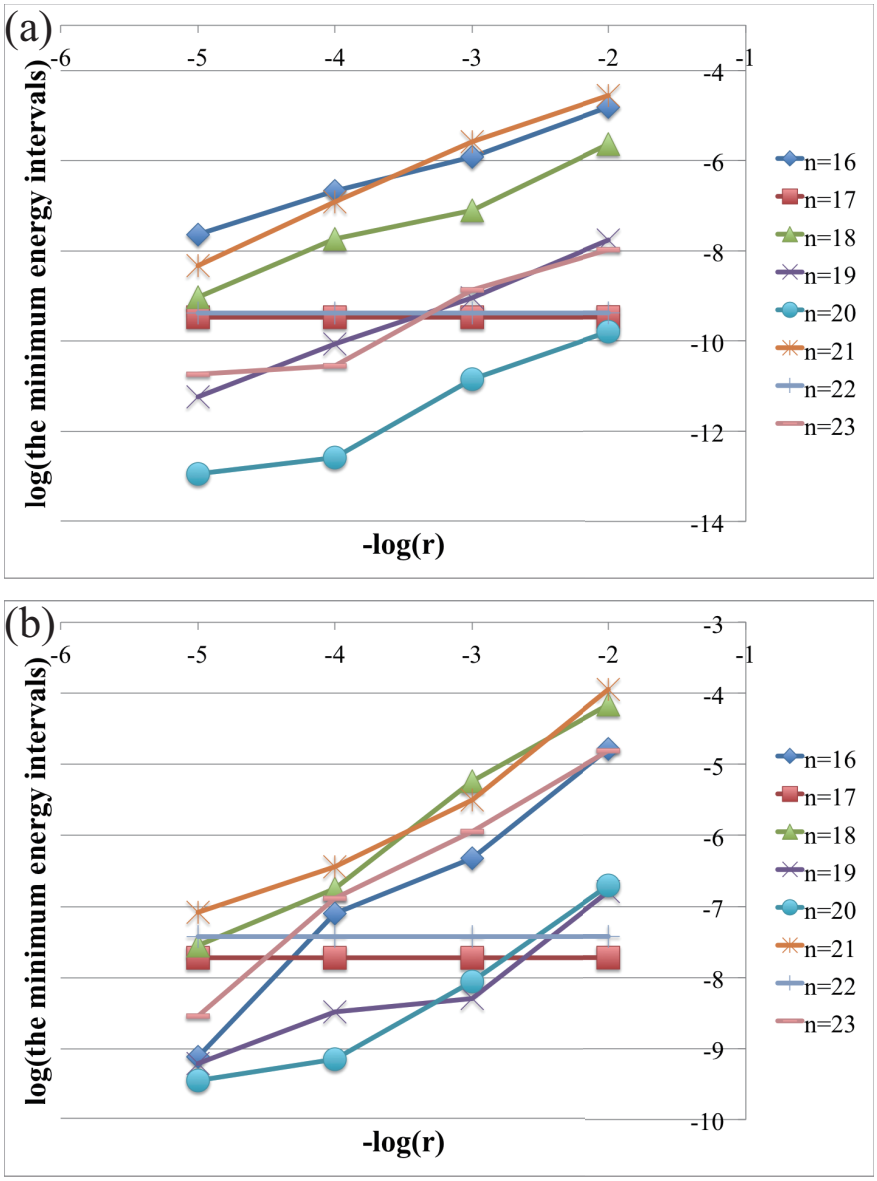

Figure 4.6: Logarithmic plots of the system-size dependence of the minimum energy interval at the contact "point" for (a) $(L_1, L_2, v_1, v_2) = (13, 8, 0.1, 0.1)$ and (b) $(L_1, L_2, v_1, v_2) = (13, 8, 0.1, 0.6)$.

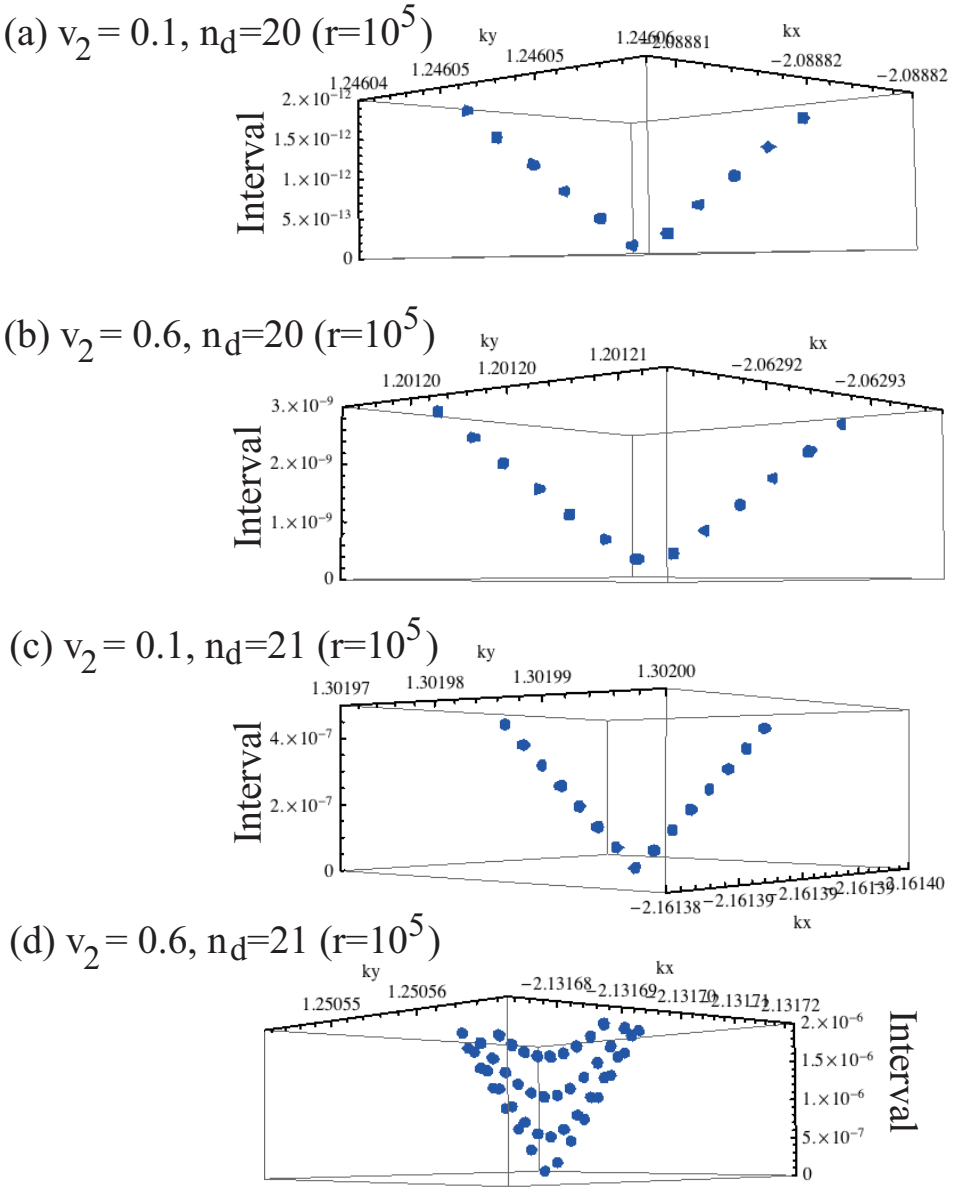

Figure 4.7: The energy intervals of neighboring energy eigenvalues around the contact "point" $n_{\rm d} = 20$ ((a) for $r_1 = r_2 = 10^5$ and $v_2 = 0.1$ and (b) for 10^5 and $v_2 = 0.6$) and $n_{\rm d} = 21$ ((c) for $r_1 = r_2 = 10^5$ and $v_2 = 0.1$ and (d) for 10^5 and $v_2 = 0.6$) .

potentials have shown nearly exponential decays as the cone indices increase (see Figs, 3.18 and 3.19). We predict that the ratio obtained in the cases of the double-periodic potential, however, shows a completely different trend. The different trend is explained by studying the Dirac Hamiltonian under the double-periodic potential. Equation (4.21) indicates that the ratio of the slopes $|f_{n_{\rm d}}|^2$ for the cone index $n_{\rm d}$ is given by the product $|f_{1,n_1}|^2 \times |f_{2,n_2}|^2$, where the terms $|f_{1,n_1}|^2$ and $|f_{2,n_2}|^2$ are the ratios in the single-periodic cases for the indices n_1 and n_2, respectively. Since n_1 and n_2 do not change monotonically as we increase $n_{\rm d}$, the ratios in the double-periodic cases should fluctuate widely as the the indices increase.

In the double-periodic cases, we can see a behavior different from the single-periodic cases by studying the anisotropy of the new Dirac-electron structures. Figure 4.8 (a) shows the ratio of the slopes in the two directions from the numerical results in the double-periodic case $(L_1, L_2, v_1, v_2) = (13, 9, 0.1, 0.1)$. It fluctuates much more widely than the one illustrated in Fig. 3.18. Figure 4.8 (b) shows comparison between the numerical results in the double-periodic case (the blue diamonds) and the ratios calculated from the numerical results in the single-periodic cases $(L, v) = (13, 0.1)$ and $(9, 0.1)$ (the red triangles). The two data set relatively have a good agreement in most points except for the data points for the indices $n_{\rm d} = +1, +10, +23$, which have stronger anisotropies than expected from the single-periodic cases. In these exceptional cases, the index consists of larger numbers of the indices n_1 and n_2, and thus they are near the end of the table in Fig. 4.1. We plot the ratio of the numerical results in the double-periodic case and the calculated values in the single-periodic cases on the combination table (see Fig. 4.9). The ratios for the index $-n_{\rm d}$ are the same as that for $+n_{\rm d}$. It is clear that the indices near the edge of the table have great mismatches between the two ratios. The larger indices n_1 and n_2 correspond to the new Dirac-electron structures whose energies are far away from the Fermi energy, and therefore we presume that the difference between the actual energy spectrum and the linear dispersion causes the mismatches.

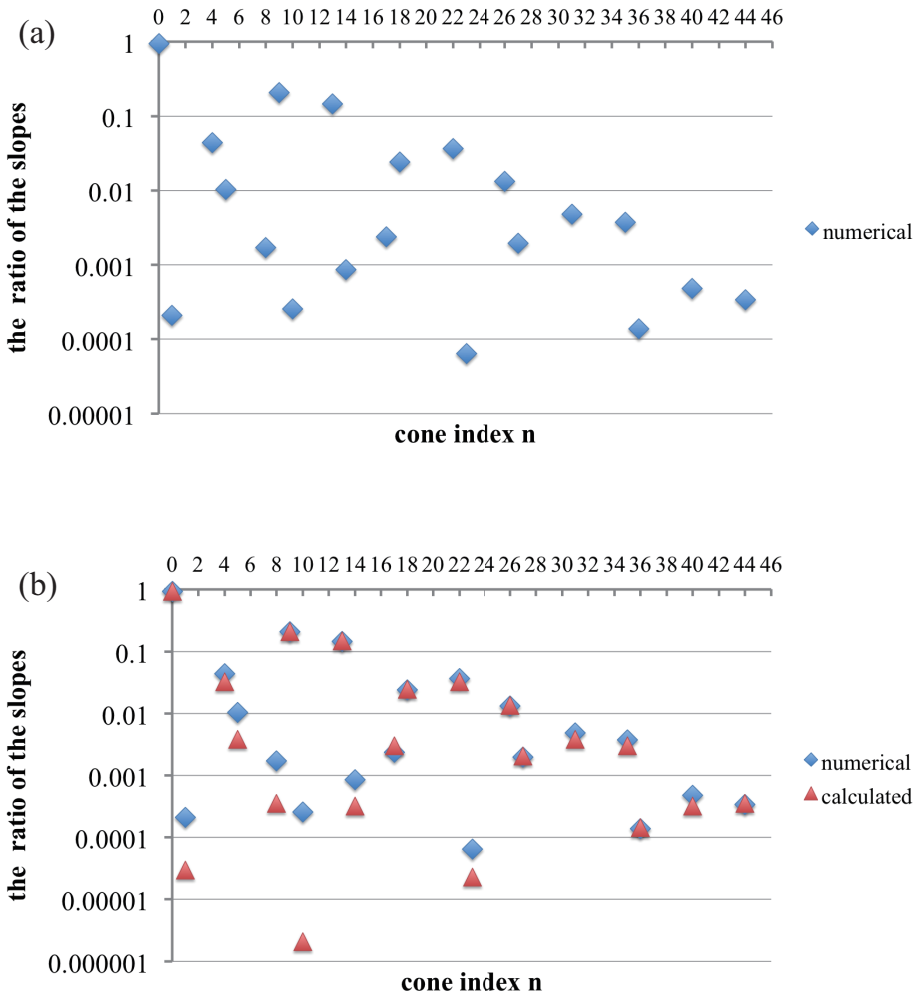

Figure 4.8: The ratio of the slopes in the two directions $(1/2)\vec{b}_1 + \vec{b}_2$ and $\vec{b}_1$. The blue diamonds potted in (a) and (b) indicate the numerical results directly obtained from the double-periodic case $(L_1, L_2, v_1, v_2) = (13, 9, 0.1, 0.1)$. The red triangles plotted in (b) indicate that calculated values by using Eq. (4.21) and the numerical data from the single-periodic cases $(L, v) = (13, 0.1)$ and $(L, v) = (9, 0.1)$.

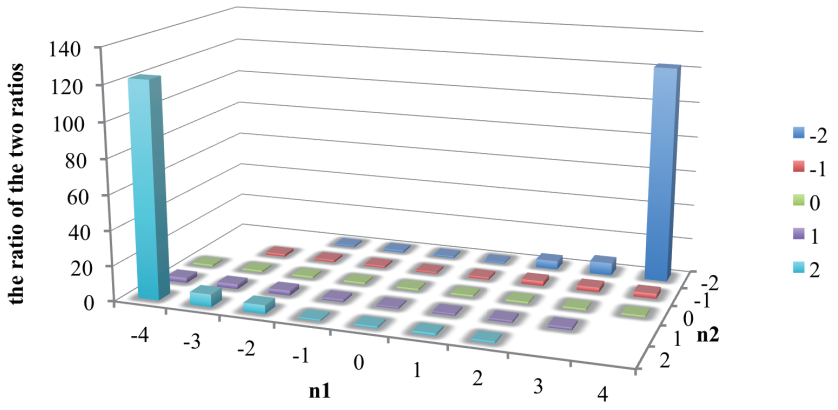

Figure 4.9: The ratio of the slopes' ratios in the double-periodic case to the ratio of slopes in the single-periodic cases. We illustrate the ratios on the combination table in Fig. 4.1.

4.3 Energy cutoff in the double-periodic cases

In the previous subsection, we revealed that the new Dirac-electron structures appear sporadically in the double-periodic cases because each single-periodic potential has an energy cutoff determined by the band width and the potential amplitude. In the present section, we show how the energy cutoffs for the two single-periodic potentials determine the energy cutoff for the resulting double-periodic potential. After examining a few examples, we will conclude that the lower energy cutoff between those for the two single-periodic potentials determines the maximum indices of *both* components n_1 and n_2 in the generation rule (4.23).

When we increase the amplitude v of the single-periodic potential, the maximum index $N(v)$ of the Dirac-electron structures, in general, becomes smaller. In other words, the Dirac-electron structures appear in the energy range $n \leq N(v) \simeq \lfloor L\Delta E(v)/\pi \rfloor$. We here consider a double-periodic system $V = V_1 + V_2$, where V_1 and V_2 have the periods L_1 and L_2, respectively. As we only increase the amplitude v_2, the corresponding cutoff $\Delta E_2(v_2)$ decreases but $\Delta E_1(v_1)$ does not change. We will, however, reveal that *both* indices n_1

Table 4.1: The list of the indices n_1 and n_2 whose energies are below the lower cutoff $\Delta E_2(v_2)$. When we set the amplitudes $v_1 = v_2 = 0.1$, the energy cutoffs are equal to the hopping parameter $t_1 = 1.0$.

$L_1 = 13,$	$L_2 = 9$	n_1	n_2
$v_1 = 0.1,$	$v_2 = 0.1$	$0, \ldots, \pm 4$	$0, \ldots, \pm 2$
$v_1 = 0.1,$	$v_2 = 0.25$	$0, \ldots, \pm 2$	$0, \pm 1$
$v_1 = 0.1,$	$v_2 = 0.44$	$0, \pm 1$	0

and n_2 are restricted by the lower one of $\Delta E_1(v_1)$ and $\Delta E_2(v_2)$:

$$n_i \leq \left\lfloor \frac{L_i}{\pi} \min\left(\Delta E_1(v_1), \Delta E_2(v_2)\right) \right\rfloor \tag{4.24}$$

for $i = 1$ and 2.

First, let us focus on a double-periodic case with $L_1 = 13$ and $L_2 = 9$. For small amplitudes $v_1 = v_2 = 0.1$, the energy cutoffs $\Delta E_1(v_1 = 0.1)$ and $\Delta E_2(v_2 = 0.1)$, which yield $n_1 = 0, \ldots, \pm 4$ and $n_2 = 0, \ldots, \pm 2$, respectively, are approximately equal to the hopping parameter $t_1 = 1.0$, as is indicated by the dotted line in the right half of Fig. 4.10 (the first row of Table 4.1). Our numerical analyses have shown that the table of the combination based on these values indeed explains the sporadic generation of the new Dirac-electron structures (see Section 4.2).

Let us next increase the amplitude v_2 to 0.25 for the single-periodic potential $L_2 = 9$ (the second row of Table 4.1; see Subsection 3.2.3). This decreases the energy cutoff for $L_2 = 9$ to $\Delta E_2(v_2 = 0.25)$ and hence extinguishes the Dirac-electron structure $n_2 = 2$. We would then expect that the generation of the new Dirac-electron structures might be ruled by the indices $n_1 = 0, \ldots, \pm 4$ and $n_2 = 0, \pm 1$. The table of the combination in Fig. 4.11 (a) would then predict a sporadic series of indices up to $n_{\rm d} = 40$. Our numerical calculation, however, shows that the new Dirac-electron structure sporadically appears only put to $n_{\rm d} = 31$.

We thereby claim that the relevant range of the index n_1 is also restricted by the energy cutoff ΔE_2, not only by ΔE_1, as shown in Eq. (4.24). According to this empirical rule, the five indices crossed out in Fig. 4.11 (a) are not eligible for the new Dirac-electron structures anymore, which explains the numerical results.

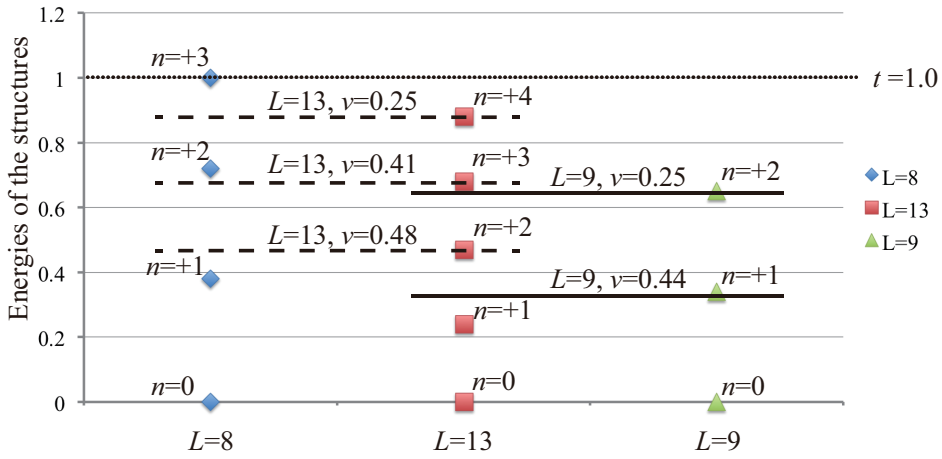

Figure 4.10: The energies of the new Dirac-electron structures of the single-periodic potentials. The blue diamonds, the red square, and the green triangles represent the energies for $L = 9$, $L = 8$, and $L = 13$, respectively. The dotted line, the solid line, and the dashed line represent the hopping element $t_1 = 1$, the energy cutoff for $L = 9$, and the one for $L = 13$, respectively.

Let us confirm the rule further by increasing the amplitude v_2 more to 0.44. The rule (4.24) dictates that as we increase the amplitude v_2 to 0.44, the cone indices $n_1 = 0, \pm 1$ and $n_2 = 0$ below the lower cutoff $\Delta E_2(v_2 = 0.44)$ are only relevant (see the right half of Fig. 4.10 and Table 4.1). The combination table in Fig. 4.11 (b) now predicts only the Dirac-electron structures $n_{\rm d} = 0$ and 9, which is indeed consistent with our numerical result.

We similarly confirm the rule (4.24) in the case $L_1 = 13$ and $L_2 = 8$. When we increase the amplitude v_1 as 0.25, 0.41, and 0.48, the relevant cone indices below the cutoff $\Delta E_1(v_1)$ decreases as is shown in the left half of Fig. 4.10 and Table 4.2. The point here is again that the index n_2 is also restricted accordingly. The combination table in Figure 4.12 then perfectly predicts the numerical results. The indices crossed out in Fig. 4.12 are indeed not Dirac-electron structures. We thereby conclude that in the combination table for the possible Dirac-electron structures in the double-periodic case, we must use the cone indices n_1 and n_2 both lower than the minimum of ΔE_1 and ΔE_2.

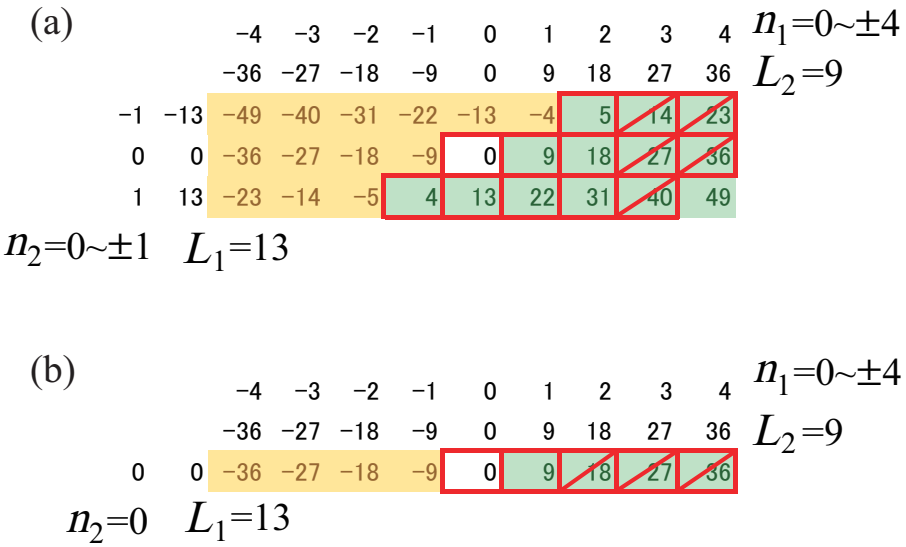

Figure 4.11: Tables of the combinations of the indices (a) $n_1 = 0, \ldots, \pm 4$ and $n_2 = 0, \pm 1$ and (b) $n_1 = 0, \ldots, \pm 4$ and $n_2 = 0$. They correspond to the double-periodic cases $(L_1, L_2, v_1, v_2) = (13, 9, 0.1, 0.25)$ and $(L_1, L_2, v_1, v_2) = (13, 9, 0.1, 0.44)$, respectively. The green and the yellow areas represent positive and negative integers. The numbers in the red boxes not crossed out are the possible Dirac-electron structures which we numerically found while the ones crossed out are not Dirac-electron structures.

Table 4.2: The list of the indices n_1 and n_2 whose energies are below the lower cutoff $\Delta E_1(v_1)$. When we set the amplitudes $v_1 = v_2 = 0.1$, the energy cutoffs are equal to the hopping parameter $t_1 = 1.0$.

$L_1 = 13,$	$L_2 = 8$	n_1	n_2
$v_1 = 0.1,$	$v_2 = 0.1$	$0, \ldots, \pm 4$	$0, \ldots, \pm 3$
$v_1 = 0.25,$	$v_2 = 0.1$	$0, \ldots, \pm 3$	$0, \ldots, \pm 2$
$v_1 = 0.41,$	$v_2 = 0.1$	$0, \ldots, \pm 2$	$0, \pm 1$
$v_1 = 0.48,$	$v_2 = 0.1$	$0, \pm 1$	$0, \pm 1$

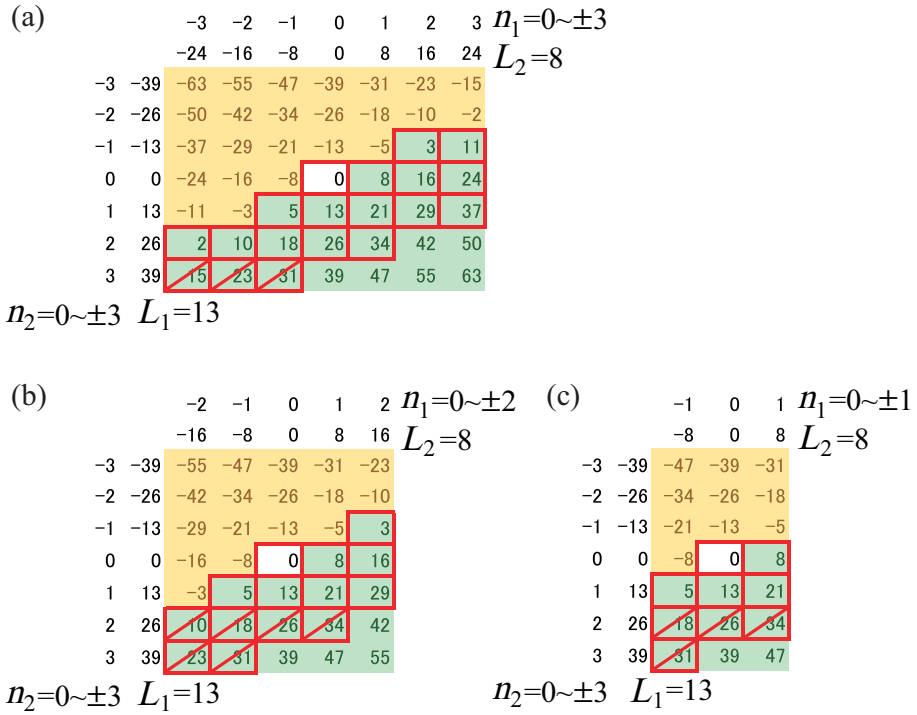

Figure 4.12: Tables of the combinations of the indices in the double-periodic case $(L_1, L_2, v_2) = (13, 8, 0.1)$; (a) $n_1 = 0, \ldots, \pm 3$ and $n_2 = 0, \ldots, \pm 3$, (b) $n_1 = 0, \ldots, \pm 2$ and $n_2 = 0, \ldots, \pm 3$, and (c) $n_1 = 0, \pm 1$ and $n_2 = 0, \ldots, \pm 3$ for the amplitudes $v_1 = 0.25$, 0.41, and 0.48, respectively. The green and the yellow areas represent positive and negative integers. The numbers in the red boxes not crossed out are the possible Dirac-electron structures which we numerically found while the ones crossed out are not Dirac-electron structures.

4.4 Dirac electron systems under the double-periodic potentials

In this section we set the energy cutoff as a free parameter in order to generalize the argument to various Dirac electron systems under superlattice potentials [82, 83]. For the shape of the argument, we assume from now on that Eq. (4.23) can represent the generation of the Dirac *cones* for the various Dirac electron systems.

Our studies show that there are three cases of the energy cutoff ΔE regarding the appearance of the new Dirac cones in the double-periodic cases (Fig. 4.13). The three cases are mainly divided by the two values $\Delta E = \pi$

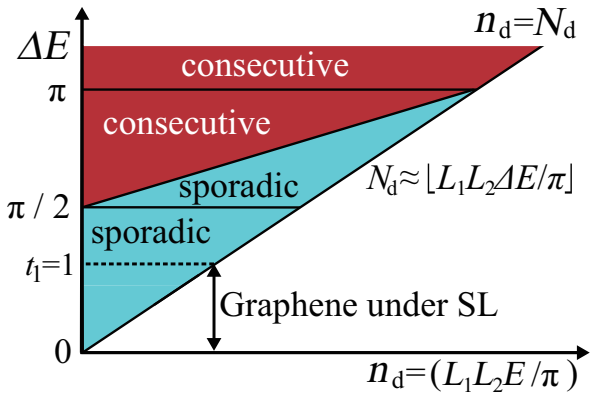

Figure 4.13: A schematic of the appearance of the new Dirac cones. The dark red area is filled up by the new points. In the light blue area the points appear sporadically. The range of the energy cutoff of graphene under the superlattice potential (SL) is represented by the double-headed arrow ($E_{\rm F}(=0) \leq \Delta E \leq t_1(=1)$).

and $\pi/2$. In the first case $\Delta E \geq \pi$, all new cones appear consecutively up to $N_{\rm d} \simeq \lfloor L_1 L_2 \Delta E/\pi \rfloor$, which coincides with the case of a single sine function (cf. Eq. (3.30)). In the second case $\pi/2 \leq \Delta E < \pi$, the new cones fill up the energy range $|E| < 2\Delta E - \pi$, or $|n_{\rm d}| < ((2\Delta E/\pi) - 1)L$. In the energy range $2\Delta E - \pi < |E| < \Delta E$, the new cones appear sporadically. In the third case $\Delta E < \pi/2$, the new cones appear sporadically in all energy range $|E| < \Delta E$.

Graphene under the superlattice potential corresponds to the third case;

the cutoff varies in the range $0.0 < \Delta E < 1.0$. In the following paragraphs we explain the appearance of the three cases by considering the finite simple continued-fraction expansion [81] of the rational number $r = L_1/L_2$ (see Appendix A).

4.4.1 General solution of the generation rule

We derive the general solution of the generation rule (4.23) as the first step of our effort. We rewrite the generation rule (4.23) by using the notation in the finite simple continued fraction expansion:

$$n_{\rm d} = B_\nu n_1 + A_\nu n_2, \tag{4.25}$$

where $A_\nu = L_1$ is the numerator and $B_\nu = L_2$ is the denominator that are coprime integers (see Appendix A). The general solutions of the above equation is given by

$$n_1 = (-1)^\nu n_{\rm d} A_{\nu-1} + A_\nu m \tag{4.26}$$

and

$$n_2 = (-1)^{\nu-1} n_{\rm d} B_{\nu-1} - B_\nu m, \tag{4.27}$$

where m is an arbitrary integer. These solutions can be derived as follows.

First, we consider the case in which the index $n_{\rm d}$ is unity. The equation is known as a linear Diophantine equation or Bézout's identity [86]:

$$B_\nu n_1 + A_\nu n_2 = 1. \tag{4.28}$$

We can see that

$$n_1^* = (-1)^\nu A_{\nu-1}, \quad n_2^* = (-1)^{\nu-1} B_{\nu-1} \tag{4.29}$$

are special solutions by substituting them into Eq. (4.28) and applying the recurrence formulas (A.11) and (A.12):

$$\begin{aligned}
&B_\nu n_1^* + A_\nu n_2^* = (-1)^\nu A_{\nu-1} B_\nu + (-1)^{\nu-1} A_\nu B_{\nu-1} \\
&= (-1)^\nu A_{\nu-1}(b_\nu B_{\nu-1} + B_{\nu-2}) + (-1)^{\nu-1}(b_\nu A_{\nu-1} + A_{\nu-2}) B_{\nu-1} \\
&= (-1)^\nu A_{\nu-1} B_{\nu-2} + (-1)^{\nu-1} A_{\nu-2} B_{\nu-1} \\
&= (-1)^\nu A_{\nu-3} B_{\nu-2} + (-1)^{\nu-1} A_{\nu-2} B_{\nu-3} \\
&= \ldots .
\end{aligned} \tag{4.30}$$

By continuing the above transformation we finally obtain

$$B_\nu n_1^* + A_\nu n_2^* = (-1)^0 A_{-1} B_0 + (-1)^{-1} A_0 B_{-1} = 1 \tag{4.31}$$

for even ν and

$$B_\nu n_1^* + A_\nu n_2^* = (-1)^1 A_0 B_{-1} + (-1)^0 A_{-1} B_0 = 1 \tag{4.32}$$

for odd ν, because $A_{-1} = B_0 = 1$ and $B_{-1} = 0$. We thus see that the numbers n_1^* and n_2^* in Eq. (4.29) are special solutions of Eq. (4.28).

Second, we set n_d to an integer greater than unity. The derivation of special solutions are almost the same as in the case of $n_\mathrm{d} = 1$. The numbers

$$n_\mathrm{d} n_1^* = (-1)^\nu n_\mathrm{d} A_{\nu-1}, \quad n_\mathrm{d} n_2^* = (-1)^{\nu-1} n_\mathrm{d} B_{\nu-1} \tag{4.33}$$

are obviously special solutions of Eq. (4.25) because

$$B_\nu (n_\mathrm{d} n_1^*) + A_\nu (n_\mathrm{d} n_2^*) = n_\mathrm{d} (B_\nu n_1^* + A_\nu n_2^*) = n_\mathrm{d}. \tag{4.34}$$

The general solutions of Eq. (4.25) are given by the special solutions (4.33). We have

$$B_\nu (n_1 - n_\mathrm{d} n_1^*) + A_\nu (n_2 - n_\mathrm{d} n_2^*) = 0 \tag{4.35}$$

by subtracting Eq. (4.34) from Eq. (4.25). Substituting the special solutions (4.33) into Eq. (4.35), we have

$$B_\nu (n_1 - (-1)^\nu n_\mathrm{d} A_{\nu-1}) = A_\nu ((-1)^{\nu-1} n_\mathrm{d} B_{\nu-1} - n_2). \tag{4.36}$$

Since A_ν and B_ν are coprime, the number in the parentheses on the left-hand side must be a multiple of A_ν and that on the right-hand side must be a multiple of B_ν: Thus it yields

$$n_1 - (-1)^\nu n_\mathrm{d} A_{\nu-1} = m A_\nu \tag{4.37}$$

$$(-1)^{\nu-1} n_\mathrm{d} B_{\nu-1} - n_2 = m B_\nu, \tag{4.38}$$

where m is an arbitrary integer. We thereby have the general solutions of Eq.(4.25) in the forms of

$$n_1 = (-1)^\nu n_\mathrm{d} A_{\nu-1} + A_\nu m, \tag{4.39}$$

$$n_2 = (-1)^{\nu-1} n_\mathrm{d} B_{\nu-1} - B_\nu m, \tag{4.40}$$

which are Eqs. (4.26) and (4.27).

4.4.2 Proof of the appearance of the three cases

In this section, we show the appearance of the three cases of the generation of the new Dirac cones in terms of the energy cutoff ΔE.

We apply the restrictions of the indices

$$|n_i| \leq N_i \simeq \left\lfloor \frac{L_i}{\pi} \Delta E \right\rfloor \quad \text{for} \quad i = 1, 2 \tag{4.41}$$

to the general solutions (4.39) and (4.40), where ΔE is in practice given by $\min(\Delta E_1(v_1), \Delta E_2(v_2))$ as in (4.24). We thereby have

$$|(-1)^\nu n_\mathrm{d} A_{\nu-1} + A_\nu m| \leq N_1 \tag{4.42}$$

and

$$\left|(-1)^{\nu-1} n_\mathrm{d} B_{\nu-1} - B_\nu m\right| \leq N_2. \tag{4.43}$$

We can also cast them into the forms

$$\left| \frac{A_{\nu-1}}{A_\nu} n_\mathrm{d} - m \right| \leq \frac{N_1}{A_\nu} \tag{4.44}$$

and

$$\left| \frac{B_{\nu-1}}{B_\nu} n_\mathrm{d} - m \right| \leq \frac{N_2}{B_\nu}, \tag{4.45}$$

where we replaced $(-1)^\nu m$ with m. A rational number has two kinds of the expansion $\{A_\nu, B_\nu\}$ and $\{A'_\nu, B'_\nu\}$ (see Appendix A), which result in different forms of the inequalities. We can show, however, that they are equivalent to each other (see Appendix A.5).

We rewrite the inequalities (4.44) and (4.45) in terms of the energy cutoff ΔE to show the appearance of the three cases (see Fig. 4.13). We use Eq. (4.41) to rewrite the right-hand side of Eq. (4.44) with the use of $A_\nu = L_1$, while we use the expression of the energy of the new Dirac point is

$$E(n_\mathrm{d}) = \frac{\pi}{L_1 L_2} n_\mathrm{d} = \frac{\pi}{A_\nu B_\nu} n_\mathrm{d} \tag{4.46}$$

for the double-periodic potential in order to rewrite the left-hand side. We thereby have

$$|A_{\nu-1} B_\nu E(n_\mathrm{d}) - m\pi| < \Delta E. \tag{4.47}$$

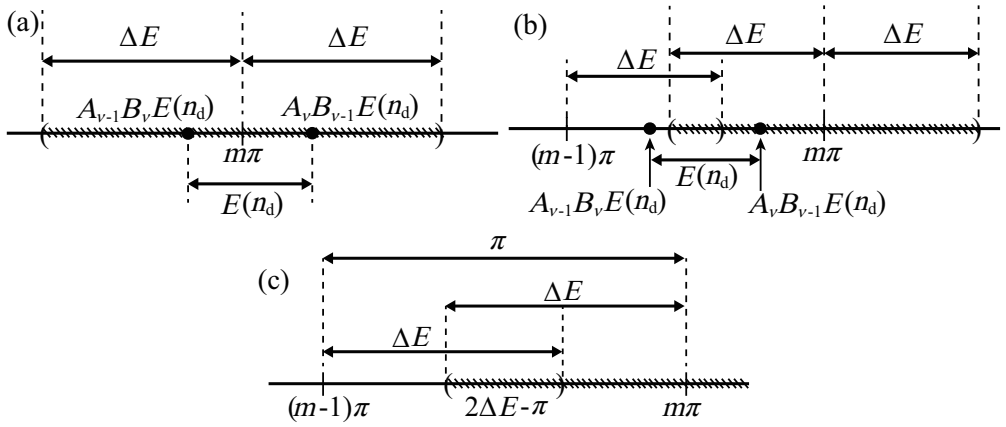

Figure 4.14: The inequalities (4.44) represented on a line. The intervals whose center is $m\pi$ are represented as the hatched areas. **(a)** The case in which the two points $A_{\nu-1}B_\nu E(n_{\rm d})$ and $A_\nu B_{\nu-1}E(n_{\rm d})$ are in the same interval. **(b)** The case in which the two points are in different intervals. **(c)** The case in which the overlap of the intervals is $2\Delta E - \pi$ in the second case $\pi/2 \leq \Delta E < \pi$.

The inequality (4.45) is also cast into the form

$$|A_\nu B_{\nu-1}E(n_{\rm d}) - m\pi| < \Delta E. \tag{4.48}$$

When both inequalities (4.47) and (4.48) hold for the same integer m, the new Dirac cones which is indexed as $n_{\rm d}$ appear in the energy spectrum.

In order to show the three cases of the appearance of the new Dirac points in Fig. 4.13, we interpret the inequalities (4.47) and (4.48) as the following problem. Let us consider a line on which there are discrete values $\{m\pi\}$, where $\{m\}$ are integers (Fig. 4.14). When the two points $A_{\nu-1}B_\nu E(n_{\rm d})$ and $A_\nu B_{\nu-1}E(n_{\rm d})$ are located in an interval $(m - \Delta E, m + \Delta E)$, the new Dirac cone $E(n_{\rm d})$ appears in the energy spectrum (see Fig. 4.14 (a)). On the other hand, the new Dirac cones do not appear when the two points are not in a common interval (see Fig. 4.14 (b)).

The distance between the two points is given by

$$A_\nu B_{\nu-1}E(n_{\rm d}) - A_{\nu-1}B_\nu E(n_{\rm d}) = (-1)^{\nu+1}E(n_{\rm d}), \tag{4.49}$$

where we use Eq. (A.13). For simplicity, we assume the case $A_\nu B_{\nu-1} > A_{\nu-1}B_\nu$ and $E(n_{\rm d}) > 0$ in this paragraph. The following arguments can be

applied to the case $A_\nu B_{\nu-1} < A_{\nu-1} B_\nu$ by replacing the symbols. In this paragraph, we thus rewrite the distance (4.49) as

$$A_\nu B_{\nu-1} E(n_\mathrm{d}) - A_{\nu-1} B_\nu E(n_\mathrm{d}) = E(n_\mathrm{d}), \tag{4.50}$$

which is greater than zero.

First we show that all new cones are consecutive in the first case $\Delta E \geq \pi$ even for the double-periodic potentials. When the energy cutoff ΔE is greater than π, we can represent the value $A_\nu B_{\nu-1} E(n_\mathrm{d})$ as

$$A_\nu B_{\nu-1} E(n_\mathrm{d}) = m\pi + \delta, \tag{4.51}$$

where

$$0 < \delta < \Delta E. \tag{4.52}$$

Note that we can do so only in the case $\Delta E \geq \pi$. Equation (4.51) leads to the inequality (4.48).

We next prove the other inequality (4.47) by contradiction. Let us assume

$$|A_{\nu-1} B_\nu E(n_\mathrm{d}) - m\pi| \geq \Delta E. \tag{4.53}$$

The value in the signs of the absolute value in Eq. (4.53) can be positive or negative. We consider the positive case as the first step. We rewrite the inequality (4.53) by using the relation (4.50) as

$$A_{\nu-1} B_\nu E(n_\mathrm{d}) - m\pi = [A_\nu B_{\nu-1} E(n_\mathrm{d}) - E(n_\mathrm{d})] - m\pi \geq \Delta E. \tag{4.54}$$

Equation (4.51) then gives

$$\delta \geq \Delta E + E(n_\mathrm{d}). \tag{4.55}$$

Let us remember that the energy of the new Dirac point is positive $E(n_\mathrm{d}) > 0$ (see Eq. (4.50)). Hence we obtain $\delta > \Delta E$. This inequality contradicts the condition (4.52).

As the second step, we assume that the value $A_{\nu-1} B_\nu E(n_\mathrm{d}) - m\pi$ is negative. We obtain the following relation in the same way as in the positive case:

$$[E(n_\mathrm{d}) - A_\nu B_{\nu-1} E(n_\mathrm{d})] + m\pi \geq \Delta E, \tag{4.56}$$

which eventually leads to

$$E(n_\mathrm{d}) - \Delta E \geq \delta. \tag{4.57}$$

The energy of the new Dirac cone must be less than the energy cutoff ΔE: $E(n_{\rm d}) < \Delta E$. This leads to the relation $0 > \delta$. It also contradicts the condition $0 < \delta\,(< \Delta E)$ in Eq. (4.51). Therefore the inequalities (4.47) and (4.48) must hold for any index $n_{\rm d}$ in the first case $\Delta E \geq \pi$. In other words, the generation of the new Dirac cones are consecutive in the first case $\Delta E \geq \pi$.

Second we show that all new Dirac cones must be consecutive for $E(n_{\rm d}) < 2\Delta E - \pi$ in the second case $\pi/2 \leq \Delta E < \pi$. The overlap of the intervals whose centers are $(m-1)\pi$ and $m\pi$ is given by $2\Delta E - \pi$ (see Fig 4.14 (c)). When the energy of the new Dirac cones $E(n_{\rm d})$ is less than the overlap, all sets of the two points $A_{\nu-1}B_\nu E(n_{\rm d})$ and $A_\nu B_{\nu-1}E(n_{\rm d})$ must be located in a common interval $(m\pi - \Delta E, m\pi + \Delta E)$:

$$A_\nu B_{\nu-1}E(n_{\rm d}) - A_{\nu-1}B_\nu E(n_{\rm d}) = E(n_{\rm d}) < 2\Delta E - \pi. \tag{4.58}$$

However, there are sets of the two points which do not enter in a common interval when the energy satisfies the condition $E(n_{\rm d}) > 2\Delta E - \pi$. This fact indicates that a line $E = 2\Delta E - \pi$ separates the appearance of the new Dirac cones into the consecutive and sporadic cases.

Finally we show that the new Dirac points are not consecutive in the third case $\Delta E < \pi/2$ in Fig. 4.13. For the double-periodic potentials, the maximum values of the indices are approximated as $N_i \approx (L_i \Delta E)/\pi$ $(i = 1, 2)$. According to the generation rule (4.23), the maximum possible number of solutions is given by the total number of the combination of the indices n_1 and n_2,

$$2N_1 \times 2N_2 \approx 4L_1L_2\left(\frac{\Delta E}{\pi}\right)^2 = 4L\left(\frac{\Delta E}{\pi}\right)^2, \tag{4.59}$$

where the coefficients 2 reflect the fact that the new Dirac points appear in both the conduction and valence bands. We also used $L = L_1 \times L_2$. When the total number is less than the number of the new Dirac points in the single-periodic case $2N \approx (2L\Delta E)/\pi$, the appearance of the new Dirac points cannot be consecutive. The ratio between the two bands

$$\frac{2N_1 \times 2N_2}{2N} \approx 2\frac{\Delta E}{\pi} \tag{4.60}$$

is less than one, when the energy cutoff ΔE is less than $\pi/2$ in the third case. Therefore the appearance of the new Dirac point must not be consecutive but sporadic in the third case.

Chapter 5

Quasi-periodic potentials

5.1 Dense appearance of the new Dirac cones under the quasiperiodic potentials

We are now in a position to study the generation of the new Dirac cones under a quasiperiodic potential. We here study the quasiperiodic case by considering the limiting case of the double-periodic potential. As in Section 4.4, we assume for the sake of the argument that Eq. (4.23) can show the generation of the Dirac *cones* in quasiperiodic cases.

We have obtained a finite number of the new Dirac-electron structures for the double-periodic potentials. For quasiperiodic potentials, however, the appearance of the new cones is completely different. According to the generation rule (4.23), the index $n_{\rm d}$ of the new Dirac-electron structures in the double-periodic case is represented by the indices n_1 and n_2 for the single-periodic potentials. The number of the combination of the indices n_1 and n_2 is about $[(2\Delta EA_\nu)/\pi] \times [(2\Delta EB_\nu)/\pi]$. Thus the total number of the new Dirac cones tends to infinity in the quasiperiodic limit $\nu \to \infty$ with $A_\nu, B_\nu \to \infty$.

However, the appearance of the new cones is basically the same as shown in Fig. 4.13, except that the new cones appear densely in the energy range $|E| < \Delta E$. The three cases in Fig. 4.13 are now distinguished in terms of the density $\rho_{\rm Dirac}$ of the Dirac cones. Let us normalize the density of the new cones by the density in the case of a single sine function, namely L/π. We show in Fig. 5.1 the normalized density of the new cones for quasiperiodic potentials, with an example of $L_1 = 233$ and $L_2 = 144$, which emulate the

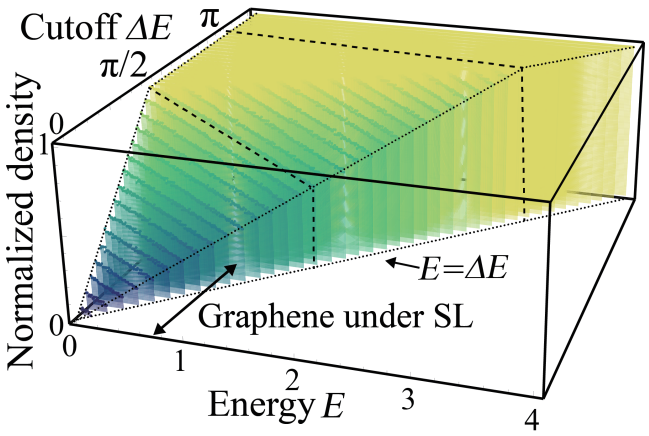

Figure 5.1: The normalized density ρ_{Dirac} for quasiperiodic potentials, with an example of $L_1/L_2 = 233/144$ as an approximation of the golden ratio $\left(1+\sqrt{5}\right)/2$. The two-dimensional plane represents the energy E and the energy cutoff ΔE. The dotted lines represent the general results derived from Eqs. (4.44) and (4.45). The broken lines represent the special cases $\Delta E = \pi/2$ and π.

golden ratio.

In the first case $\Delta E \geq \pi$, the normalized density is unity $\rho_{\mathrm{Dirac}} = 1$ in the whole range $|E| < \Delta E$. In the second case $\pi/2 \leq \Delta E < \pi$, the normalized density ρ_{Dirac} is also unity for the energy which satisfies the condition $|E| < 2\Delta E - \pi$. These two cases correspond to the area which has the consecutive Dirac cones in Fig. 4.13. In the remaining cases, namely the energy range $2\Delta E - \pi < |E| < \Delta E$ in the second case and the whole energy range in the third case $\Delta E < \pi/2$, the normalized density is less than unity.

5.2 Density of the new Dirac cones

We again consider the distance between the two points $A_{\nu-1}B_\nu E(n_{\mathrm{d}})$ and $A_\nu B_{\nu-1}E(n_{\mathrm{d}})$ on a line and assume $A_\nu B_{\nu-1} > A_{\nu-1}B_\nu$:

$$A_\nu B_{\nu-1}E(n_{\mathrm{d}}) - A_{\nu-1}B_\nu E(n_{\mathrm{d}}) = E(n_{\mathrm{d}}). \tag{5.1}$$

In the quasiperiodic limit, the infinite number of points are distributed homogeneously in the range π. We note that the following arguments can be

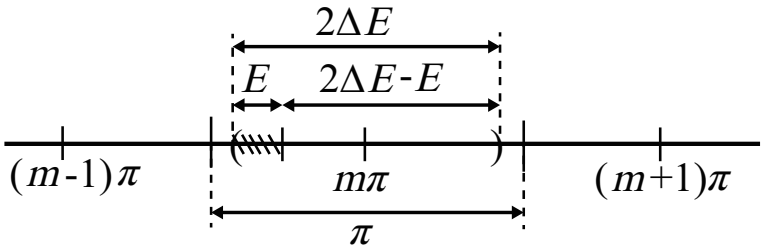

Figure 5.2: The condition of generating the new Dirac cones in the third case. When the energy E is available in the hatched area, the new Dirac cones never appear.

applied to the case $A_\nu B_{\nu-1} < A_{\nu-1}B_\nu$ by replacing the symbols.

We first consider the third case $\Delta E < \pi/2$. The equations (4.47) and (4.48) tells us that both two points $A_{\nu-1}B_\nu E(n_{\rm d})$ and $A_\nu B_{\nu-1}E(n_{\rm d})$ must be located in a range $(m\pi - \Delta E, m\pi + \Delta E)$ in order to generate the new Dirac cone indexed as $n_{\rm d}$. When the point $A_\nu B_{\nu-1}E(n_{\rm d})$ is set in the hatched area in Fig. 5.2, the other point $A_{\nu-1}B_\nu E(n_{\rm d}) = A_\nu B_{\nu-1}E(n_{\rm d}) - E(n_{\rm d})$ cannot be located in the hatched area, and hence we do not have the new Dirac cone indexed as $n_{\rm d}$.

We can employ this argument to compute the density of the new Dirac cones. In the quasiperiodic limit, the infinite number of points $A_\nu B_{\nu-1}E(n_{\rm d})$ are located on a line. Let us fold the points on to the corresponding locations in an interval with the range π (see Fig. 5.3 (a)). According to the above argument, the points $\{A_\nu B_{\nu-1}E(n_{\rm d})\}$ located in the hatched area do not generate the new Dirac cones (see Fig. 5.3 (b)). The probability that the homogeneously distributed points are not located in the hatched area is given by

$$\frac{2\Delta E - (\text{the hatched area})}{\pi}, \tag{5.2}$$

which gives the normalized density $\rho_{\rm Dirac}$. Therefore the normalized density in the third case is represented by

$$\rho_{\rm Dirac} = \frac{2\Delta E - E}{\pi} = -\frac{1}{\pi}E + 2\frac{\Delta E}{\pi}. \tag{5.3}$$

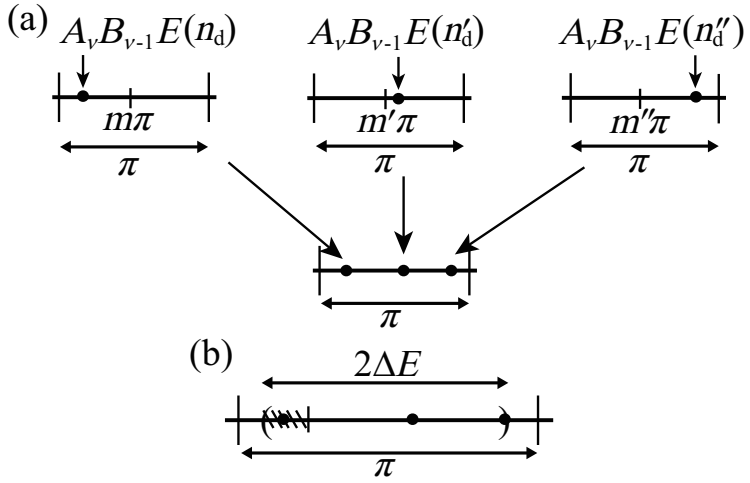

Figure 5.3: **(a)** Folding the points $\{A_\nu B_{\nu-1} E(n_\mathrm{d})\}$ in different intervals to the same interval with the range π. **(b)** The condition of generating the new Dirac cones in the third case.

Table 5.1: The series of the approximated values A_ν/B_ν of the golden ratio $(1+\sqrt{5})/2$.

ν	4	5	6	7	8	9	10	11	12	13
A_ν	8	13	21	34	55	89	144	233	377	610
B_ν	5	8	13	21	34	55	89	144	233	377

5.3 Fractal analysis of the new Dirac cones

Generally speaking, quasiperiodic quantum systems are believed to have fractal structures in the energy spectrum [64–66]. Previous works have confirmed it for the systems governed by the Schrödinger equation. In this section, we claim that we do not see any fractal features in the appearance of the Dirac cones under quasiperiodic potentials. The difference may be due to the difference in the dispersion relation. The Schrödinger equation usually has a quadratic dispersion in the energy spectrum, whereas the dispersion of the Dirac Hamiltonian is linear.

We carry out a multifractal analysis of the intervals between the indices $n_{\rm d}$ of the new Dirac cones in the numerical calculations (see Appendix D) [84, 85]. We used the generation rule (4.23) in order to obtain the series of the indices of the new Dirac cones. The indices n_1 and n_2 are given by $n_i = 0, \pm 1, \pm 2, \ldots, \pm N_i$, where $N_i \simeq \lfloor L_i \Delta E/\pi \rfloor$ $(i = 1, 2)$. We thus obtain the series of the indices $n_{\rm d}$ for the double-periodic potentials as the combination of the indices n_1 and n_2 through Eq. (4.23).

We here regard the series of the new Dirac points as a point sequence and carried out the multifractal analysis for the intervals of the sporadic new Dirac cones in the second case $\pi/2 \leq \Delta E < \pi$ and the third case $\Delta E < \pi/2$. The first case $\Delta E \geq \pi$ cannot show a fractal structure because the Dirac cones appear consecutively.

Figures 5.4 and 5.5 show the multifractal spectra of the intervals of the new Dirac points in the second case $\Delta E = 2.2$ and the third case $\Delta E = 1.0$, respectively. We used the series of the rational numbers A_ν/B_ν which converges to the golden ratio $(1+\sqrt{5})/2$ (see Table 5.1). We skip the sets $A_1/B_1 = 2/1$, $A_2/B_2 = 3/2$, and $A_3/B_3 = 5/3$ because the numerical diagonalization showed that graphene under a double-periodic potential with these periods never generate the new Dirac cones because of short periods.

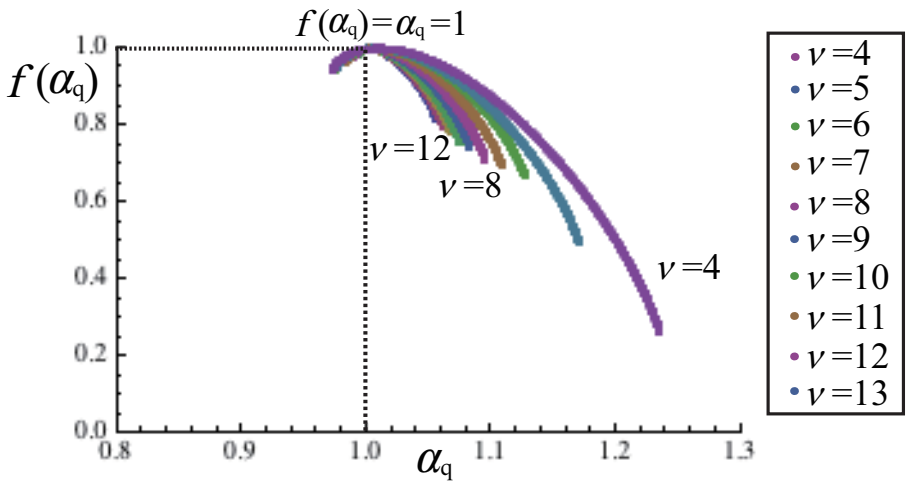

Figure 5.4: A multifractal analysis of the intervals of the new Dirac cones for the energy cutoff $\Delta E = 2.2$, which corresponds to the second case $\pi/2 \leq \Delta E < \pi$. The spectra show the results for the rational numbers $\nu = 4, \ldots, 13$ which approximate the golden ratio. The broken line represents $f(\alpha_q) = \alpha_q = 1$.

The multifractal spectrum in the second case $\Delta E = 2.2$ show a smooth curve (see Fig. 5.4). The tops of the spectra are close to the dimension $f(\alpha_q) = \alpha_q = 1$. Analyses for other values of the cutoff in the second case show similar spectra. The multifractal spectrum in the third case $\Delta E = 1.0$ also shows a smooth curve (see Fig. 5.5).

The curves in Figs. 5.4 and 5.5 seem to converge asymptotically. Thus we focus on the minimum and maximum values of the singularity index α_q. The minimum and maximum values α_∞ and $\alpha_{-\infty}$ are obtained in the limits $q \to \infty$ and $q \to -\infty$, respectively. The difference of the values α_∞ and $\alpha_{-\infty}$ represents the range of the singular indices α_q of the multifractal spectrum. In order to study the multifractal spectrum in the quasiperiodic limit, we study the series of the minimum and maximum values $\alpha_\infty(\nu)$ and $\alpha_{-\infty}(\nu)$ as the order of the expansion ν increases. In our numerical calculation, we estimate the minimum and maximum values α_∞ and $\alpha_{-\infty}$ by using large positive and negative values q.

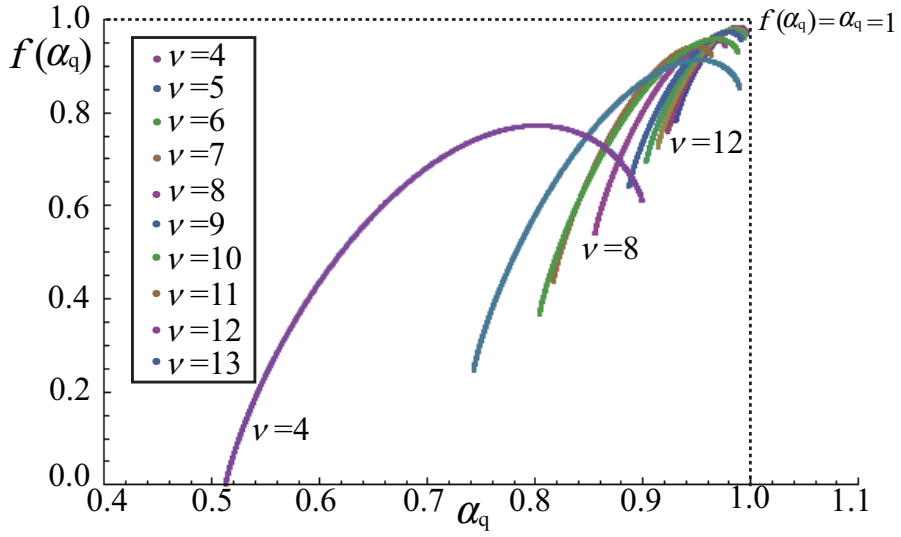

Figure 5.5: A multifractal analysis of the intervals of the new Dirac cones for the energy cutoff $\Delta E = 1.0$, which corresponds to the third case $\Delta E < \pi/2$. The spectra show the results for the rational numbers $\nu = 4, \ldots, 13$ which approximate the golden ratio. The broken line represents $f(\alpha_q) = \alpha_q = 1$.

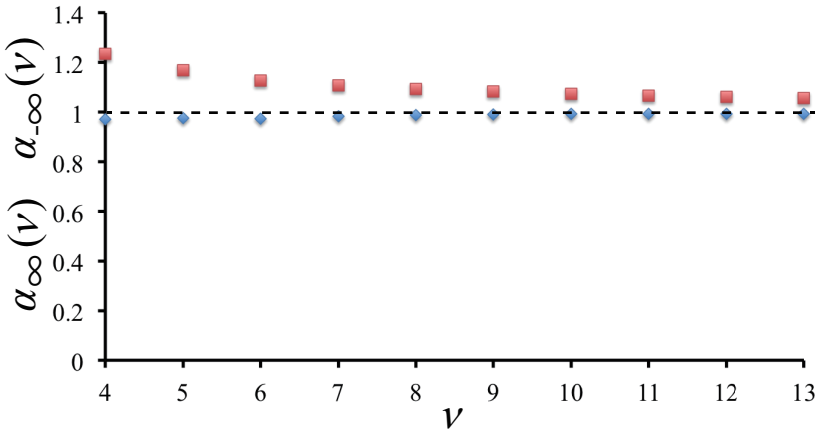

Figure 5.6: Changes of the minimum and maximum values of the singular index α_∞ and $\alpha_{-\infty}$ as the increase of the order of the expansion ν for the energy cutoff $\Delta E = 2.2$. The blue diamonds and red squares represent the numerical results for the minimum and maximum values α_∞ and $\alpha_{-\infty}$, respectively. The broken line represents $\alpha(\nu) = 1$.

We first show the numerical results for the second case $\Delta E = 2.2$ in Fig. 5.6. Figure 5.6 shows that the minimum and maximum values of the singular index seem to converge to unity as the order of the expansion ν increases. We estimate the limiting values by fitting the data to the function ν^{-x}, where x is a positive integer. For the energy cutoff $\Delta E = 2.2$, the estimation shows that $\alpha_\infty(\nu) \to 1.005$ (Fig. 5.7 (a)) and $\alpha_{-\infty}(\nu) \to 1.042$ (Fig. 5.7 (b)) by using ν^{-1} and ν^{-2}, respectively. The both estimates converge to unity, which is the dimension of a line. Hence we can conclude that the generation of the new Dirac cones is not multifractal in the second case $\pi/2 \leq \Delta E < \pi$.

Figure 5.8 is a numerical result for the energy cutoff $\Delta E = 1.0$. The estimation shows that $\alpha_\infty(\nu) \to 0.9256$ (Fig. 5.9 (a)) and $\alpha_{-\infty}(\nu) \to 1.007$ (Fig. 5.9 (b)) by using ν^{-3} and ν^{-2}, respectively. Both estimates for the energy cutoff $\Delta E = 1.0$ show that the singularity indices α_∞ and $\alpha_{-\infty}$ are in the range $(0.9, 1.0)$. Thus the singularity indices tend to converge to values close to unity.

We finally conclude that the the intervals of the new Dirac cones are not fractal in the quasiperiodic limit, because the estimated values are very close

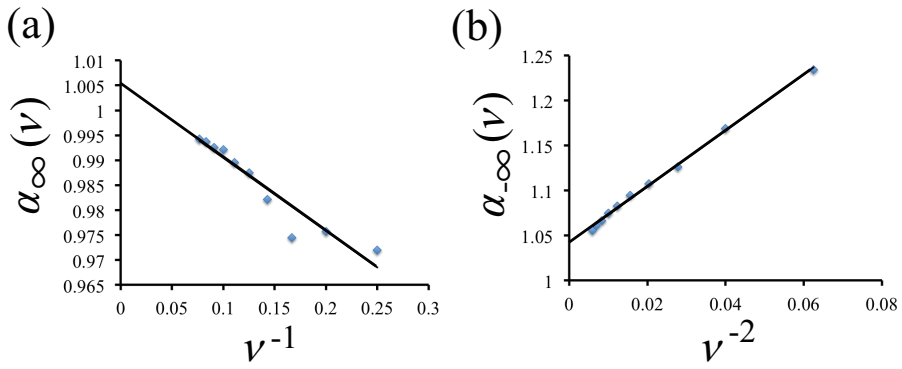

Figure 5.7: Estimation of the limiting values by fitting the data to the function ν^{-x} for the energy cutoff $\Delta E = 2.2$. **(a)** The minimum value α_∞ by fitting the data to the function ν^{-1}. **(b)** The maximum value $\alpha_{-\infty}$ by fitting the data to the function ν^{-2}. In both figures, the solid lines represent the fitting lines

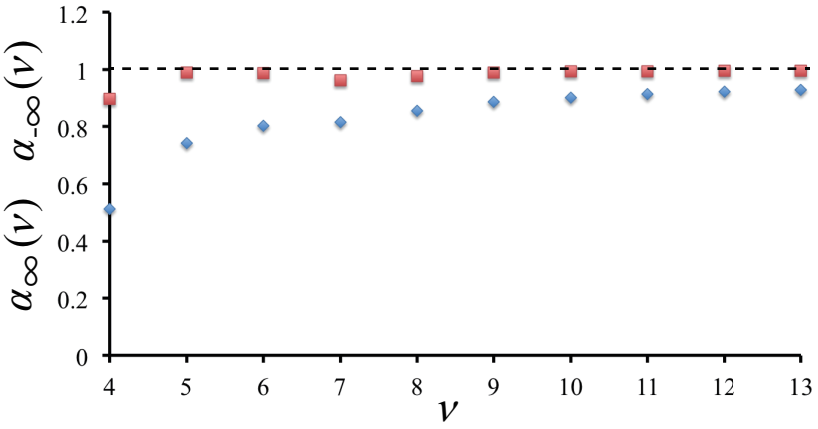

Figure 5.8: Changes of the minimum and maximum values of the singular index α_∞ and $\alpha_{-\infty}$ as the increase of the order of the expansion ν for the energy cutoff $\Delta E = 1.0$. The blue diamonds and red squares represent the numerical results for the minimum and maximum values α_∞ and $\alpha_{-\infty}$, respectively. The broken line represents $\alpha(\nu) = 1$.

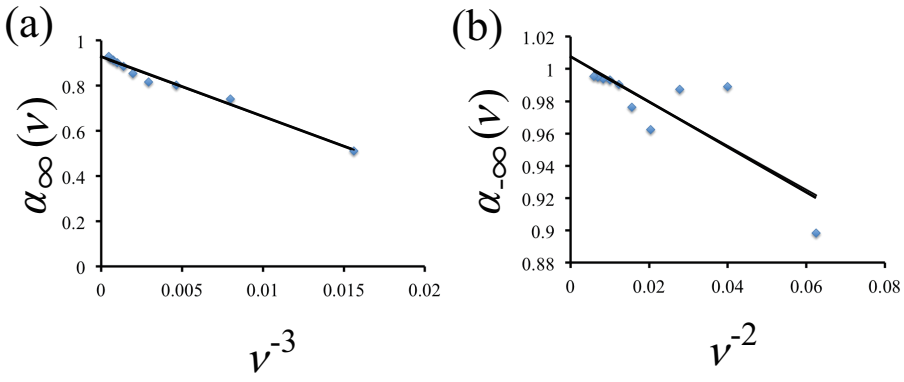

Figure 5.9: Estimation of the limiting values by fitting the data to the function ν^{-x} for the energy cutoff $\Delta E = 1.0$. **(a)** The minimum value α_{∞} by fitting the data to the function ν^{-3}. **(b)** The maximum value $\alpha_{-\infty}$ by fitting the data to the function ν^{-2}. In both figures, the solid lines represent the fitting lines

to unity.

Chapter 6

Summary and discussion

In this thesis we have investigated the generation of the new Dirac-electron structures induced by single-periodic, double-periodic, and quasiperiodic potentials. We confirmed our prediction by numerical results of the tight-binding model under the *superlattice* potentials.

In Chapter 2, we first reviewed the theoretical treatments of graphene by using the tight-binding model on the honeycomb lattice. We reviewed that the conical dispersions, namely the Dirac cones, appear at the boundaries of the hexagonal Brillouin zone, the K and K' points. We next defined a quasiperiodic function as the summation of two sine functions with an irrational number as the ratio of the periods. If the ratio of the periods of two sine functions is a rational number, we call the sum of them *double-periodic*. We can regard the double-periodic function as an approximation of the quasiperiodic function because an irrational number is approximated by a rational number. We used the relation to treat the generation of the new Dirac cones under quasiperiodic superlattice potentials. At the end of this chapter, we studied the tight-binding model on the honeycomb lattice under periodic superlattice potentials. The wave-vector representation of the Hamiltonian in the deformed Brillouin zone is the basis of the numerical analyses.

In Chapter 3, we first reviewed the generation of the new Dirac cones in the Dirac Hamiltonian under the single-periodic superlattice potential. The energies of the new Dirac cones are inversely proportional to the period of the superlattice. The cones appear at one half of the reciprocal lattice vector of the superlattice. The generation is indexed by consecutive integers, $n = 0, \pm 1, \pm 2, \ldots$. Note that there is no maximum value for the integers in

the previous studies [52, 53].

We then numerically confirmed the generation of the new Dirac-electron structures under the one-dimensional single-periodic superlattice potential by using the tight-binding approximation. As we increase the system size we found two different trends of the energy intervals. The first one is that the energy intervals show visibly large gaps as the system size increase. The second one is that the energy intervals continue decreasing as we increase the size. In the second case, we cannot tell whether the energy gaps of the band contacts are truly zero or not by our numerical results of the tight bonding model of finite sizes. Strictly speaking, superlattice potentials may not produce the truly gapless Dirac cones in contradiction to the reports of the previous theoretical and experimental studies [26, 27, 31, 52, 53]. From our numerical results, we nonetheless practically regard the structure as a Dirac cone because the energy gaps, if any, are invisibly small. We call them *Dirac-electron structures* in this thesis. As we increase the amplitudes of the potentials, the energy gaps remain very small below critical or crossover values, beyond which visible gaps develop. Graphene on superlattice substrates with enough weak interlayer couplings may create the Dirac-electron structures. The present numerical results showed that the energy gaps are at least 10^{-6} times smaller than the hopping element. Therefore, experimental $\mathrm{d}I/\mathrm{d}V$ curves obtained by scanning tunneling microscope may show sharp dips for the new Dirac-electron structures. If we increase the interlayer couplings, the curve may show plateaus as the reflection of the Dirac-electron structures with visibly large energy gaps.

We numerically found the maximum value of the index of the new Dirac-electron structures. As we increase the amplitude, the maximum value decreases although we fixed the period. We defined the energy cutoff $\Delta E(v)$ for a large amplitude v as the minimum energy of the disappeared structures.

We found that the new Dirac-electron structures become anisotropic with increasing distance from the Fermi energy. In addition, the change of the amplitude also affected the positions of the Dirac-electron structures. They moved linearly passing though the positions which are predicted by the Dirac Hamiltonian. As a result, two Dirac-electron structures, excepting the case $L = 2$, disappear without merging with each other. We thus concluded that the Dirac-electron structures without merging may not be the gapless Dirac cones, because all the Dirac cones exhibited merging before the annihilation in the previous studies [55–58]. We showed the numerical results for different periods, which are the basis in the double-periodic cases.

In Chapter 4, we first investigated the generation of the new Dirac-electron structures in the double-periodic case in terms of the Dirac Hamiltonian with a superlattice potential. The most different point is that the generation of the new Dirac-electron structures is not consecutive although the double-periodic potential is a periodic function. We found that the generation is described by the the Diophantine equation. It showed that the index of the new structures for the double-periodic potentials is represented by the combination of the indices for the single-periodic potentials. We then studied the generation in the double-periodic case by the numerical diagonalization of the tight-binding model. Note that we confirmed the generation by the same judgment rule which we used for the single-periodic potentials.

The appearance was indeed different from the single-periodic cases, which we call *sporadic*. The difference also appears in the anisotropy of the new cones. As the index becomes larger, the anisotropy changed seemingly randomly while the one for single-periodic potential monotonically decreases. The generation rule well explained the difference. This is also a piece of evidence that the Dirac-electron structures have at most invisibly small energy gaps for small amplitudes of the potentials. As we increase the amplitude, we empirically found that the lower one of the energy cutoffs controls the generation. Though we increased just an amplitude, the ranges of both indices which affect the generation decreased.

We next extended our argument to general Dirac electron systems, assuming that the generation rule governs the appearance of the Dirac cones. We here distinguish the Dirac electron systems in terms of the value of the energy cutoff ΔE. We have found that the generation is classified into three cases according to the energy cutoff. In the first case $\Delta E \geq \pi$, all new Dirac cones are consecutive though we add a double-periodic potential. In the second case $\pi/2 \leq \Delta E < \pi$, we found two regions of consecutive and sporadic generations. In the third case $\Delta E < \pi/2$, the generation is always sporadic; graphene under superlattice potentials belong to this case. We analytically proved the existence of the three cases.

In Chapter 5, we studied the generation of the new Dirac cones induced by the quasiperiodic potentials. We first revealed that the new Dirac cones appear densely in the quasiperiodic limit. We introduced the density of the Dirac cones in order to understand the difference. We found that the generation is also classified into the three cases for the quasiperiodic potentials. The most significant difference between the periodic systems (including double-periodic systems) and the quasiperiodic systems is the interval of the Dirac

cones. The original Dirac cone [6] and the new cones generated by periodic potentials have zero measure because they have finite intervals. However, the new Dirac cones generated by quasiperiodic potentials have a finite measure because they appear densely without intervals. It may make the nature of the Dirac cones robust against a thermal excitation and an infinitesimal doping. This essential difference can affect the dc conductivity [32] and transmission [62].

We next showed the multifractal analyses of the intervals of the new Dirac points under the quasiperiodic potentials. The previous works [64–66] reported that the energy spectra are fractal for quantum systems with quasiperiodic arrangements. In order to analyze the fractality of the spectrum of Dirac electron systems under the quasiperiodic potentials, we studied the multifractal spectra of the intervals of the new Dirac cones. In the quasiperiodic limit the results showed that the dimension of the interval tends to converge to unity. This is clearly different from the well-known example, namely the Cantor set whose dimension is $\log 2/\log 3 = 0.63\ldots$. We therefore conclude that the intervals of the new Dirac cones are not fractal. On the other hand, previous studies reported the self-similarity in graphene with Fibonacci arrangement [37, 62, 63]. Our result suggests that the self-similar growth of the Fibonacci superlattice causes the difference. We may distinguish the difference between the quasiperiodicity and the fractality in the studies of graphene and general Dirac electron systems under the superlattice potentials.

The non-fractal generation of the new Dirac cones may make us reconsider the concepts of the quasiperiodic system. Our results of the energy cutoff $\Delta E \geq \pi$ show that the quasiperiodic potentials never generate the new Dirac cones with fractal arrangements. It indicates that the well-known relation between the quasiperiodic systems and the fractal spectra only hold in the case of the quadratic dispersion. It is important from the viewpoint of understanding the fractal nature of the quantum mechanics.

It is also important to note that the fractal aspects in quantum mechanics mostly appear in the one-electron problem. The studies of fractals in physics have mainly targeted classical systems; fractals have been found mostly in stochastic phenomena, for example the growth of DLA (diffusion limited aggregation) clusters, the shape of coasts, viscous fingering, and so on [84,85]. Fractals in quantum systems, on the other hands, do not need a particle-particle interactions but spatial arrangements *i.e.* quasiperiodicity. The difference in the condition of the appearance may be intrinsic in the fractality

of quantum systems. We need to investigate the point as a future work.

In this study, we have mainly focused on the conditions of that the energy gaps stay invisibly small. From the point of view of the application of graphene, however, producing *large* energy gaps gathers more attention. Controlling the coupling or the amplitudes of the substrate can be a way to make the graphene-based semi conductor. In the low-energy ranges, making large energy gaps is helped by the double-periodic potentials. If we set appropriate periods, we can produce the lowest gapful structure $n = 1$. The shape of the superlattice is important not only to realize the fundamental nature of graphene superlattice but also to promote the graphene-based technology. Graphene on two hexagonal boron-nitride monolayers with different rotation angles can generate double-periodic moiré patterns and may show dips at the points given by Eq. (4.23).

Acknowledgements

It is great pleasure to express my sincere gratitude to my supervisor Dr. Naomichi Hatano. He gave me continuous supports and fruitful advises since I have first met him as a master course student in other laboratory. His advises always guided my research in a new direction. I thank to Dr. Jun Goryo for useful discussions. I am indebted to Dr. Kenichiro Imura and Dr. Tomoki Machida for helpful information on this work.

I was financially supported by Global Center of Excellence for Physical Sciences Frontier, The University of Tokyo.

Finally I would like to express my gratitude to my family for their supports.

Tokyo, July 2015. *Masayuki Tashima*

Appendix A

Continued fraction expansion

All real numbers are classified into two types, the rational number and the irrational number. We here review the formalism of the continued fraction expansions of the rational and irrational numbers and show the relations between the expansions.

A.1 Rational number

Any rational number r_n can be expressed by two types of the finite simple continued fraction expansion [81, 86]:

$$r_n = b_0 + \cfrac{1}{b_1 + \cfrac{1}{b_2 + \cdots \cfrac{1}{b_{n-1} + \cfrac{1}{b_n}}}} \tag{A.1}$$

and

$$r_n = b_0 + \cfrac{1}{b_1 + \cfrac{1}{b_2 + \cdots \cfrac{1}{b_{n-1} + \cfrac{1}{(b_n - 1) + \cfrac{1}{1}}}}}, \tag{A.2}$$

where b_0 is an integer and b_n ($n \geq 1$) are positive integers. They are sometimes represented in the following forms for brevity:

$$r_n = \frac{A_n}{B_n} = [b_0; b_1, b_2, \cdots, b_{n-1}, b_n] \tag{A.3}$$

and

$$\begin{aligned} r_n = r'_{n+1} = \frac{A'_{n+1}}{B'_{n+1}} &= [b'_0; b'_1, b'_2, \cdots, b'_{n-1}, b'_n, b'_{n+1}] \\ &= [b_0; b_1, b_2, \cdots, b_{n-1}, (b_n - 1), 1], \end{aligned} \tag{A.4}$$

where A_n and B_n are integers coprime to each other, A'_{n+1} and B'_{n+1} are too, and we used the prime to distinguish the two expansions.

A.2 Irrational number

Any irrational number r_∞ can be expressed by only one type of the infinite simple continued fraction expansion:

$$r_\infty = b_0 + \cfrac{1}{b_1 + \cfrac{1}{b_2 + \cdots \cfrac{1}{b_{n-1} + \cfrac{1}{b_n + \cdots}}}}, \tag{A.5}$$

or by the corresponding compact form:

$$r_\infty = [b_0; b_1, b_2, \cdots, b_{n-1}, b_n, \cdots]. \tag{A.6}$$

An irrational number r_∞ can be approximated by a series of rational numbers $\{r_n\} = \{r_0, r_1, r_2, \ldots, r_n, \ldots\}$ given in the compact forms

$$r_0 = \frac{A_0}{B_0} = [b_0], \tag{A.7}$$

$$r_1 = \frac{A_1}{B_1} = [b_0; b_1], \tag{A.8}$$

$$r_2 = \frac{A_2}{B_2} = [b_0; b_1, b_2], \tag{A.9}$$

$$r_n = \frac{A_n}{B_n} = [b_0; b_1, b_2, \cdots, b_n], \tag{A.10}$$

where A_n and B_n are both integers coprime to each other.

The numerators $\{A_n\}$ and denominators $\{B_n\}$ given by the infinite simple continued expansion (A.10) satisfy the following recurrence formulas [81]

$$A_n = b_n A_{n-1} + A_{n-2} \tag{A.11}$$

and

$$B_n = b_n B_{n-1} + B_{n-2} \tag{A.12}$$

for $n \geq 1$, where $A_{-1} = 1$, $A_0 = b_0$, $B_{-1} = 0$, and $B_0 = 1$.

A.3 A relation between numerators and denominators

The numerators $\{A_n\}$ and denominators $\{B_n\}$ satify a simple relation

$$A_n B_{n-1} - A_{n-1} B_n = (-1)^{n-1}. \tag{A.13}$$

We show the above relation by using the recurrence formulas (A.11) and (A.12).

We rewrite the left-hand side of Eq. (A.13) by using the recurrence formulas (A.11) and (A.12) as follows:

$$\begin{aligned} & A_n B_{n-1} - A_{n-1} B_n \\ & = (b_n A_{n-1} + A_{n-2}) B_{n-1} - A_{n-1}(b_n B_{n-1} + B_{n-2}) \\ & = A_{n-2} B_{n-1} - A_{n-1} B_{n-2}. \end{aligned} \tag{A.14}$$

The relation $A_{n-2} B_{n-1} - A_{n-1} B_{n-2}$ is of the same form as in the left-hand side of Eq. (A.13) after replacing $A_n \to A_{n-2}$ and $B_n \to B_{n-2}$. We repeat rewriting the relation and obtain

$$\begin{aligned} & A_n B_{n-1} - A_{n-1} B_n \\ & = A_{n-2} B_{n-1} - A_{n-1} B_{n-2} \\ & = A_{n-2}(b_{n-1} B_{n-2} + B_{n-3}) - (b_{n-1} A_{n-2} + A_{n-3}) B_{n-2} \\ & = A_{n-2} B_{n-3} - A_{n-3} B_{n-2} \\ & = A_{n-4} B_{n-3} - A_{n-3} B_{n-4} \\ & = A_{n-4} B_{n-5} - A_{n-5} B_{n-4} = \cdots . \end{aligned} \tag{A.15}$$

When the degree of the expansion n is an even number, the rewriting stops as

$$A_n B_{n-1} - A_{n-1} B_n = \cdots = A_0 B_{-1} - A_{-1} B_0 = -1 = (-1)^{n-1}, \tag{A.16}$$

while for odd n, it stops as

$$A_n B_{n-1} - A_{n-1} B_n = \cdots = A_{-1} B_0 - A_0 B_{-1} = +1 = (-1)^{n-1}. \tag{A.17}$$

We thereby obtain the relation (A.13).

A.4 A relation between different expansions of a rational number

A rational number r_n has the two types of the expansion (A.3) and (A.4). We here show that the numerators and denominators in the two types of the expansion satisy a relation.

We first show a relation among the numerators and the denominators before going to the final relation. Let us consider the two expansions of a rational number $r_n = r'_{n+1}$ in Eqs. (A.3) and (A.4) Since the two expressions reduce to the some rational number, the numerators and the denominators must be the same:

$$A_n = A'_{n+1}, \quad B_n = B'_{n+1}. \tag{A.18}$$

On the other hand, the above relation never holds for $m < n$. Let us consider the case $m = n - 1$ for example. The two expansions

$$r_m = r_{n-1} = \frac{A_{n-1}}{B_{n-1}} = [b_0; b_1, b_2, \cdots, b_{n-1}] \tag{A.19}$$

and

$$\begin{aligned} r'_{m+1} = r'_n = \frac{A'_n}{B'_n} &= [b'_0; b'_1, b'_2, \cdots, b'_{n-1}, b'_n] \\ &= [b_0; b_1, b_2, \cdots, b_{n-1}, (b_n - 1)]. \end{aligned} \tag{A.20}$$

produce different rational numbrs, $r_m \neq r'_{m+1}$, and hence $A_m \neq A'_{m+1}$ and $B_m \neq B'_{m+1}$.

In order to find out relations between the numerators and denominators in the case $m < n$, we use the following expansion another rational number:

$$\begin{aligned} r'_{n-1} = \frac{A'_{n-1}}{B'_{n-1}} &= [b'_0; b'_1, b'_2, \cdots, b'_{n-1}] \\ &= [b_0; b_1, b_2, \cdots, b_{n-1}] = \frac{A_{n-1}}{B_{n-1}}. \end{aligned} \tag{A.21}$$

These expansions yield the following relations for $m < n$:

$$A_m = A'_m, \quad B_m = B'_m. \tag{A.22}$$

Now we can show a relation between the two types of the expansion. The numerators A_{n-1} and A'_n have the following relation:

$$\begin{aligned} A_{n-1} + A'_n &= A_{n-1} + \left[(b_n - 1)A'_{n-1} + A'_{n-2}\right] \\ &= A_{n-1} + [(b_n - 1)A_{n-1} + A_{n-2}] \\ &= b_n A_{n-1} + A_{n-2} = A_n, \end{aligned} \tag{A.23}$$

where we used the recurrence relation (A.11) and the relation (A.22). The denominators B_{n-1} and B'_n also have a similar relation. We finally obtain the following relations between the two types of the expansion:

$$A_{n-1} + A'_n = A_n, \quad B_{n-1} + B'_n = B_n. \tag{A.24}$$

A.5 Proof of the equivalence of inequalities for two kinds of expansions

The Euclidean algorithm [86] casts any rational number into two types of the expansion (A.3) and (A.4). We here show that the two forms of the expansion lead to the same set of inequalities. The second of the expansion yield the following inequalities:

$$\left| \frac{A'_\nu}{A'_{\nu+1}} n_{\rm d} - m' \right| \leq \frac{N_1}{A'_{\nu+1}} \tag{A.25}$$

and

$$\left| \frac{B'_\nu}{B'_{\nu+1}} n_{\rm d} - m' \right| \leq \frac{N_2}{B'_{\nu+1}} \tag{A.26}$$

instead of Eqs. (4.44) and (4.45). In order to show that the inequalities (A.25) and (4.44) are equivalent to each other, we rewrite Eq. (A.25) by using the replacement (A.18) and (A.24):

$$\begin{aligned} \left| \frac{A'_\nu}{A'_{\nu+1}} n_{\rm d} - m' \right| &= \left| \frac{(A_\nu - A_{\nu-1})}{A_\nu} n_{\rm d} - m' \right| \\ &= \left| \frac{A_{\nu-1}}{A_\nu} n_{\rm d} - (n_{\rm d} - m') \right|. \end{aligned} \tag{A.27}$$

Replacing the integer $n_{\rm d} - m'$ with m, We obtain

$$\left| \frac{A'_\nu}{A'_{\nu+1}} n_{\rm d} - m' \right| = \left| \frac{A_{\nu-1}}{A_\nu} n_{\rm d} - m \right|. \tag{A.28}$$

The right-hand sides of the inequalities (A.25) and (4.44) are also equal to each other:

$$\frac{N_1}{A'_{\nu+1}} = \frac{N_1}{A_\nu}. \tag{A.29}$$

Therefore the two inequalities (A.25) and (4.44) are equivalent. The same argument shows that the relation also holds for (A.26) and (4.45).

Appendix B

The K and K' points in the first supercell Brillouin zone

The positions of the K and K' points in the first Brillouin zone of the hexagonal lattice system are represented by the reciprocal vectors $\vec{b}_1$ and $\vec{b}_2$:

$$\vec{K} = \frac{2}{3}\vec{b}_1 + \frac{1}{3}\vec{b}_2 \tag{B.1}$$

and

$$\vec{K'} = \frac{1}{3}\vec{b}_1 + \frac{2}{3}\vec{b}_2. \tag{B.2}$$

When we apply a one-dimensional periodic superlattice potential with the period L along the $\vec{a}_1$ direction, the first supercell Brillouin zone is reduced to $(1/L)\vec{b}_1 \times \vec{b}_2$. The positions of K and K' points in the first supercell Brillouin zone is represented as

$$\vec{K} = K_1\left(\frac{\vec{b}_1}{L}\right) + K_2\vec{b}_2 \tag{B.3}$$

and

$$\vec{K'} = K'_1\left(\frac{\vec{b}_1}{L}\right) + K'_2\vec{b}_2, \tag{B.4}$$

where the coefficients are real number whose absolute values are less than one. If we consider the band folding, the coefficients K_2 and K'_2 do not change: $K_2 = 1/3$ and $K'_2 = 2/3$, while the other coefficients must satisfy the following relations:

$$0 \leq K_1 = \frac{2}{3}L - l_1 < 1 \tag{B.5}$$

and

$$0 \leq K_1' = \frac{1}{3}L - l_1' < 1, \tag{B.6}$$

where l_1 and l_1' are integers.

We next show that the coefficients K_1 and K_1' only have three cases depending on the period L. We firstly study the case $L = 3 \times m$, where m is an integer. In this case, we can rewrite the relations (B.5) and (B.6) to

$$0 \leq 2m - l_1 < 1 \tag{B.7}$$

and

$$0 \leq m - l_1' < 1. \tag{B.8}$$

We thus obtain the coefficients $K_1 = 0$ and $K_1' = 0$ for $l_1 = 2m$ and $l_1' = m$, respectively, as the only possibility. We next study the case $L = 3 \times m + 2$. This time we obtain the following relations:

$$0 \leq 2m + \frac{4}{3} - l_1 < 1 \tag{B.9}$$

and

$$0 \leq m + \frac{2}{3} - l_1' < 1. \tag{B.10}$$

The coefficients are $K_1 = 1/3$ and $K_1' = 2/3$ for $l_1 = 2m + 1$ and $l_1' = m$, respectively. Using the same arguments, we obtain the last relations for $L = 3m + 1$:

$$0 \leq 2m + \frac{2}{3} - l_1 < 1 \tag{B.11}$$

and

$$0 \leq m + \frac{1}{3} - l_1' < 1. \tag{B.12}$$

The coefficients are $K_1 = 2/3$ and $K_1' = 1/3$ for $l_1 = 2m$ and $l_1' = m$, respectively.

Appendix C

The two Dirac points for the single-periodic case $L = 2$

We here consider the case of the single-periodic potential with $L = 2$. The matrix elements are given by Eqs. (2.41) and (2.42). We here use the cosine potential because the sine function is not appropriate to study the effect of the amplitude in the case of $L = 2$.

For $L = 2$, a reciorocal vector $\vec{k}$ is represented by

$$\vec{k} = k_1\vec{b}_1 + k_2\vec{b}_2, \tag{C.1}$$

where k_1 and k_2 are real, while $\vec{b}_1$ and $\vec{b}_2$ are given by Eqs. (2.3) and (2.4). We analytically obtain the eigenenergy in the forms

$$\begin{aligned} E_{1,\pm} = \pm\Big(3 + v^2 + 2\cos(2k_2\pi) - \sqrt{2}\big\{ \cos(4k_1\pi) + \cos[4(k_1 - k_2)\pi] \\ + (4 + 8v^2)\cos^2(k_2\pi) + 2\cos[(4k_1 - 2k_2)\pi]\big\}^{1/2}\Big)^{1/2} \end{aligned} \tag{C.2}$$

and

$$\begin{aligned} E_{2,\pm} = \pm\Big(3 + v^2 + 2\cos(2k_2\pi) + \sqrt{2}\big\{ \cos(4k_1\pi) + \cos[4(k_1 - k_2)\pi] \\ + (4 + 8v^2)\cos^2(k_2\pi) + 2\cos[(4k_1 - 2k_2)\pi]\big\}^{1/2}\Big)^{1/2}. \end{aligned} \tag{C.3}$$

The energy bands $E_{1,\pm}$ may touch each other at the Fermi energy. Let us find where they do so. We assume that the locations of the touching points

are perpendicular to the reciprocal lattice vector of the external potential. We therefore represent the touching point around the K point as

$$\vec{K} + \alpha\left(\frac{1}{2}\vec{b}_1 + \vec{b}_2\right) = \left(\frac{1}{6} + \frac{\alpha}{2}\right)\vec{b}_1 + \left(\frac{1}{3} + \alpha\right)\vec{b}_2, \tag{C.4}$$

where a real number α denotes the distance from the K point solving the equation $E_{1,\pm} = 0$ for $k_1 = (1/6 + \alpha/2)$ and $k_2 = (1/3 + \alpha)$, we obtain the relation between the distance α and the amplitude of the potential v in the form

$$\alpha = \frac{1}{2\pi}\arccos\left(\frac{v^2 - 1}{2}\right) - \frac{1}{3}. \tag{C.5}$$

When the amplitude v is zero, the energy spectrum is gapless just at K point ($\alpha = 0$). The relation holds until the amplitude v is equal to or less than $\sqrt{3}$. When $v = \sqrt{3}$, the gapless point is located at the origin ($\alpha = -1/3$).

We can obtain the touching point around the K' point by the same argument. The K' point in Fig. 3.25 is represented as follows:

$$\vec{K}' = \left(\frac{2}{3} - 1\right)\frac{1}{2}\vec{b}_1 + \left(\frac{2}{3} - 1\right)\vec{b}_2 = -\frac{1}{6}\vec{b}_1 - \frac{1}{3}\vec{b}_2. \tag{C.6}$$

Thus the touching point should appear at

$$\vec{K}' + \beta\left(\frac{1}{2}\vec{b}_1 + \vec{b}_2\right) = \left(-\frac{1}{6} + \frac{\beta}{2}\right)\vec{b}_1 + \left(-\frac{1}{3} + \beta\right)\vec{b}_2, \tag{C.7}$$

where β is a real number. We again solve the equation $E_1 = 0$ and obtain the relation:

$$\beta = -\frac{1}{2\pi}\arccos\left(\frac{v^2 - 1}{2}\right) + \frac{1}{3}. \tag{C.8}$$

For $v = 0$, the spectrum is gapless at the K' point. The relation also holds until the amplitude is equal to or less than $\sqrt{3}$, in which case the gapless point around the K' point also comes to the origin.

To summarize, when the period of the external potential L is two, there are two Dirac points at the Fermi energy. For $v = 0$, the two points appear at the K and K' points. When we increase the amplitude, the gapless points approach each other and merge at the origin for $v = \sqrt{3}$. Beyond the threshold, the energy spectrum becomes gapful.

Appendix D

Multifractal analysis

D.1 Formalism of the multifractal analysis

The multifractal analysis of a continuous system is defined as follows [84, 85].

We consider a function $\mu(\vec{r})$ in the space V and try to regard it as a possibility distribution. If the value $\mu(\vec{r})$ can be negative, we use the absolute value or the square modulus of $\mu(\vec{r})$; let us use the latter here.

We divide the space V into $N(\epsilon)$pieces of small cells V_i of width ϵ. The probability $p_i(\epsilon)$ of the ith cell may be given by

$$p_i(\epsilon) = \frac{\int_{V_i} |\mu(\vec{r})|^2 d\vec{r}}{\int_V |\mu(\vec{r}')|^2 d\vec{r}'}, \tag{D.1}$$

which satisfies the normalized condition

$$\sum_{i=1}^{N(\epsilon)} p_i(\epsilon) = 1. \tag{D.2}$$

Let us assume that the probability $p_i(\epsilon)$ around the center of the ith cell depends on the cell size ϵ as

$$p_i(\epsilon) \sim \epsilon^{\alpha_i}, \tag{D.3}$$

where the index α_i represents the local singularity, or the local fractal dimension and is referred to as the singularity index or the Lipschitz-Hölder index. The singularity index α_i can take various values in different cells. We expect that the values of α_i are equal to each other in some cells when the space

is divided into a large enough number of cells. We thereby assume that the probability that we find the singularity index α_i in a small range $(\alpha, \alpha + d\alpha)$ is given by

$$\rho(\alpha)\epsilon^{-f(\alpha)}d\alpha, \tag{D.4}$$

where $\rho(\alpha)$ is the distribution function of the singularity index α and the function $f(\alpha)$ represents the fractal dimension of the support of the cell set which has the singular index α. The function $f(\alpha)$ is called the multifractal spectrum.

In order to obtain the multifractal spectrum, we consider the generalized dimension as follows. We first prepare the partition function

$$Z_q(\epsilon) = \sum_{i=1}^{N(\epsilon)} [p_i(\epsilon)]^q, \tag{D.5}$$

where the parameter q emphasizes different parts of the distribution probability $p_i(\epsilon)$. When q has a large positive value, the partition function $Z_q(\epsilon)$ is governed by cells with large values of $p_i(\epsilon)$. On the other hand, when q has a large negative value, the partition function $Z_q(\epsilon)$ is governed by cells with small values of $p_i(\epsilon)$.

The generalized dimension is given by the partition function in the form

$$D_q = \frac{1}{q-1}\lim_{\epsilon\to 0}\frac{\ln Z_q(\epsilon)}{\ln \epsilon}. \tag{D.6}$$

The generalized dimension is a type of the fractal dimension. For instance, the generalized dimension coincides with the information dimension D_1 for $q = 1$ and the correlation dimension dimension D_2 for $q = 2$, where

$$D_1 = \lim_{\epsilon\to 0}\frac{\sum_{i=1}^{N(\epsilon)} p_i(\epsilon)\ln p_i(\epsilon)}{\ln \epsilon} \tag{D.7}$$

and

$$D_2 = \lim_{\epsilon\to 0}\frac{\ln \sum_{i=1}^{N(\epsilon)} [p_i(\epsilon)]^2}{\ln \epsilon}. \tag{D.8}$$

This indicates that the generalized dimension (D.6) is an extension of the fractal dimensions.

In order to obtain a relation between the generalized dimension D_q and the multifractal spectrum $f(\alpha)$, we rewrite Eq. (D.5) using Eq. (D.4):

$$Z_q(\epsilon) = \int_0^\infty \rho(\alpha)\epsilon^{-f(\alpha)+q\alpha}d\alpha. \tag{D.9}$$

In the limit $\epsilon \to 0$, the integrand has a sharp peak at the value where $-f(\alpha) + q\alpha$ becomes minimum, namely at $\alpha = \alpha_q$ defined by

$$q = \left(\frac{df(\alpha)}{d\alpha} \right)_{\alpha=\alpha_q}. \tag{D.10}$$

Inserting the expansion

$$\begin{aligned} -f(\alpha) + q\alpha &= -\Bigg(f(\alpha_q) + (\alpha - \alpha_q) \left(\frac{df(\alpha)}{d\alpha} \right)_{\alpha=\alpha_q} \\ &\quad + \frac{(\alpha - \alpha_q)^2}{2!} \left(\frac{d^2 f(\alpha)}{d\alpha^2} \right)_{\alpha=\alpha_q} + \cdots \Bigg) + q\alpha \\ &= -f(\alpha_q) + q\alpha_q - \frac{1}{2}(\alpha - \alpha_q)^2 \left(\frac{d^2 f(\alpha)}{d\alpha^2} \right)_{\alpha=\alpha_q} + \cdots \end{aligned} \tag{D.11}$$

in Eq. (D.9) we have

$$Z_q(\epsilon) \simeq \rho(\alpha_q) \epsilon^{-f(\alpha_q)+q\alpha_q} \int_0^\infty \epsilon^{-\frac{1}{2}(\alpha-\alpha_q)^2 \left(\frac{d^2 f(\alpha)}{d^2 \alpha} \right)_{\alpha=\alpha_q}} d\alpha. \tag{D.12}$$

In order to obtain a finite value from the integral the following condition should be satisfied:

$$\left(\frac{d^2 f(\alpha)}{d\alpha^2} \right)_{\alpha=\alpha_q} < 0. \tag{D.13}$$

Equation (D.13) shows that the multifractal spectrum must be a concave function.

Substituting the expression (D.12) in Eq. (D.6) we have the relation:

$$\begin{aligned} D_q &\simeq \frac{1}{q-1} \lim_{\epsilon \to 0} \Bigg(\ln \rho(\alpha_q) + (-f(\alpha_q) + q\alpha_q) \ln \epsilon \\ &\quad + \ln \left(\int_0^\infty \epsilon^{-\frac{1}{2}(\alpha-\alpha_q)^2 \left(\frac{d^2 f(\alpha)}{d^2 \alpha} \right)_{\alpha=\alpha_q}} d\alpha \right) \Bigg) / \ln \epsilon \\ &\simeq \frac{1}{q-1} \left(-f(\alpha_q) + q\alpha_q \right). \end{aligned} \tag{D.14}$$

By introducing the quantity $\tau_q = (q-1)D_q$, we obtain the relations among the singularity index α_q, the multifractal spectrum $f(\alpha_q)$, and the generalized

dimension D_q as follows:

$$\alpha_q = \frac{d\tau_q}{dq} = \frac{d}{dq}\Big[(q-1)\,D_q\Big] \tag{D.15}$$

and

$$f(\alpha_q) = q\alpha_q - \tau_q = q\alpha_q - (q-1)D_q. \tag{D.16}$$

The multifractal spectrum $f(\alpha_q)$ reduces to a simple form for mono-fractal objects with a mono-fractal dimension $D_{\rm mono}$ $(= f(\alpha_q) = \alpha_q)$. Generally speaking, calculating the multifractal spectrum from numerical and experimental data is a tough task. Calculating $f(\alpha_q)$ from the generalized dimension D_q is simpler in many cases.

D.2 Multifractal analysis for finite lattice systems

In the previous section we introduced the multifractal analysis for a continuous systems. The purpose of this section is to extend the analysis to finite lattice systems. The outline of the analysis is almost the same, but we need some modification for discrete systems.

In the multifractal analysis for continuous systems, we regarded the cell size ϵ as a free parameter and set it to an infinitesimal value $\epsilon \to 0$. For lattice systems, however, we have the lattice constant as the smallest value. We therefore consider an infinite number of lattice points as the limiting operation. We also need to change the integral over $\vec{r}$ to the summation with respect to the cells.

Let us consider a function $P_j(x)$ on a one-dimensional lattice system as a simple example. We set the lattice constant unity. The probability of the ith cell of size l is given by

$$Q_i\left(\frac{l}{N}\right) = \frac{\sum_{k=i\,l}^{(i+1)\,l-1} |P_k(x)|^2}{\sum_{j=1}^{N} |P_j(x)|^2}, \tag{D.17}$$

where N is the total number of the lattice points. The partition function Z_q for lattice systems is defined as

$$Z_q\left(\frac{l}{N}\right) = \sum_{i=1}^{m}\left[Q_i\left(\frac{l}{N}\right)\right]^q, \tag{D.18}$$

where $m = N/l$ is the total number of the cells. The generalized dimension D_q is given by

$$D_q = \frac{1}{q-1} \lim_{N\to\infty} \lim_{\epsilon\to\epsilon_{\min}} \frac{\ln Z_q(l/N)}{\ln \epsilon}. \tag{D.19}$$

The cell size ϵ has the cutoff length $\epsilon_{\min} = l/N$, because one cannot set the size of the cells to the infinitesimal value because of the lattice constant. We alternatively set the total number of the lattice N to an infinite value. We can thereby obtain the generalized dimension D_q.

Bibliography

[1] A. H. C. Neto, F. Guinea, N. M. R. Peres, K. S. Novoselov, and A. K. Geim , Rev. Mod. Phys. **81**, 109 (2009).

[2] A. K. Geim and K.S. Novoselov, Nature Materials **6**, 183 (2007).

[3] P. R. Wallace, Phys. Rev. **71**, 622 (1947).

[4] J. W. McClure, Phys. Rev. **104**, 666 (1956).

[5] J. C. Slonczewski and P. R. Weiss, **109**, 272 (1958).

[6] S. Das Sarma, S. Adam, E. H. Hwang, and E. Rossi, Rev. Mod. Phys. **83**, 407 (2011).

[7] K. S. Novoselov, D. Jiang, F. Schedin, T. J. Booth, V. V. Khotkevich, S. V. Morozov, and A. K. Geim, Proc. Natl. Acad. Sci. **102**, 10451 (2005).

[8] N. D. Mermin, Phys. Rev. **176**, 250 (1968).

[9] K. S. Novoselov, A. K. Geim, S. V. Morozov, D. Jiang, Y. Zhang, S. V. Dubonos, I. V. Grigorieva, and A. A. Firsov, Science **306**, 666 (2004).

[10] K. S. Novoselov, A. K. Geim, S. V. Morozov, D. Jiang, M. I. Katsnelson, I. V. Grigorieva, S. V. Dubonos, and A. A. Firsov, Nature **438**, 197 (2005).

[11] Y. Zhang, Y.-W. Tan, H. L. Stormer, and P. Kim, Nature **438**, 201 (2005).

[12] J. C. Meyer, A. K. Geim, M. I. Katsnelson, K. S. Novoselov, T. J. Booth, and S. Roth, Nature **446**, 60 (2007).

[13] M. Koshino and T. Ando, Phys. Rev. B **73**, 245403 (2006).

[14] Y. Fujimoto and S. Saito, Phys. Rev. B **84**, 245446 (2011).

[15] G. W. Semenoff, Phys. Rev. Lett. **53**, 2449 (1984).

[16] C.-H. Park and S.G. Louie, Nano Lett. **9**, 1793 (2009).

[17] M. Gibertini, A. Singha, V. Pellegrini, M. Polini, G. Vignale, A. Pinczuk, L. N. Pfeiffer, and K. W. West, Phys. Rev. B 79, 241406(R) (2009).

[18] K. K. Gomes, W. Mar, W. Ko, F. Guinea, and H. C. Manoharan, Nature **483**, 306 (2012).

[19] S.-L. Zhu, B. Wang, and L.-M. Duan, Phys. Rev. Lett. **98**, 260402 (2007).

[20] P. Soltan-Panahi, J. Struck, P. Hauke, A. Bick, W. Plenkers, G. Meineke, C. Becker, P. Windpassinger, M. Lewenstein, and K. Sengstock, Nature Phys. **7**, 434 (2011).

[21] L. Tarruell, D. Greif, T. Uehlinger, G. Jotzu, and T. Esslinger, Nature **483**, 302 (2012).

[22] T. Uehlinger, G. Jotzu, M. Messer, D. Grif, W. Hofstetter, U. Bissbort, and T. Esslinger, Phys. Rev. Lett. **111**, 185307 (2013).

[23] O. Peleg, G. Bartal, B. Freedman, O. Manela, M. Segev, and D. N. Christodoulides, Phys. Rev. Lett. **98**, 103901 (2007).

[24] F. D. M. Haldane and S. Raghu, Phys. Rev. Lett. **100**, 013904 (2008).

[25] M. Polini, F. Guinea, M. Lewenstein, H. C. Manharan, and V. Pellegrini, Nature Nanotechnology **8**, 625 (2013).

[26] M. Yankowitz, J. Xue, and B. J. LeRoy, J. Phys. Condens. Matter **26**, 303201 (2014).

[27] L. A. Ponomarenko, R. V. Gorbachev, G. L. Yu, D. C. Elias, R. Jalil, A. A. Patel, A. Mishchenko, A. S. Mayorov, C. R. Woods, J. R. Wallbank, M. Mucha-Kruczynski, B. A. Piot, M. Potemski, I. V. Grigorieva, K. S. Novoselov, F. Guinea, V. I. Fal'ko, and A. K. Geim, Nature **497**, 594 (2013).

[28] M. Zarenia, O. Leenearts, B. Paroens, and F. M. Peeters, Phys. Rev. B **86**, 085451 (2012).

[29] M. Kindermann, B. Uchoa, and D. L. Miller, Phys. Rev. B **86**, 115415 (2012).

[30] J. C. W. Song, A. V.Shytov, and L. S. Levitov, Phys. Rev. Lett. **111**, 266801 (2013).

[31] M. Yankowitz, J. Xue, D. Cormode, J. D. Sanchez-Yamagishi, K. Watanabe, T. Taniguchi, P. Jarillo-Herrero, P. Jacquod, and B. J. LeRoy, Nature Phys. **8**, 382 (2012).

[32] M. Barbier, P. Vasilopoulos, and F. M. Peeters, Phys. Rev. B **81**, 075438 (2010).

[33] Z. Sun, C. L. Pint, D. C. Marcano, C. Zhang, J. Yao, G. Ruan, Z. Yan, Y. Zhu, R. H. Hauge, and J. M. Tour, Nature Comm. **2**, 559 (2011).

[34] J. C. Meyer, C. O. Girit, M. F. Crommie, and A. Zettl, Appl. Phys. Lett. **92**, 123110 (2008).

[35] R. Shi, H. Xu, B. Chen, Z. Zhang, and L.-M. Peng, Appl. Phys. Lett. **102**, 113102 (2013).

[36] Z. Jin, W. Sun, Y. Ke, C.-J. Shin, G. L. C. Paulus, Q.-H. Wang, B. Mu, P. Yin , and M. S. Strano, Nature Commun. **4**, 1663 (2013).

[37] P.-L. Zhao and X. Chen, Appl. Phys. Lett. **99**, 182108 (2011).

[38] I. Pletikosić, M. Kralj, P. Pervan, R. Brako, J. Coraux, A. T. N'Diaye, C. Busse, and T. Michely, Phys. Rev. Lett. **102**, 056808 (2009).

[39] M. Kralj, I. Pletikosić, M. Petrović, P. Pervan, M. Milun, A. T. N'Diaye, C. Busse, T. Michely, J. Fujii, and I. Vobornik, Phys. Rev. B **84**, 075427 (2011).

[40] C. Lin, X. Huang, F. Ke, C. Jin, N. Tong, X. Yin, L. Gan, X. Guo, R. Zhao, W. Yang, E. Wang, and Z. Hu, Phys. Rev. B **89**, 085416 (2014).

[41] N. Shima and H. Aoki, Phys. Rev. Lett. **71**, 4389 (1993).

[42] W. Oswald and Z. Wu, Phys. Rev. B **85**, 115431 (2012).

[43] H.-X. Yang, M. Chshiev, D. W. Boukhvalov, X. Waintal, and S. Roche, Phys. Rev. B **84**, 214404 (2011).

[44] I. I. Naumov and A. M. Bratkovsky, Phys. Rev. B **85**, 201414 (2012).

[45] J. Bai, X. Zhong, S. Jiang, Y. Huang, and X. Duan, Nature Nanotechnology **5**, 190 (2010).

[46] S. Berrada, V. H. Nguyen, D. Querlioz, J. Saint-Martin, A. Alarcón, C. Chassat, A. Bournel, and P. Dollfus, Appl. Phys. Lett. **103**, 183509 (2013).

[47] V. H. Nguyen, M. C. Nguyen, H.-Vi. Nguyen, and P. Dollfus, J. Appl. Phys. **113**, 013702 (2013).

[48] L. Jiang and Z. Fan, Nanoscale **4**, 1922 (2014).

[49] J. Haruyama, Electronics **2**, 368 (2013).

[50] K. Yan, D. Wu, H. Peng, L. Jin, Q. Fu, X. Bao, and Z. Liu, Nature Commun. **3**, 1280 (2012).

[51] K.-K. Bai, Y. Zhou, H. Zheng, L. Meng, H. Peng, Z. Liu, J.-C. Nie, and L. He, Phys. Rev. Lett. **113**, 086102 (2014).

[52] C.-H. Park, L. Yang, Y.-W. Son, M. L. Cohen, and S. G. Louie, Nature Phys. **4**, 213 (2008).

[53] C.-H. Park, L. Yang, Y.-W. Son, M. L. Cohen, and S. G. Louie, Phys. Rev. Lett. **101**, 126804 (2008).

[54] Y. Hatsugai, J. Phys.: Conf. Ser. **334**, 012004 (2011).

[55] V. M. Pereia, A. H. C. Neto, and N. M. R. Peres, Phys. Rev. B, **80**, 045401 (2009).

[56] Y. Hasegawa, R. Konno, H. Nakano, and M. Kohmoto, Phys. Rev. B, **74**, 033413 (2006).

[57] G. Montambaux, F. Piéchon, J.-N. Fuchs, and M. O. Goerbig, Phys. Rev. B, **80**, 153412 (2009).

[58] R. de Gail, J.-N. Fuchs, M.O. Goerbig, F. Piéchon, and G. Montambaux, Phyica B, **407**, 1948 (2012).

[59] K. Asano and C. Hotta, Phys. Rev. B **83**, 245125 (2011).

[60] H. Watanabe, Y. Hatsugai, and H. Aoki, Phys. Rev. B. **82**, 241403(R) (2010).

[61] G.-X. Ni, Y. Zheng, S. Bae, H. R. Kim, A. Pachoud, Y. S. Kim, C.-L. Tan, D. Im, J.-H. Ahn, B. H. Hong, and B. Özyilmaz, ACS Nano **6**, 1158 (2012).

[62] S. H. R. Sena, J. M. Pereira Jr, G. A. Farias, M. S. Vasconcelos, and E. L. Albuquerque, J. Phys.: Condens. Matter. **22**, 465305 (2010).

[63] S. Mukhopadhyay, R. Biswas, and C. Sinha, Phys. Status Solidi B **247**, 342 (2010).

[64] T. Fujiwara and Y. Ishii: in *Quasicrystals*, ed. T. Fujiwara and Y. Ishii (Elsevier 2008) pp.1 – 9.

[65] T. Fujiwara: in *Physical Properties of Quasicrystals*, ed. Z. M. Stadnik (Springer, 1999) p. 173.

[66] E. Maciá: Rep. Prog. Phys. **69**, 397 (2006).

[67] M. Kohmoto, B. Sutherland, and C. Tang: Phys. Rev. B **35**, 1020 (1987).

[68] T. Fujiwara, M. Kohmoto, and T. Tokihiro: Phys. Rev. B **40**, 7413 (1989).

[69] M. Baake: in *Quasicrystals: An Introduction to Structure, Physical Properties and Applications*, ed. J.-B. Suck, M. Schreiber, and P. Häussler (Springer, 2002) p.17.

[70] D. Shechtman, I. Blech, D. Gratias, and J. W. Cahn: Phys. Rev. Lett. **53**, 1951 (1984).

[71] D. Levine and P. J. Steinhardt: Phys. Rev. Lett. **53**, 2477 (1984).

[72] A. Sutö: J. Stat. Phys. **56**, 525 (1989).

[73] G. Mantica: Physica D **103** 576, (1996).

[74] I. Guarneri and G. Mantica, Phys. Rev. Lett. **73**, 3379 (1994).

[75] M. Tashima and S. Tasaki, J. Phys. Soc. Jpn. **80**, 074004 (2011).

[76] M. Tashima and N. Hatano, J. Phys. Soc. Jpn. **82**, 113706 (2013).

[77] M. Tashima and N. Hatano, J. Phys. Soc. Jpn. Conf. Proc. **4**, 013002 (2015).

[78] C. Kittel: Introduction to Solid State Physics (8th edition), Wiley (2004).

[79] Z. V. Vardeny, A. Nahata, and A. Agrawal, Nature Photon. **7**, 177 (2012).

[80] K. Hayashida, T. Dotera, A. Takano, and Y. Matsushita, Phys. Rev. Lett. **98**, 195502 (2007).

[81] W. B. Jones and W. J. Thron: Continued Fractions: Analytic Theory and Applications (Encyclopedia of Mathematics and its Applications, Vol. 11), Addison Wesley (1980).

[82] S. Katayama, A. Kobayashi, and Y. Suzumura, J. Phys. Soc. Jpn. **75**, 054705 (2006).

[83] D. Hsieh, D. Qian, L. Wray, Y. Xia, Y. S. Hor, R. J. Cava, and M. Z. Hasan, Nature **452**, 970 (2008).

[84] P. Meakin: *Fractals, scaling and growth far from equilibrium* (Cambridge University Press, 1998) p. 160.

[85] J. Feder: *Fractals* (Plenum Press, 1988) p. 66.

[86] H. Cohen: A Course in Computational Algebraic Number Theory, Springer (1993).